THESIS FOR THE DEGREE OF DOCTOR OF PHILOSOPHY

Decoherence and noise in High critical Temperature Superconducting quantum nanodevices

MARCO ARZEO

CHALMERS

Department of Microtechnology and Nanoscience
Quantum Device Physics Laboratory
Chalmers University of Technology
Göteborg, Sweden 2016

Decoherence and noise in High critical Temperature Superconducting quantum nanodevices

MARCO ARZEO
ISBN 978-91-7597-474-3

Author email: `marco.arzeo@chalmers.se`

Doktorsavhandlingar vid Chalmers tekniska högskola
Ny serie nr 4155
ISSN 0346-718X

Chalmers University of Technology
Department of Microtechnology and Nanoscience (MC2)
Quantum Device Physics Laboratory
SE-412 96 Göteborg, Sweden
Telephone +46 (0)31-772 1000

ISSN 1652-0769
Technical Report MC2-348

Printed by Chalmers Reproservice, Chalmers University of Technology
Göteborg, Sweden, October 2016

Decoherence and noise in High critical Temperature Superconducting quantum nanodevices
MARCO ARZEO
Department of Microtechnology and Nanoscience, MC2
Chalmers University of Technology
Göteborg, Sweden 2016

Abstract

The thesis deals with the investigation of dissipation mechanisms and noise in superconducting quantum nanodevices made of the cuprate High critical Temperature Superconductor (HTS) $YBa_2Cu_3O_{7\text{-}\delta}$ (YBCO). The main aim is to get a better understanding of the microscopic physical mechanism leading to superconductivity in HTSs, which still represents one of the main unsolved problems in solid-state physics. In this respect, YBCO nanodevices are used as tools to design new experiments, which can deliver deeper insights about the complex properties of HTS materials.

In the first part of the thesis transport and noise properties of nanowire based YBCO Superconducting QUantum Interference Devices (SQUIDs) are presented. NanoSQUID devices, with transport properties close to the pristine bulk material, are potential tools to investigate fundamental physics of the YBCO by looking e.g. at the fluxoid quantization. Moreover, because of the measured ultra low magnetic flux white noise (below $1\,\mu\Phi_0/\sqrt{\mathrm{Hz}}$), these devices are very attractive for applications as magnetic flux sensors. Flux noise properties are not degraded when employing an inductively coupled, mainly via kinetic inductance, large pick-up loop. This allows to improve magnetic field sensitivity, with possible applications in magnetic field imaging, such as magnetoencephalography.

The second part of the thesis discusses the employment of an all-YBCO transmon quantum circuit based on bi-epitaxial grain boundary Josephson junctions to study decoherence mechanisms intrinsic of the material. First, microwave losses from all the materials involved in the fabrication process, including the dielectric substrates and the YBCO itself, are investigated at very low temperatures and microwave powers. The reported results demonstrate the feasibility of a YBCO transmon. Then, the quantum coherence of the device, extracted from spectroscopy measurements, is studied in the presence of high magnetic field and a comparison to DC-transport properties is made. A significant improvement of the coherence time is observed with the application of an external magnetic field, compatible with the occurrence of a fully gapped superconducting state. The main dissipation source has been identified in the presence of a resistive shunt in the junction barrier.

Keywords: High-Tc superconductors, nanowire based nanoSQUIDs, noise, microwave losses, dielectric losses, transmon qubit, quantum coherence

A Michele, Maria e Rosario

And on the pedestal these words appear:
"My name is Ozymandias, king of kings:
Look on my works, ye Mighty, and despair!"
Nothing beside remains. Round the decay
Of that colossal wreck, boundless and bare,
The lone and level sands stretch far away.
Percy Bysshe Shelley - 1818

List of publications

This thesis is based on the work reported in the following publications:

I **Ultra low noise $YBa_2Cu_3O_{7\text{-}\delta}$ nano superconducting quantum interference devices implementing nanowires**
R. Arpaia, **M. Arzeo**, S. Nawaz, S. Charpentier, F. Lombardi, and T. Bauch
Applied Physics Letter **104**, 072603 (2014).

II **Toward ultra high magnetic field sensitivity $YBa_2Cu_3O_{7\text{-}\delta}$ nanowire based superconducting quantum interference devices**
M. Arzeo, R. Arpaia, R. Baghdadi, F. Lombardi, and T. Bauch
Journal of Applied Physics, **119**, 174501 (2016).

III **Microwave losses in MgO, $LaAlO_3$, and $(La_{0.3}Sr_{0.7})(Al_{0.65}Ta_{0.35})O_3$ dielectrics at low power and in the millikelvin temperature range**
M. Arzeo, F. Lombardi, and T. Bauch
Applied Physics Letter **104**, 212601 (2014).

IV **Microwave Losses in YBCO Coplanar Waveguide Resonators at Low Power and Millikelvin Range**
M. Arzeo, F. Lombardi, and T. Bauch
IEEE Transactions on Applied Superconductivity **25**, 3 (2015).

V **Increased coherence time of an all-YBCO transmon quantum circuit at high magnetic fields**
M. Arzeo, F. Lombardi, and T. Bauch
Manuscript to be submitted... (2016).

Publications outside the scope of this thesis:

- **Resistive state triggered by vortex entry in $YBa_2Cu_3O_{7-\delta}$ nanostructures**
  R. Arpaia, D. Golubev, R. Baghdadi, **M. Arzeo**, G. Kunakova, S. Charpentier, S. Nawaz, F. Lombardi, and T. Bauch
  Physica C: Superconductivity and its Applications **506**, 165 (2014).

- **Highly homogeneous YBCO/LSMO nanowires for photoresponse experiments**
  R. Arpaia, M. Ejrnaes, L. Parlato, R. Cristiano, **M. Arzeo**, T. Bauch, S. Nawaz, F. Tafuri, G.P. Pepe, and F. Lombardi
  Superconductor Science and Technology **27**, 4 (2014).

- **Fast Electron Thermometry for Ultrasensitive Calorimetric Detection**
  S. Gasparinetti, K.L. Viisanen, O.-P. Saira, T. Faivre, **M. Arzeo**, M. Meschke, and J.P. Pekola
  Physical Review Applied **3**, 014007 (2015).

- **Improved noise performance of ultrathin YBCO Dayem bridge nanoSQUIDs**
  R. Arpaia, **M. Arzeo**, R. Baghdadi, E. Trabaldo, F. Lombardi and T. Bauch
  Superconductor Science and Technology, to be published... (2016).

List of symbols

Constants

h	Planck constant	$\simeq 6.63 \times 10^{-34}$ Js
e	Elementary charge	$\simeq 1.6 \times 10^{-19}$ C
c	Speed of light in vacuum	$\simeq 3 \times 10^{8}$ m/s
k_B	Boltzmann constant	$\simeq 1.38 \times 10^{-23}$ J/K
m	Electron mass	$\simeq 9.11 \times 10^{-31}$ Kg
μ_0	Vacuum permeability	$\simeq 4\pi \times 10^{-7}$ H/m
Φ_0	Magnetic flux quantum	$h/2e \simeq 2.07 \times 10^{-15}$ Tm^2

Chapter 1: Introduction

$7-\delta$	Oxygen content per unit cell
Δ	Superconducting energy gap
e_s	Charge of the superconducting electrons
E_F	Fermi energy
g_{eff}	Electron-phonon coupling
J_s	Superconducting current density
λ_L	London penetration depth
m_s	Mass of the superconducting electrons
n_s	Density of the superconducting electrons
p	Hole doping per planar copper atom
ϕ	Superconducting phase
$\Psi(\vec{r})$	Superconducting order parameter
T_c	Critical temperature
ω_D	Debye frequency
V_{eff}	Phonon mediated electron-electron interaction
ξ	Superconducting coherence length

Chapter 2: Theoretical background

Josephson effect

α	Grain boundary angle
α_d	Dissipation parameter
β_c	Damping factor
D	Junction transparency
δ	Minigap
E_{JJ}	Josephson energy
E_J	Maximum Josephson energy
I_b	Bias current
I_c	Critical current
L_J	Josephson inductance
K	Coupling amplitude
Q	Josephson junction quality factor
ω_P	Plasma frequency

SQUIDs

A_{eff}	Effective area
A_{eff}^{nS}	NanoSQUID effective area
A_{eff}^{pl}	Pickup loop effective area
β_L	Screening inductance factor
δ_L	Inductance asymmetry parameter
d_w	Separation distance between nanowires
γ_r	Relaxation rate
J_d	Depairing current
λ_P	Pearl length, $2\lambda_L^2/t$
Λ	TLS tunnelling strength
Λ_0	Double-well barrier height
l	Nanowire length
L	Total inductance
L_c	Coupling inductance
L_{ex}	Geometric inductance
L_{kin}	Kinetic inductance
L_{pl}	Total pickup inductance
Φ	Magnetic flux
$S(f)$	Power spectral density
$S_B^{1/2}$	Magnetic field noise
$S_\Phi^{1/2}$	Magnetic flux noise
τ_u	Lifetime of the untrapped state
τ_t	Lifetime of the trapped state
t	Thickness
U	Double-well potential asymmetry
v	Cooper pairs velocity
w	Nanowire width
w_e	Electrodes width

Coplanar waveguide resonators

C_c	Coupling capacitance
$\vec{d}$	Electric dipole
ϵ_{eff}	Effective dielectric constant
F	Filling factor
f_0	Fundamental resonance frequency
λ	Electromagnetic field wavelength
n_N	Density of normal electrons
P_c	Critical power
P_{cir}	Circulating power
Q_0	Unloaded quality factor
Q_d	Dielectric quality factor
Q_{ext}	External/coupling quality factor
Q_L	Loaded quality factor
Q_{rad}	Radiation quality factor
R_s	Surface resistance
$\tan\delta$	Dielectric losses
v_{ph}	Phase velocity

Superconducting quantum bit

a	Photon annhilation operator
$a^\dagger$	Photon creation operator
A	Critical current fluctuations amplitude
A_{GB}	Critical current fluctuations amplitude for a grain boundary junction
α	Anharmonicity of the energy levels
α_r	Relative anharmonicity
C_B	Transmon shunting capacitance
C_g	Gate capacitance
C_J	Josephson junction capacitance
C_Σ	Total transmon capacitance
χ	Dispersive shift
Δ_0	Transmon-cavity detuning
E_c	Charging energy
f_a	Atom/qubit transition frequency
g_{01}	Transmon-cavity coupling strength
$\hat{n}$	Number operator
N_{qp}	Number of quasiparticles
Q	Charge stored in the capacitor
σ_+	Raising operator
σ_-	Lowering operator
σ_z	Pauli operator
T_1	Relaxation time
T_2	Decoherence time
T_ϕ	Dephasing time

Chapter 3: Modelling, fabrication and experimental techniques

C_R Resonator equivalent lumped element capacitance

E_{Jmax} Maximum Josephson energy

L_R Resonator equivalent lumped element inductance

Φ_e Externally applied magnetic flux

$S_V^{1/2}$ Voltage noise

V_Φ Transfer function

V_{rms}^0 Root mean square voltage of the resonator vacuum fluctuations

Z_0 Experimental characteristic impedance, $\simeq 50\,\Omega$

Z Transmission line characteristic impedance

Chapter 4: YBCO nanowire based nanoSQUIDs

A_{eff}^{an} Analytic effective area

A_{eff}^{num} Numerical effective area

A_{geo} Geometric area

β_L^{exp} Experimental screening inductance factor

β_L^{num} Numerical screening inductance factor

ΔB Magnetic field periodicity

ΔI_c Critical current modulation

$\delta\Phi$ Magnetic flux fluctuations

δV Voltage fluctuations

f_c Lorentzian characteristic frequency

$F_0^{1/2}$ Lorentzian amplitude

λ_0 London penetration depth at $T = 0$

R_d Differential resistance

ξ_0 Superconducting coherence length at $T = 0$

Chapter 5: Microwave losses in YBCO resonators in the single photon limit

δf_0 Resonance frequency shift

ϵ_r Relative dielectric permittivity

Γ Complex reflection coefficient

N_{ph} Average number of photons

Ψ Complex digamma function

Q_b Total background quality factor

Chapter 6: Characterization of an all-YBCO transmon quantum bit

A_{cp} Area of Cooper pairs channels

A_{qp} Area of quasiparticles channels

$B_\parallel$ In-plane magnetic field

d $d-$wave component of the order parameter

Δf Spectroscopic linewidth

is Imaginary $s-$wave component of the order parameter

f_{rf} Probing frequency

f_1 Second tone frequency

γ Decoherence rate

J_c Critical current density

κ Resonator decay rate

R_N Normal resistance

S_I Relative critical current fluctuations

S_R Relative normal resistance fluctuations

S_V Voltage power spectrum

List of abbreviations

AC	Alternate Current
AFM	Atomic Force Microscope
CPR	Current Phase Relation
CPW	CoPlanar Waveguide
DC	Direct Current
GB	Grain Boundary
GL	Ginzburg-Landau
HTS	High critical Temperature Superconductor
JJ	Josephson Junction
LAO	$LaAlO_3$
LSAT	$(La_{0.3}Sr_{0.7})(Al_{0.65}Ta_{0.35})O_3$
LTS	Low critical Temperature Superconductor
MGS	MidGap State
PLD	Pulsed Laser Deposition
RCSJ	Resistively and Capacitively Shunted Junction
SEM	Scanning Electron Microscope
SC	SuperConductor
S-c-S	Superconductor-Constriction-Superconductor
S-I-N	Superconductor-Insulator-Normal
S-I-S	Superconductor-Insulator-Superconductor
S-N-S	Superconductor-Normal-Superconductor
SQUID	Superconducting QUantum Interference Device
TEM	Transversal Electro-Magnetic
TLF	Two-Level Fluctuator
TLS	Two-Level System
XRD	X-Ray Diffraction
YBCO	$YBa_2Cu_3O_{7-\delta}$

Contents

Chapter 1

Introduction

1.1 Motivations

The discovery of cuprates high critical temperature superconductors (HTSs) thirty years ago[1] was a scientific breakthorugh in solid state physics. The fascinating phenomenon of superconductivity at temperature even above the one of liquid nitrogen ($T = 77$ K) in these materials attracted the attention of many researchers in the field, with interests in both fundamental physics and various possible applications. A lot has been done since then, but we still lack a full understanding of the microscopic physical mechanism leading to superconductivity in these materials[2, 3]. Moreover, in the recent years, many different experiments have demonstrated the occurrence of nanoscale ordering in the form of charge density wave (CDW)[4, 5], ubiquitous in all the cuprates family. This form of nanoscale ordering intertwines with the superconducting state and has contributed to enhance the complexity of cuprates. In order to shed light on this long-standing problem in solid state physics, new experimental observations are needed[2]. A possible approach, which has been pursued in this thesis work, consists in the realization of quantum devices made of such materials and probing their superconducting properties. In this respect, quantum devices are employed as tools to obtain new experimental findings.

During the last few decades, the use of superconductors to engineer macroscopic physical systems, for which the laws of quantum mechanics can be applied, has been proven to be very successful. In particular, the implementation of conventional low critical temperature superconductors (LTSs) Josephson junctions (JJs) devices has allowed the observation of various quantum phenomena such as: macroscopic quantum tunnelling (MQT)[6], energy levels quantization[7] and quantum superposition of macroscopic states[8]. Coherent oscillations between different distinct quantum states (macroscopic quantum coherence), and their manipulation have also been extensively reported in these devices[9, 10]. Among JJ based devices, Superconducting QUantum Interference Devices (SQUIDs), combining Josephson effect with quantization of magnetic flux in superconducting loops, manifest an astonishing macroscopic quantum coherence[11]. Moreover, they are among the most sensitive magnetic flux and field detectors, and for this reason can be employed for several applications [12, 13, 14, 15, 16]. In this respect, the use of high critical temperature superconductors allows to extend the operation temperature range, with a significant reduction of the costs involved[17].

Furthermore, the observation of quantum coherence made JJ based devices very attractive to serve as quantum-bits (qubits) in quantum information processing[18, 19]. The advantage of using superconductors lies in the presence of a well-developed energy gap for the excitation spectrum of quasiparticles, resulting in very low dissipation, which helps to preserve phase coherence over rather long time scales (up to hundreds of μs)[20]. Moreover, these devices allow for scalability and excellent control, thanks to well-established fabrication and advanced measurement techniques.

Unconventional JJs made of high critical temperature superconductors represent another possible candidate for realizing such macroscopic quantum circuits. For this class of materials, the $d-$wave symmetry of the order parameter, describing the superconducting state, opens the possibility to explore new configurations[21]. However, because of the very challenging fabrication, and above all of the extra decoherence coming from the presence of nodal quasiparticles and zero-energy bound states, $d-$wave JJs have not been pursued much in this field. On the other hand, the realization of quantum circuits made of HTSs could be used to investigate fundamental physics in previously inaccessible regimes, and pave the way for the understanding of the microscopic mechanism leading to superconductivity in these materials. Recent findings have demonstrated macroscopic quantum behavior in $YBa_2Cu_3O_{7\text{-}\delta}$ (YBCO) bi-epitaxial Josephson junctions[22, 23] and a fully developed gap in the quasiparticles excitation spectrum in the superconducting island of a YBCO single electron transistor at very low temperatures[24]. These findings clearly require a reconsideration of the dissipation mechanisms in HTSs, and this thesis work follows up on that. The main focus is on the characterization of noise and decoherence sources intrinsic to the material itself. In particular, the thesis presents results from the study of noise properties of YBCO nanowire based nanoSQUIDs, and the investigation of decoherence in a YBCO transmon quantum circuit.

1.2 Superconductivity

Discovered by H. K. Onnes[25] in 1911, *superconductivity* represents one of the main breakthrough in solid state physics of the last century. Onnes first observed that some metals like: mercury, lead and tin, cooled down below a certain critical temperature (T_c), show an abrupt decrease of the electrical resistance by several orders of magnitude: perfect conductivity. However, superconducting materials are more than perfect conductors. In fact, when the temperature is reduced below T_c, the magnetic field is completely expelled from a superconductor, exhibiting perfect diamagnetism. This effect arises from the presence of persistent screening currents, which flow to compensate the externally applied magnetic field inside the superconductor, and is known as *Meissner effect*, from the name of the physicist who first experimentally observed this phenomenon in 1933[26].

A first successful phenomenological description of the two above mentioned electrodynamic properties of superconductors was given by the brothers F. and H. London in 1935[27]. They proposed two equations to describe the electric $\vec{E}$ and magnetic $\vec{B}$ field inside the superconductor:

$$\begin{aligned} \vec{E} &= \mu_0 \lambda_L^2 \frac{\partial \vec{J}_s}{\partial t} \\ \vec{B} &= -\mu_0 \lambda_L^2 \nabla \times \vec{J}_s, \end{aligned} \tag{1.1}$$

where $\vec{J}_s$ is the superconducting current density, $\lambda_L = \sqrt{\frac{m_s}{\mu_0 e_s^2 n_s}}$ a phenomenological parameter known as London penetration depth, with m_s, e_s and n_s the mass, the charge and the density of superconducting electrons, respectively. The London penetration depth represents the length scale within which the DC-magnetic field can penetrate inside a superconductor[1], and it is material dependent.

A more complete phenomenological model, based on Landau's mean field theory of second-order phase transitions, was proposed by V. L. Ginzburg and L. Landau (GL) himself[28]. They assume that the free energy F of a superconductor, near its superconducting transition, can be expressed in terms of a spatial-dependent complex order parameter Ψ:

$$\Psi(\vec{r}) = \sqrt{n_s(\vec{r})}e^{i\phi(\vec{r})}, \tag{1.2}$$

where ϕ is known as the superconducting quantum phase. Equation (1.2) shows that the order parameter is related to the density of the superconducting electrons, such that: $|\Psi|^2 = n_s$; Ψ is nonzero in the superconducting state ($n_s \neq 0$) and vanishes in the normal state ($n_s = 0$). Indeed, $\Psi(\vec{r})$ as expressed in Eq. (1.2) has the form of a wave function. Beyond the results obtained from the London equations, the GL theory predicts a second characteristic length scale ξ, over which spatial changes in Ψ occur. The coherence length is material dependent, and it represents a fundamental parameter for describing physical properties of the devices presented in this thesis work.

At the first, Ginzburg and Landau did not associate Ψ to any microscopic physical parameter. This was done only after that a full microscopic theory of conventional superconductivity was developed in 1957 by Bardeen-Cooper-Schrieffer (BCS)[29]. Then the GL equations were demonstrated to be a limit of the BCS theory when the temperature approaches T_c[30]. The main idea behind the BCS theory is the concept of Cooper-pairs. Two negative charges, like electrons, normally repel each other as a result of Coulomb interaction. However, a metal is characterized by a positively charged ionic lattice, whose vibrations (phonons) in certain conditions can mediate the electron-electron interaction resulting in an effective attraction. Therefore, the net attraction, although small, can make it possible the formation of electron pairs. As a consequence, two paired electrons, which individually would obey to Fermi-Dirac statistics (fermions) behave instead as bosons. They are referred to as Cooper pairs. The Cooper-pairs can condensate occupying the same quantum state (superconducting state), described by a wave function of the form of Eq. (1.2). In the BCS framework, the effective phonon mediated electron-electron attractive interaction V_{eff} is written as[31]:

$$V_{eff}(\omega) = |g_{eff}|^2 \frac{1}{\omega^2 - \omega_D^2}, \tag{1.3}$$

where g_{eff} is the effective electron-phonon coupling and ω_D is the Debye frequency. Here, ω_D represents a cut-off frequency, above which the interaction becomes repulsive. A negative V_{eff} promotes the formation of a bound state, i.e. for two electrons it is energetically favourable to form a Cooper pair. The characteristic binding energy for Cooper pairs, known as superconducting energy gap Δ, can be written as[31]:

$$\Delta \simeq 2\hbar\omega_D e^{-1/N(E_F)g_{eff}} \simeq 1.76 k_B T_c, \tag{1.4}$$

[1]As regards AC transport properties, λ_L is the length scale on which AC-electromagnetic field penetrate in the superconductor.

where E_F is the Fermi energy, $N(E_F)$ is the electrons density of state at the Fermi level. Equation (1.4) is valid only in the limit $N(E_F)g_{eff} \ll 1$, in the so-called *weak coupling approximation*, which holds for most of the classic superconductors. Any energy larger than 2Δ will break Cooper pairs and consequently destroy the superconducting state. From Eq. (1.4), it is clear that to get a larger critical temperature T_c, one has to increase ω_D, $N(E_F)$ or g_{eff}. Unfortunately, $N(E_F)$ and g_{eff} are not independent: increasing $N(E_F)$ results in a larger screening of the phonons from the electrons and therefore g_{eff} will decrease; a large g_{eff} can result in different instabilities (polarons, charge density wave), which cause a drop of $N(E_F)$. On the other hand, the Debye frequency ω_D is larger for light atoms and could results in a significant increase of T_c. In fact, metallic hydrogen (possible at high pressure) is expected to be a room temperature superconductor. Moreover, the highest $T_c \simeq 203$K has been recently observed in H_2S under high pressure[32]. However, for many decades, it was believed that T_c could hardly reach the value of 30 K (the highest experimentally measured was $T_c = 23$ K for a niobium-germanium compound). Only with the discovery of superconductivity in copper oxides (cuprates), first made for $La_{2-x}Ba_xCuO_4$ ($T_c \simeq 30$ K) by G. Bednorz and K. Muller in 1986[1], the critical temperature was drastically increased. It soon exceeded the value of the nitrogen boiling temperature ($T = 77$ K) with the experimental observation of superconductivity in the $YBa_2Cu_3O_{7-\delta}$ (YBCO, $T_c \simeq 90$ K) in 1987[33].

Cuprates, together with other materials, form a new class of compounds known as High critical Temperature Superconductors (HTSs), whose physical properties differ from the conventional superconductors or Low critical Temperature Superconductors (LTSs) properly described by the BCS theory.

1.3 High-T_c superconductivity in cuprates: YBCO

The discovery of high critical temperature superconductivity in copper oxides is considered one of the most important scientific achievements of the twentieth century. These strongly correlated electron systems exhibit different aspects of quantum matter physics, and have attracted and frustrated many researchers during the last three decades. The understanding of the microscopic mechanism behind superconductivity in these materials is still an unsolved problem. If one thinks in terms of BCS theory for conventional superconductors, cuprates would be expected to be the least likely materials to show superconductivity. In fact, even though one replaces the electron-phonon with any other attractive interaction (mediated by a different excitation), the electrons density of state $N(E_F)$ will still be not well defined. The reason is that, in the normal state, cuprates have not a conventional Fermi surface. They are not standard metals above T_c. Moreover, the direct proportionality between the Debye frequency ω_D and the critical temperature, as expressed by Eq. (1.4), does not hold for cuprates. Even using a generalized expression (not only valid in the weak limit approximation), would result in a too large electron-phonon coupling[34].

In general, the structural and transport properties of cuprates are very complex and strongly doping dependent. Among the cuprates family, YBCO is the most known, the first to show a T_c larger than the nitrogen boiling temperature, and the most studied perovskite. Moreover, it is the main superconducting material used for this thesis work. The $YBa_2Cu_3O_{7-\delta}$ is characterized by a more complex crystallographic structure compared to LTSs. It consists of three stacked perovskite cells (see Fig. 1.1), and its structure is doping dependent. If the oxygen content is such that $\delta = 1$, the structure is tetragonal ($a = b$) and the material is insulating (see the phase diagram for hole doping per planar Cu atom $p < p_{min} = 0.05$, Fig. 1.2). By increasing the oxygen content up to the critical point characterized by $\delta = 0.65$ ($p = 0.05$), the structure becomes orthorhombic, CuO chains are formed along the b direction with a consequent elongation of the b-axis. In this particular case, the unit cell is characterized by an Yttrium atom (orange sphere) surrounded by two CuO_2 planes in the middle, and CuO chains with a Barium atom (green spheres) at the center in the top and the bottom layers (see Fig. 1.1). The unit cell lattice parameters for optimally doped YBCO ($\delta = 0.05$, $p = 0.16$) are: $a = 3.82$ Å, $b = 3.89$ Å, and $c = 11.69$ Å. The CuO chains act as charge reservoirs for the CuO_2 planes, where most of the carriers are localized. Because of the poor coupling between CuO_2 planes and the larger carrier

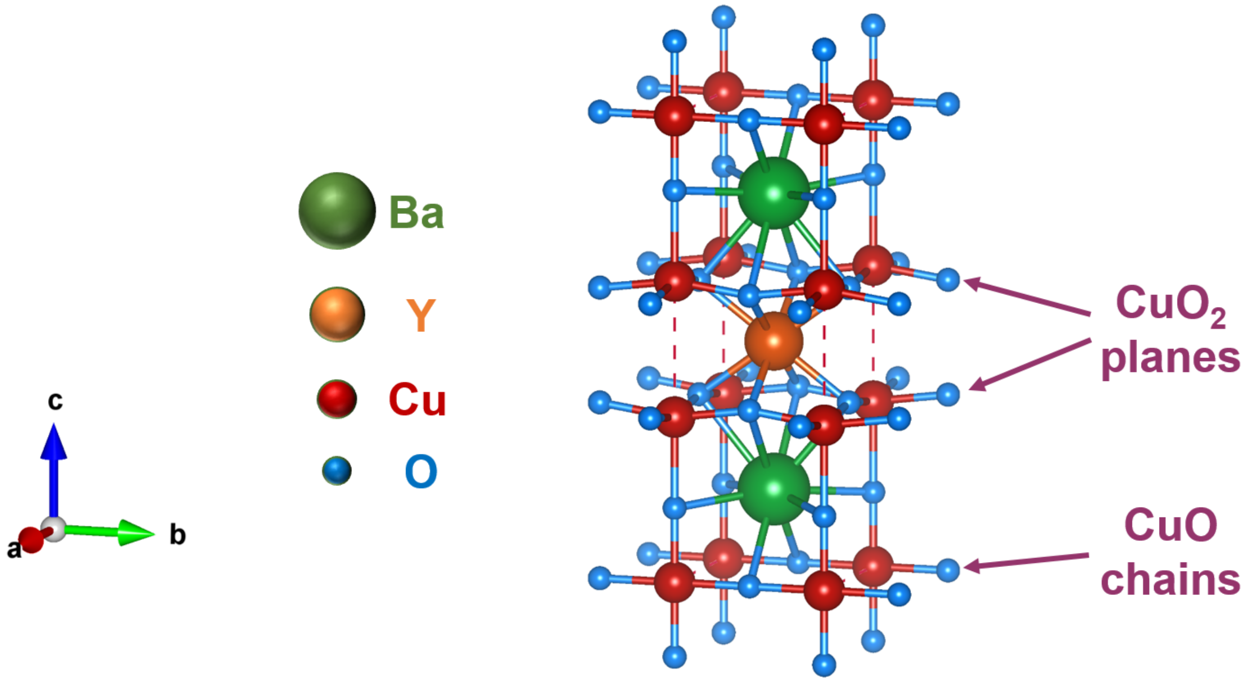

Figure 1.1: Unit cell sketch of an orthorhombic, optimally doped YBCO.

density localized in those planes, the transport properties for both the normal and the superconducting state are strongly anisotropic. In particular, superconductivity is much weaker along the c-axis compared to the ab planes. Moreover, due to the orthorhombic unit cell ($a < b$), transport is also anisotropic in the ab planes for untwinned[2] YBCO single crystals and thin films close to optimal doping. In-plane anisotropy for YBCO has been experimentally observed for the London penetration depth[35], the normal resistivity[36], the critical current[37] and the energy gap[38, 39]. A summary of the superconducting parameters of optimally doped YBCO, in comparison to most common LTS materials, are listed in Table 1.1. Orthorhombic YBCO is very reactive and prone to oxygen out-diffusion, which results in a deterioration of the superconducting properties. This makes

[2] a- and b-axis are not randomly oriented.

the superconducting YBCO very difficult to handle, especially during the micro- and nano-fabrication processes as it will be discussed in section 3.2.

Figure 1.2 shows the phase diagram of the YBCO, where the different electronic phases are plotted versus temperature and the hole doping per planar Cu atom (p), and the different phases are indicated. In details, starting from the zero doping ($p = 0$), the parent

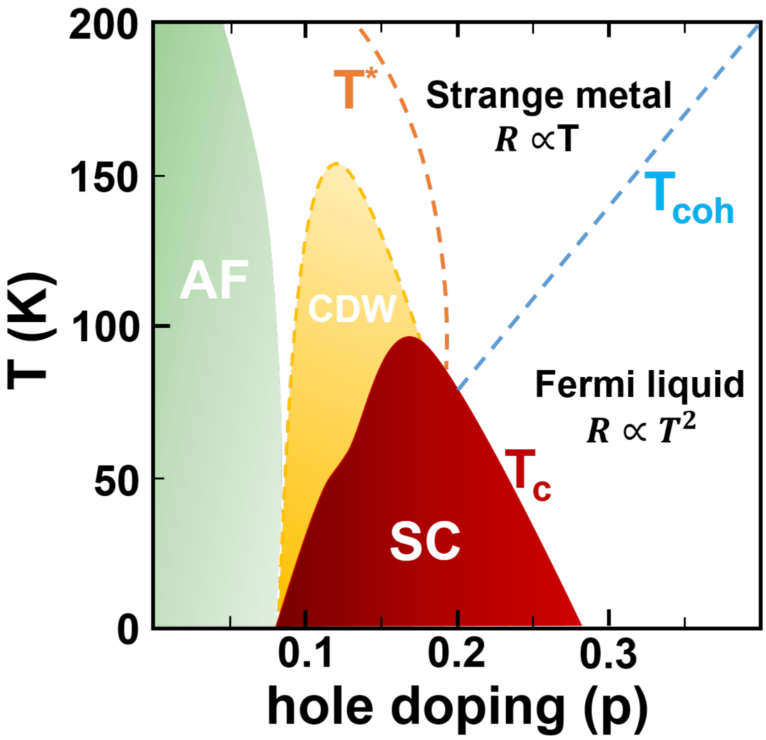

Figure 1.2: Phase diagram of the YBCO as a function of the temperature and the hole doping p. The different phases occurring for this material are also indicated. AF labels the antiferromagnetic insulating region, CDW the charge density wave, and SC the superconducting dome. T^*, T_c and T_{coh} are respecitively the pseudogap, the critical and the coherence temperature.

compound is antiferromagnetic insulating. Magnetism origins from repulsive interactions between electrons, which is in contrast with the attractive interaction forming Cooper-pairs and inducing superconductivity. YBCO becomes conducting upon doping with holes. Above the critical temperature T_c (normal state), the transport phenomenology of the cuprates is not explainable with classic theory of metals. YBCO first exhibits a behavior specific to copper oxides HTS known as "pseudogap" regime, characterized by a significant suppression of the electron density of states. The pseudogap has been detected by several experiments in a wide range of temperature right above T_c and specifically in the *underdoped* region ($p < 0.16$)[40]. Whether the pseudogap is related or not to the superconducting gap is still under debate[41, 42]. Moreover, in the same region of the phase diagram, many recent experiments have proven the existence of various forms of order such as: charge density wave (CDW)[4, 5], spin density wave (SDW)[43], and electron nematic order[44]. By further increasing the doping, above T_c, YBCO is then referred to as "strange" or "bad" metal. Compared to conventional metals, it is characterized by a smaller conductivity, and different frequency and temperature dependencies ($R \propto T$). Such behaviour is usually described by the "marginal Fermi liquid" model[45], and it has been observed in a large number of materials belonging to the strongly correlated electron systems family with no superconducting transition. This might suggest that such a behaviour has no correlation to high-T_c superconductivity. Finally, the section of phase diagram defined by $p > 0.16$ is known as overdoped region, and in particular, is described by a Fermi liquid model ($R \propto T^2$).

The superconducting dome (dark red region) is delimited by the critical temperature T_c and the hole doping values ranging between $p_{min} = 0.05 \leq p \leq p_{max} = 0.27$. It presents two plateaus: a first one at $T_c \simeq 90$ K, related to the optimal doping ($p = 0.16$); a second one at $T_c \simeq 60$ K whose origin is believed to be due to the presence of the CDW order competing with superconductivity.

Material	$\mathbf{T_c}(K)$	$\lambda^{\mathbf{a}}; \lambda^{\mathbf{b}}; \lambda^{\mathbf{c}}$ (nm)	$\mathbf{\Delta}$ (meV)	$\xi_{\mathbf{ab}}; \xi_{\mathbf{c}}(nm)$	$\mathbf{H^{ab}_{c2}}, \mathbf{H^{c}_{c2}}(T)$
YBCO	94	150-300; $\lambda^a/1.3$; $\simeq 1000$	20-25	1-3; $\simeq 0.2$	250;120
Nb	9	44	1.5	40	3
NbN	16	200	1.5	5	20
Al	1.2	16	0.2	1600	0.01

Table 1.1: Main superconducting parameters for optimally doped YBCO, compared to some of the most common LTS materials[46, 47]. T_c is the critical temperature. $\lambda^a, \lambda^b, \lambda^c$ are respectively the London penetration depth along the $a-$, $b-$ and $c-$axis. Δ is the superconducting energy gap. ξ_{ab} and ξ_c are the coherence length along the $ab-$ plane and the $c-$axis, respectively. H^{ab}_{c2} and H^{c}_{c2} are respectively the upper crtical magnetic field along the $ab-$ plane and the $c-$axis.

1.3.1 Symmetry of the superconducting order parameter

As stated in section 1.2, the GL order parameter $\Psi(\vec{r})$ identifies a macroscopic wave function describing the collective superconducting state, and it is proportional to the energy gap $\Delta(\vec{r})$. Whilst GL equations are proven to be valid only in a range of temperature near T_c, as regards the pairing symmetry, the identification of the energy gap $\Delta(\vec{r})$ with the GL order parameter is expected to be valid in the whole temperature range below T_c. This arises from the fact that the order parameter represents the degree of the long-range phase coherence in the pair state[48]. Following BCS theory, in momentum space (k-space), the pair function Ψ can be written as: $\Psi(\vec{k}) = \Delta(\vec{k})/2E(\vec{k})$, where $E(\vec{k})$ is the quasiparticles energy dispersion. The gap symmetry can be determined experimentally even if a detailed knowledge of the microscopic pairing mechanism leading to superconductivity is missing. Many different experimental techniques (angle-resolved photoemission spectroscopy, specific heat, thermal conductivity, tricrystal experiment, etc) exist to determine the symmetry of the order parameter[48].

Differently from conventional LTS, which are s-wave, it is well established[48, 49] that cuprates are mainly characterized by a superconducting order parameter with a d-wave symmetry. In particular, a $d_{x^2-y^2}$ symmetry, with the superconducting wave function changing sign by a 90-degree rotation (see Fig.1.3).

Lobes with opposite sign exhibit a relative phase shift of π. Indeed, the energy gap

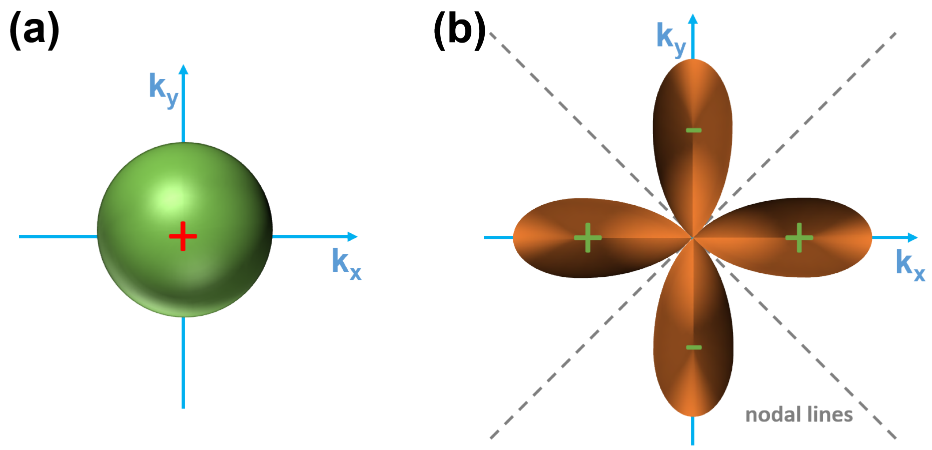

Figure 1.3: Sketch of a pure s-wave (a) and a pure d-wave (b) order parameter.

changes in the k-space as expressed by the following equation:

$$\Delta(\vec{k}) = \Delta_0(\cos(k_x a) - \cos(k_y a)), \tag{1.5}$$

where Δ_0 is the maximum value of $\Delta(\vec{k})$, and a is the in plane lattice constant. Equation (1.5) indicates that the cuprates superconducting state is gapless ($\Delta(\vec{k}) = 0$) along the (110) direction, i.e. nodal lines, which are rotated by 45° with respect to the direction of the lobes (see Fig. 1.3(b)). Such specific pairing has fundamental consequences on transport and thermodynamic properties, associated to the existence of zero-energy quasiparticles excitations at the lowest temperatures. The presence of a subdominant component for the superconducting order parameter has been predicted theoretically[50, 51], and recently demonstrated experimentally by several studies[24, 39]. The occurrence of a subdominant order parameter, possibly opening a full superconducting gap, will strongly alter the intrinsic AC dissipation channels of a $d-$wave superconductor and therefore affect the behaviour of the quantum devices studied in this thesis (see section 2.5.1 for a detailed discussion). Moreover, an accurate knowledge of the ground-state and of the low-energy excitations spectrum is a crucial step towards a better understanding of the origin of superconductivity in cuprates.

1.4 Thesis structure

The rest of this thesis is structured as follows: chapter 2 presents the theoretical framework of the investigated devices. It starts with the basics of the Josephson effect, with a specific focus on the modelling of the current-voltage characteristics of a Josephson junction. Next, the realization of HTS Josephson junctions implementing grain boundary techniques is introduced, and the effects of the $d-$wave symmetry of the superconducting order parameter on its transport properties are presented. In particular, the $d-$wave order parameter results in the formation of the so-called midgap states (Andreev bound states at the Fermi energy), which have a strong influence on the quantum coherence of a Josephson junction based quantum device. The employment of Josephson junctions as key building elements of superconducting quantum interference devices (SQUIDs) and of microwave transmon quantum bits is discussed. The chapter also includes the description of the co-planar waveguide (CPW) superconducting resonator, employed for readout operations of a transmon. The possible material related microwave loss mechanisms are discussed.

In chapter 3, the experimental details reported in this thesis and in all the appended papers are introduced. First, the modelling of the studied devices is discussed and all the characteristic parameters are listed. Then, the main fabrication methods are described, with a special attention at the realization of grain boundary bi-epitaxial Josephson junctions. The chapter is concluded with a description of the experimental techniques and the measurement setups employed for all the different investigations.

In chapter 4, the results from appended papers I and II, regarding the investigation of nanowire based YBCO nanoSQUIDs, are combined and presented. First, the transport properties are analyzed and a comparison to numerical methods is made. Then, the noise performances are presented and analyzed aiming at both the understanding of the microscopic mechanisms contributing to the measured noise and at a possible applications of the nanoSQUIDs as magnetic flux and field detectors. Extra experimental data, beyond those presented in paper I and II, are discussed to provide a more complete and clear picture.

In chapter 5, the experimental results from the investigation of the microwave losses coming from the materials involved in the fabrication of a YBCO CPW resonator, including both the dielectrics and the superconductor itself, are reported. The unloaded quality factor data in the millikelvin temperature range and at very low input power are analyzed in relation to the two-level systems model related to dielectric losses. Finally, the feasibility of a YBCO transmon qubit in the single photon limit is addressed. These results are discussed and reported in the appended papers III and IV.

In chapter 6, the realization and the first characterization of an all-YBCO transmon quantum bit, made out of bi-epitaxial Josephson junctions, are introduced. Transmission data through the qubit-cavity system, showing vacuum Rabi splitting, are presented. Decoherence intrinsic to the YBCO material, is analyzed in the presence of a large magnetic field up to 9 Tesla and a comparison to the DC-characterization of the employed Josephson junctions is made. An improvement of the transmon quantum coherence time at high magnetic field is observed and associated to a possible presence of a subdominant imaginary $s-$wave component of the order parameter.

Finally, in chapter 7, the thesis is concluded with a short summary of the main results, illustrating also possible outlook and outlining future works.

Chapter 2

Theoretical background

The aim of this chapter is to provide a theoretical background for the understanding of the experimental results presented in this thesis and in the appended papers. First, the physics of a conventional Josephson junction is described, and the implementation of grain boundaries to realize HTS junctions is discussed. Then a possible microscopic description of the Josephson effect in these structures is given in terms of the Andreev bound states. Next, the main mechanisms of a nanowire based SQUID is discussed in comparison to a Josephson junctions based one. After that, the concepts of a superconducting CPW resonator, together with a description of the microwave loss mechanisms involved for this device, are presented. Finally, the superconducting transmon qubit is introduced.

2.1 Josephson effect

Josephson junctions represent the key elements for various superconducting devices. The knowledge of the physics behind the Josephson effect is a crucial prerequisite. The superconducting state is regarded as a macroscopic quantum state, where a number of electrons pair and condense in the same ground state. This collective state is described by a single wave function as expressed by Eq.(1.2). If one considers two superconductors (SCs) separated by a macroscopic distance, each of them will be characterized by a superconducting quantum phase, which can be varied independently. However, if the separation distance l is reduced (short barrier), a coupling between the two SCs is created. The coupling is related to the overlapping of the two wave-functions across the barrier (see Fig.2.1). Cooper-pairs can tunnel through the barrier, and the two SCs plus the barrier are coupled. This phenomenon is known as *Josephson effect*[52]. The Josephson effect can not only take place through an insulating but also through a normal barrier, and by realizing various types of the so-called "weak links" (Dayem bridges[53], point contact[54], etc). Two superconductors separated by a weak link are referred to as Josephson junction (JJ).

2.1.1 Josephson equations

Lets consider two superconductors separated by a short tunneling barrier, as sketched in Fig.2.1. The superconducting states of the left and right SC, labeled SC_L and SC_R

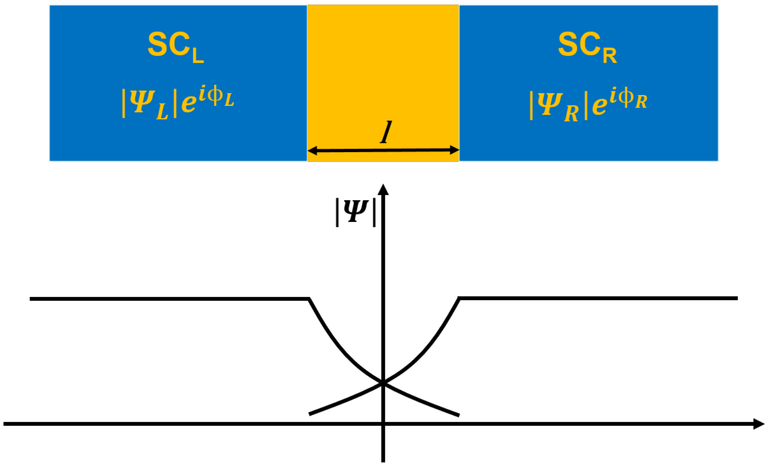

Figure 2.1: Schematic of a Josephson junction. Ψ_L and Ψ_R are respectively the wave function for the left (SC$_L$) and the right (SC$_R$) superconductor. The overlap of the wave functions along the barrier is shown.

respectively, are described by the wave functions: $\Psi_{L,R}(\vec{r}) = |\Psi_{L,R}(\vec{r})|e^{i\phi_{L,R}}$. Considering the coupling between the two SCs, and the consequent Cooper-pairs tunneling, the quantum state Ψ_J for the JJ is a superposition of basis states for $\Psi_L(\vec{r})$ and $\Psi_R(\vec{r})$. Without going into the details (see ref.[55] for the full derivation), the Josephson equations can be obtained starting from the time evolution of Ψ_J described by the Schrödinger equation, and using an Hamiltonian $H = H_L + H_R + H_T$. Here H_L and H_R describe the unperturbed states of the left and right SC respectively, whereas H_T (tunnelling Hamiltonian) the interaction between the states. The latter is written in terms of the coupling amplitude K, which represents a measure of the interaction between the two SCs, and depends on the specific properties of the junction (geometry, type of barrier, etc). Assuming $|\Psi_L(\vec{r})| = |\Psi_R(\vec{r})| = \sqrt{n_s}$, and setting $\phi = \phi_L - \phi_R$, we get the following expressions:

$$I = I_c \sin\phi \tag{2.1}$$

$$\frac{\partial\phi}{\partial t} = \frac{2e}{\hbar}V, \tag{2.2}$$

where $\hbar$ is the reduced Planck constant, and $I_c = 2K/\hbar n_s$ is known as critical current of the junction. Equations (2.1) and (2.2) are known as Josephson equations (JE). The second of the JE (2.2) states that at zero voltage $V = 0$, the phase difference ϕ across the JJ is constant (not necessarily zero), and from Eq. (2.1) current can flow through the barrier without any voltage drop up to a critical value I_c. This is known as DC-Josephson effect. If the current exceeds the critical value, a finite voltage drop across the JJ is observed and the phase difference ϕ varies over time as expressed by equation (2.2). At any finite voltage $V \neq 0$, with the phase difference ϕ evolving in time, Eq. (2.1) results in an alternating supercurrent. This is known as AC-Josephson effect. Consequences of the AC-Josephson effect can be observed as current steps on the DC I-V characteristics of a JJ, by irradiating the junction with a microwave signal. The AC-Josephson current locks to the microwave radiation, generating current steps at well defined constant voltage values: $V_n = \frac{nh}{2e} f_0$, known as Shapiro steps[56]. Here $n = (\pm 1, \pm 2, ...)$ is an integer number, and f_0 is the frequency of the microwave radiation.

From an electrical circuit point of view, a Josephson junction acts as a non-linear inductance. This can be easily obtained taking the time derivative of the Josephson current in Eq.(2.1):

$$\frac{\mathrm{d}I}{\mathrm{d}t} = I_c \cos\phi \frac{\mathrm{d}\phi}{\mathrm{d}t} = I_c \cos\phi \frac{2e}{\hbar} V, \tag{2.3}$$

thence the voltage across the junction writes as:

$$V = \frac{\hbar}{2eI_c \cos\phi} \frac{\mathrm{d}I}{\mathrm{d}t}. \tag{2.4}$$

Now, recalling that $V = L\frac{dI}{dt}$, one obtains the following equation for the Josephson inductance:

$$L_J = \frac{\hbar}{2eI_c \cos\phi} = \frac{\Phi_0}{2\pi I_c \cos\phi}, \tag{2.5}$$

where $\Phi_0 = h/2e$ is the magnetic flux quantum. Equation (2.5) indicates a diverging Josephson inductance at $\phi = (2n+1)\frac{\pi}{2}$, and that in general L_J is not linear as a consequence of the $1/\cos\phi$ term. Since it behaves as an inductance, an important property of a Josephson junction is the capability to store energy from the tunnelling of Cooper-pairs, known as Josephson energy E_{JJ}. The Josephson energy can be derived by taking the time integral of the power across the junction, as follows:

$$E_{JJ}(\phi) = \int IV \,\mathrm{d}t = \int I_c \sin\phi \frac{\hbar}{2e} \frac{\mathrm{d}\phi}{\mathrm{d}t} \,\mathrm{d}t = -\frac{I_c\hbar}{2e}\cos\phi = -E_J\cos\phi, \tag{2.6}$$

where $E_J = \frac{I_c\hbar}{2e} = \frac{I_c\Phi_0}{2\pi}$ is the maximum Josephson energy. The non-linearity of the Josephson energy is extremely important to build up superconducting quantum circuits, as it will be discussed in section 2.5.

2.1.2 RCSJ model for a Josephson junction

The measurement of the IV characteristic of a Josephson junction is typically performed by connecting the JJ to a bias current source and measuring the voltage drop across the junction. While equation (2.1) suffices to describe the zero voltage DC properties of a JJ, a more complete description is required for the finite voltage state. A simple way to describe the behaviour of a current biased Josephson junction is represented by the so-called resistively and capacitively shunted junction (RCSJ) model. Within this model the JJ is included in a lumped elements circuit (see Fig.2.2) together with a resistor R, accounting for the dissipation due to the presence of quasiparticles in the finite voltage state, and a capacitor C, representing the capacitance between the two superconducting electrodes both across the barrier and the stray capacitance through the dielectric substrate. The appropriate value for R is of the order of the normal resistance R_N for an SNS junction, an ScS junction, and an SIS junction close to T_c. Here the normal resistance R_N is the junction resistance measured at voltage values above 2Δ. According to BCS theory, the appropriate value of R for high quality SIS junctions at voltages smaller than 2Δ increases exponentially with lowering the temperature as $R_N e^{\Delta/k_B T}$, which takes into account the freezing-out of quasiparticles at low temperatures. Indeed, R is voltage dependent and should be chosen in the best possible way to represent the highly non-linear quasiparticles conductance. Referring to the circuit in Fig.2.2, the total current resulting from the sum

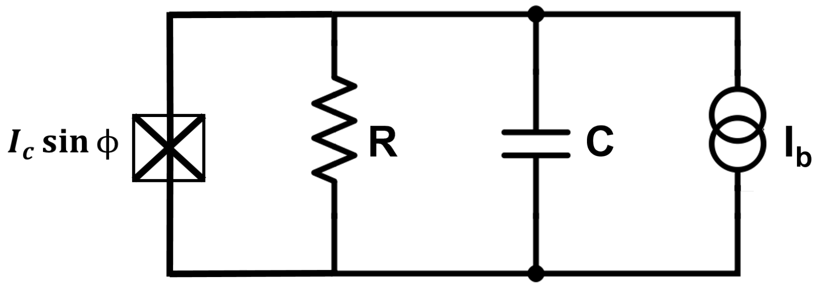

Figure 2.2: Sketch of the current biased RCSJ circuit, showing the lumped elements used to model a Josephson junction. R models the dissipation in the normal state; C accounts for the capacitance across the barrier and superconductors/substrate stray capacitance.

of the current through the JJ, the resistor R and the displacement current through the shunting capacitance C, can be derived equating it to the bias current I_b, and writes as follows:

$$I_b = I_c \sin\phi + \frac{V}{R} + C\frac{dV}{dt}. \tag{2.7}$$

Using the second Josephson equation (2.2), it becomes:

$$I_b = I_c \sin\phi + \frac{\hbar}{2eR}\frac{d\phi}{dt} + \frac{\hbar C}{2e}\frac{d^2\phi}{dt^2}. \tag{2.8}$$

Introducing the dimensionless parameters: $\tau = \omega_p t$, where $\omega_p = \sqrt{\frac{2eI_c}{\hbar C}}$ is the so-called "plasma frequency", and the quality factor $Q = \omega_p RC$, equation (2.8) writes as:

$$\frac{I_b}{I_c} = \sin\phi + \frac{1}{Q}\frac{d\phi}{d\tau} + \frac{d^2\phi}{d\tau^2}. \tag{2.9}$$

The quality factor Q is directly related to the damping factor $\beta_c = \frac{2e}{\hbar} I_c R^2 C$, introduced by Stewart and McCumber[57], via the relation $Q = \sqrt{\beta_c}$. The RCSJ model described by equation (2.8 or 2.9) has a mechanical analogy that helps to picture the time evolution of the superconducting phase. The dynamics of the phase, in fact, is qualitatively like the one of a particle of mass $m_\phi = (\hbar/2e)^2 C$ moving in a *tilted washboard* potential $U(\phi)$ (see Fig. 2.3) given by:

$$U(\phi) = -E_J \cos\phi - \frac{\hbar I_b}{2e}\phi, \tag{2.10}$$

and subject to a drag force: $(\hbar/2e)^2(1/R)(d\phi/dt)$. Within this mechanical analogy, the phase difference ϕ represents the position coordinate of the particle; the maximum Josephson energy E_J is the characteristic energy scale involved in the phase dynamics ($2E_J \equiv \Delta U$ coincides with the barrier height at $I_b = 0$), and the applied bias current I_b causes a tilt of the potential. At zero temperature $T = 0$, when the bias current exceeds the maximum critical current ($I_b > I_c$) the phase particle starts to move along the potential (the junction is in the running mode) following a trajectory that depends on the dissipation $\alpha_d = 1/Q$. The smaller is the Q factor, the steeper is the trajectory, represented by an arrow in Fig.2.3. The I-V characteristic is then determined by the time evolution of the

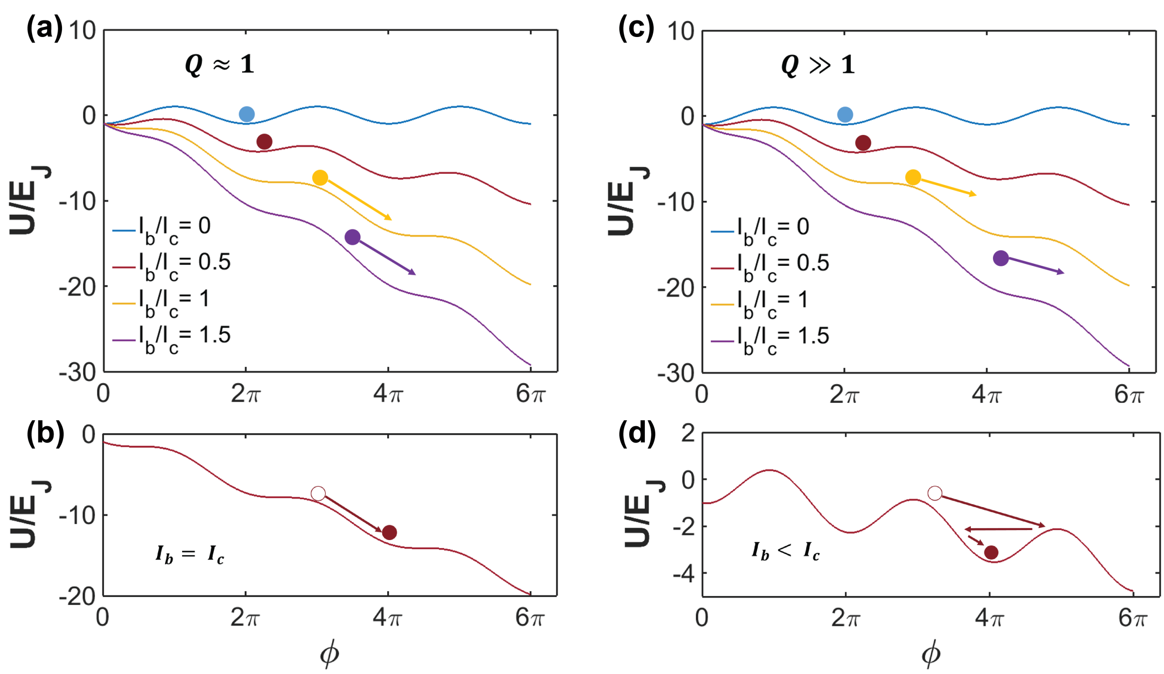

Figure 2.3: Plot of the washboard potential expressed by Eq. (2.10) as a function of the phase ϕ for bias current sweep from $I_b = 0$ to $I_b = 1.5I_c$. The fictitious phase particle for the over-damped (a) and under-damped (c) case are depicted. (b) and (d) Retrapping process of the fictitious phase particle when the bias current is decreased from a value $I_b \gg I_c$ towards zero.

phase difference ϕ. Two main regimes can be distinguished depending on the value of the damping parameter β_c:

- $\beta_c \ll 1$, *over-damped* regime;
- $\beta_c \gg 1$, *under-damped* regime.

In the over-damped regime, the capacitance is negligible and the second time derivative in equation (2.8) can be neglected. Integrating the resulting equation over time, one obtains the average voltage:

$$< V >= R(I_b^2 - I_c^2)^{1/2}. \tag{2.11}$$

If $I_b < I_c$, the phase particle remains trapped in a local minimum of the washboard potential, and the average voltage across the junction is zero (superconducting state). For $I_b > I_c$ the phase particle is in the running regime, and a voltage drop is observed as expressed by eq.(2.11). By further increasing I_b the voltage drop smoothly increases (see Fig. 2.4(a)) following eq.(2.11), until it behaves like a normal resistor described by Ohm's law ($V = I_bR$ for $I_b \gg I_c$). Then, by reducing back the bias current, the phase particle gets trapped in the potential well once I_b reaches I_c (see Fig.2.3(b)).

In the under-damped regime, the capacitance can not be neglected and eq.(2.8) has to be solved numerically to obtain the time averaged voltage $< V >$. As result of the low dissipation ($Q > 1$), the I-V characteristic of an under-damped Josephson junction is hysteretic (see Fig. 2.4(b)). First, when I_b exceeds I_c, the phase particle follows a straight trajectory (see Fig. 2.3(c)) and as a result the voltage V jumps discontinously from $V = 0$ up to a finite value. Assuming a voltage independent resistance $R = R_N$, the voltage would assume the normal value $V = I_c R_N$. Then, due to low dissipation, once the bias current I_b is reduced back to I_c, the phase particle is not immediately trapped back by the potential well. In fact, the phase particle gets only retrapped once I_b reaches the retrapping current $I_r \simeq \frac{4I_c}{\pi Q}$[31](see Fig.2.3(d)), which depends on the quality factor.

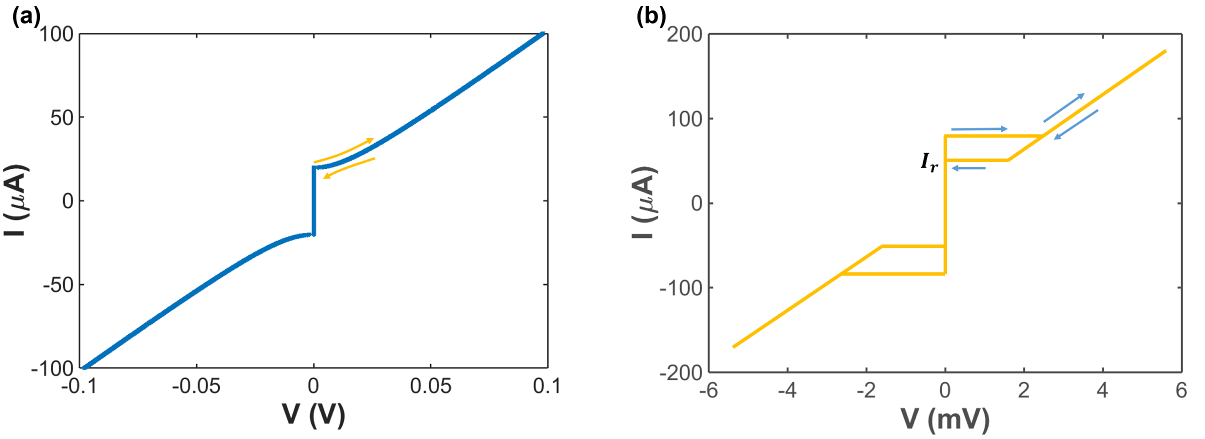

Figure 2.4: Sketch of typical IV characteristics for over-damped (a) and under-damped (b) Josephson junctions.

2.1.3 Grain boundary HTS Josephson junctions

The simplest way of realizing a Josephson junction is to interpose a thin insulating barrier between two superconducting electrodes. This technique is unfortunately very difficult to implement with HTSs. The reason of this difficulty lies mainly in the very short coherence length (see Table 1.1), but also in the complex crystal structure and the high instability of these materials. An alternative way is to use a controlled grain boundary (GB) to realize a JJ[58]. A GB is formed at the region between grains with different crystallographic orientations. GBs are normally classified in terms of the rotation necessary to go from one grain to the other, and they are associated to a high degree of disorder. In fact, in order to accommodate for the lattice mismatch between the two crystals in contact, different types of defects are formed (dislocations, changes in the stoichiometry, inter-granular phases and/or micro-cracks). Such disorder is responsible for the poor electrical transport properties (low value of the critical current density J_c) of polycrystalline HTS. However, GBs characterized by a large enough angle can act as a tunneling barrier, and can form very high quality Josephson junctions[58]. Therefore, high-T_c superconducting GBs are very appealing both for applications and basic physics studies.

The main fabrication techniques for the realization of controlled GBs are:

- bicrystal junctions[59], for which a special substrate, obtained by assembling two pieces of the same material characterized by different crystallographic orientations (see Fig.2.5(a)), is required. The HTS film deposited on such a substrate grows epitaxially according to the different crystal orientations and a GB is formed at the bicrystal line. Bicrystal junctions have rather reproducible properties, but they are not versatile, i.e. they do not provide freedom in the design.

- step-edge junctions[60]: they are obtained by growing a HTS film on a substrate where a step has been etched (see Fig.2.5(b)). With this technique two GBs are formed, one at the bottom and another at the top of the step. The presence of two junctions in series is detrimental for most applications. Possible approaches to solve this issue consist in realizing junctions at the top and bottom of the step with very dissimilar critical currents [61] or creating a smooth bottom edge, such that the bottom GB junction does not form[62].

- biepitaxial junctions[63]: they make use of of patterned template layers (seed layers) to change the epitaxial relations between the HTS thin films and the substrate. A possible example is shown in Fig.2.5(c), where the YBCO grows c-axis oriented on the seed layer whereas is (103) oriented on the bare substrate. The GB is formed at the interface between the two different growth orientations similar to the bicrystal case. The bi-epitaxial technique is the one used in this thesis work. More details of the fabrication methods are reported in section 3.2.

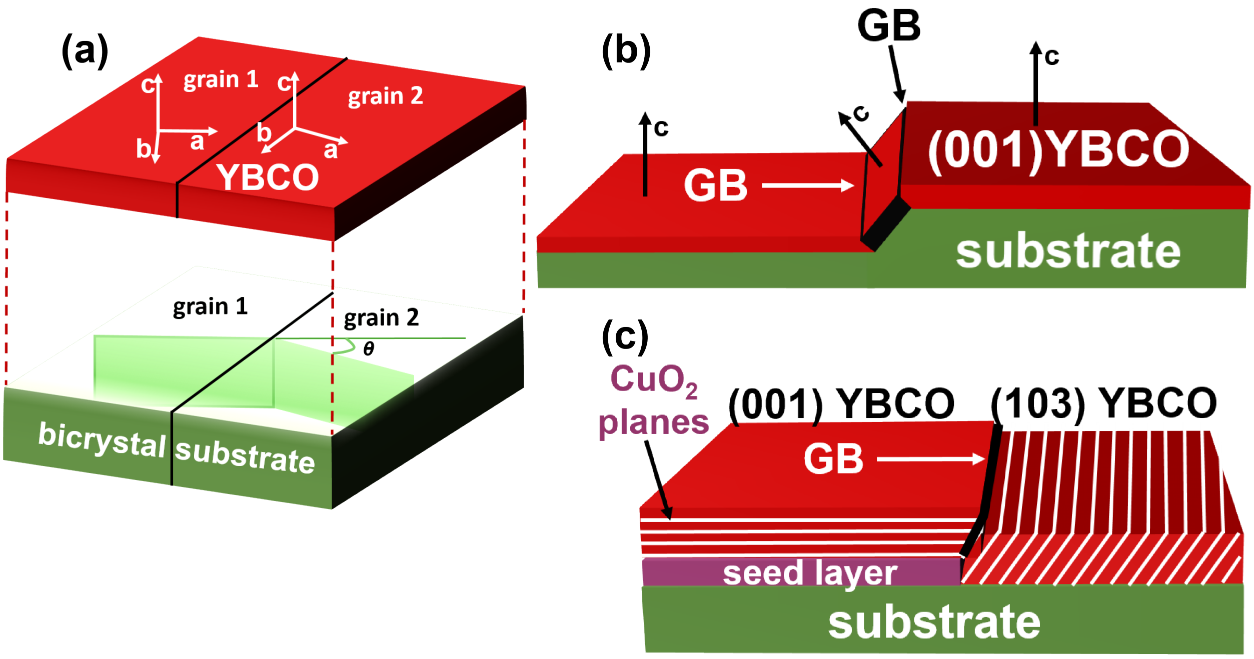

Figure 2.5: Cartoon of the three main different grain boundary technologies employed for cuprates high critical temperature superconductors: bicrystal (a), step-edge (b) and bi-epitaxial (c).

Among the different techniques listed above, the bi-epitaxial one is the most versatile. In fact it allows to place the GBs freely on the substrate and to realize GBs characterized by different Josephson transport directions with respect to the orientation of the order parameters in the electrodes. Different grain boundary angles α are obtained by changing the orientation of the GB line, defined by the seed layer, with respect to the in plane orientation of the substrate, as it is shown in figure 2.6. Here the angle α is measured from the [1-10] in-plane direction of the (110)LSAT substrate. Depending on α, different GB structures can be obtained.

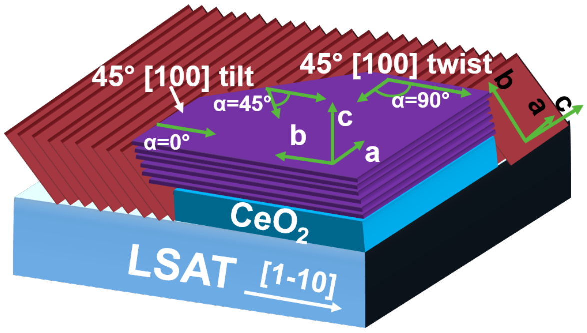

Figure 2.6: Cartoon of bi-epitaxial grain boundary junctions. The main different GB structures used in this thesis work are labelled.

The grain boundaries are classified as *tilt* if the rotation to go from one grain to the other is around an axis perpendicular to the normal $\hat{n}$ to the boundary (see Fig.2.7(a)), as *twist* if the rotational axis is parallel to $\hat{n}$ (see Fig.2.7(b)). Figure 2.7 shows a schematic of a 45°[010]-tilt (a) and of a 45°[100]-twist GB junction (b), which in this thesis are respectively referred to as $\alpha = 0°$ and $\alpha = 90°$ junction.

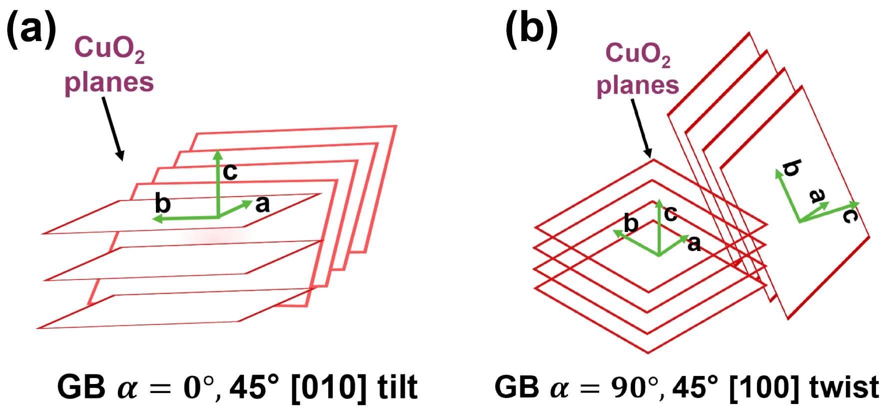

Figure 2.7: Cartoon of a GB $\alpha = 0°$, 45°[010]-tilt (a), and a GB $\alpha = 90°$, 45°[100]-twist(b).

Different angles α characterize GBs with different structures, but also with different transport properties due to the $d-$wave symmetry of the order parameter. This aspect has great influence in the transport properties of the junctions. The current-phase relation, in fact, will strongly depend on the relative orientation of the order parameter in the two junction electrodes[64]. It has been shown that the critical current density J_c of a $d-$wave junction depends on the orientation of the order parameter with respect to the GB line, as expressed by[65]:

$$J_c = J_{c,max}(n_x^2 - n_y^2)_L(n_x^2 - n_y^2)_R \sin\phi, \tag{2.12}$$

where n_x and n_y are the components of the normal vector to the GB interface $\hat{n}$ along the crystallographic axes, subscripts L and R refer respectively to the left and the right junction electrode. Equation (2.12) implies that junctions with the lobes of the order parameter facing each other have a larger J_c compared to lobe to node or node to node junctions. In general the GB interface of a HTS is characterized by a meandering structure due to the granularity of the films, with facets on the length scale of 100-200 nm. The faceting results in a GB with different interface angles, as schematically sketched in Fig.2.8. This influences the transport properties of the junctions, which will then be the result of an averaging effect over the different facets. According to Eq.(2.12) each facet is, in fact, characterized by a different J_c. In order to reduce the number of facets at the GB

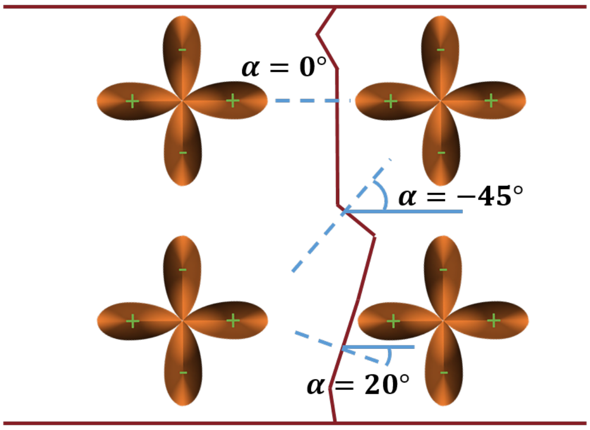

Figure 2.8: Schematic of the faceting of a grain boundary interface in combination with the $d-$wave symmetry of the order parameter.

interface, which strongly depends on the growth conditions and the GB angle, sub-micron sized GB junctions are necessary.

In this thesis work, nanometer sized bi-epitaxial GB YBCO junctions are used as key element for building superconducting quantum circuits to study fundamental properties of cuprates.

2.2 Andreev bound states in high-T_c junctions

Andreev bound states provide a possible microscopic description of Josephson transport in grain boundary junctions. Lets first consider an interface between a normal metal and a superconductor (NS), an electron moving from the normal electrode towards the interface, with energy $|E| < \Delta$, can not penetrate into the superconductor. It can either be normally reflected as electron with opposite momentum or as hole with the same momentum, generating a Cooper pair in the superconductor (Andreev reflection). The concept of electron-hole conversion, i.e. "on a superconductor surface, electrons are reflected as holes and holes are reflected as electrons"[66], was introduced by Andreev[67]. Andreev reflections induce the formation of surface states. In fact, each Andreev reflection is associated to a shift of the phase φ of the electron/hole wavefunction. A surface state then is associated to a closed quasiparticle trajectory (see Fig.2.9(a)), and its energy can be obtained from the Bohr-Sommerfeld quantization condition, according to which the total phase accumulated along a closed cycle has to be equal to an integer number n of 2π: $\oint_\Gamma \nabla\varphi \, d\Gamma = 2n\pi$.

The energy of these states depends on the surface properties and on the symmetry of the superconducting order parameter (or gap Δ). In fact, while for an $s-$wave superconductor surface states at the Fermi energy can not exist, for a d-wave superconductor with specific orientations of the order parameter, the surface states can occur at the Fermi energy. These are known as *midgap states* (MGS). The presence of MGS is due to the fact that the phase of the $d-$wave order parameter (gap) is angle dependent[1](see Fig. 2.9(b)). Therefore, for some specific quasiparticle trajectories, the probed order parameter (gap)

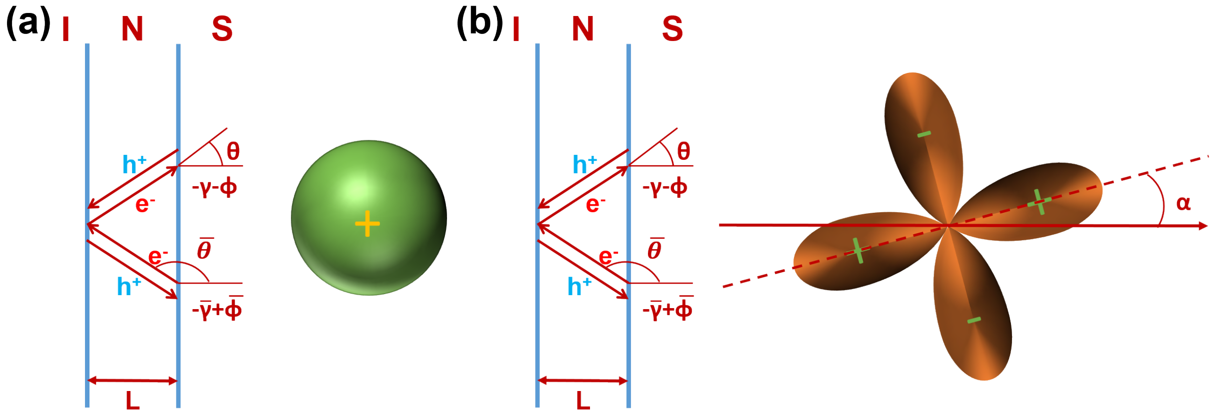

Figure 2.9: Sketch of an INS interface with an isotropic s-wave superconductor (a) and an anisotropic d-wave superconductor (b), showing a quasiparticle path generating the surface state. L is the size of the normal region N, which models the gap suppression in the vicinity of the surface. In (b) α represents the orientation angle of the order parameter in respect to the surface normal direction.

shows a different sign before and after reflection. The observation of the MGS from electrical transport measurement provides a strong proof of a d-wave symmetric order parameter[68]. In the presence of a subdominant imaginary s- or d-wave order parameter, which could be energetically favorable when the main d-wave gap is suppressed and at low temperatures[50, 69, 70, 51, 71], MGS are significantly modified. The MGS, in fact, are shifted away from the Fermi energy to the energy level of the subdominant gap.

In superconducting junctions, the surface states can hybridize and create stationary states for the whole junction, known as Andreev bound states. For high-T_c superconductors, due to the presence of MGS, zero energy quasiparticle bound states (ZEBS) can be built. In general being associated to charge transfer, Andreev bound states can carry current, and consequently they provide a microscopic description of the DC-Josephson transport.

In the next section, following [66], the effect of midgap states on DC-Josephson transport for specific orientations of the d-wave order parameter will be examined. A more detailed discussion about Andreev bound states in $d-$wave superconductors can be found in ref.[66] and references therein.

[1] d-wave symmetry for HTS is discussed in details in section 1.3.1

2.2.1 Midgap states influence on DC-Josephson effect

In a Josephson junction the surface states from the two superconducting electrodes couple and form coherent bound states, known as Andreev bound states. Lets first consider the case of a superconductor-normal-superconductor (SNS) junction, as sketched in figure 2.10 (a). In this structure an electron from the normal region, with energy lower than the

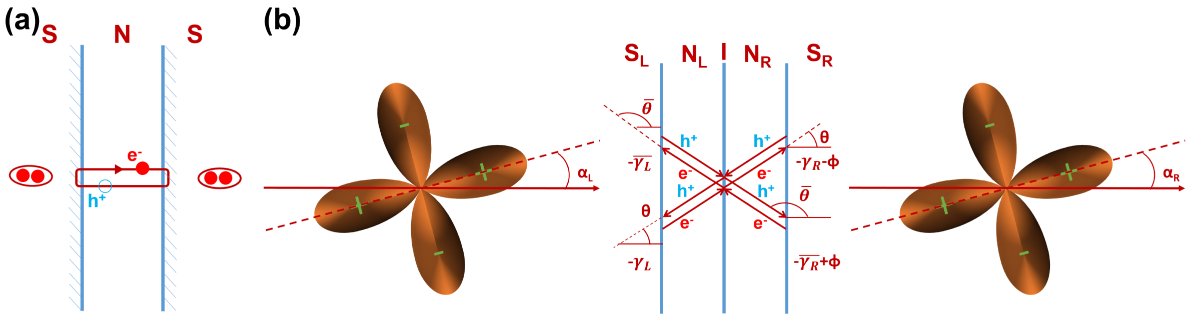

Figure 2.10: (a) Sketch of an SNS junction showing the formation of a bound states below the gap energy. (b) Sketch of an SNINS junction with anisotropic *d*-wave superconductors. A quasiparticle closed trajectory forming zero energy bound states is shown. $\alpha_{L,R}$ represents the orientation angle of the order parameter with respect to the surface normal direction, respectively for the left and right superconductor. The normal regions $N_{L,R}$ model the gap suppression in the vicinity of the surface.

gap and traveling towards the right superconductor, can experience an Andreev reflection into a hole with same momentum but opposite velocity. The hole will then travel towards the left superconductor getting Andreev reflected at the SN interface. It is like the quasiparticle is trapped between the two superconducting electrodes: a bound state is created. A similar scenario can take place for a HTS grain boundary Josephson junction (see Fig. 2.10 (b) where the normal regions N model a gap suppression in the vicinity of the surface). Here, one can think of the Andreev bound states as a result of the hybridization of the surface states at both the left and the right side of the insulating tunnel barrier. Because of charge conservation, for each reflection on the right interface, a Cooper-pair is transferred to the right superconductor. On the other hand, for each hole reflection on the left interface a Cooper-pair is absorbed from the left superconductor. This results in a DC-Josephson current through the whole device, which means that Andreev bound states can provide a microscopic description of Josephson effect. Andreev states depend on both the transparency D of the tunneling barrier separating the two superconducting electrodes and the phase difference ϕ across the junction. The latter implies a phase dispersion of the energy of the Andreev levels $E(\phi)$. In junctions with many transport channels one talks about Andreev bands, where the width depends on D.

Within the Andreev states framework, junctions implementing *d*-wave superconductors are characterized by a Josephson current strongly dependent on the orientation (α_L and α_R) of the order parameter in the superconducting electrodes (see Fig. 2.10 (b)). One can consider three different cases:

1. no MGS at both sides of the junction;

2. MGS at both sides of the junction;

3. MGS at only one side of the junction.

In the following the short junction limit is considered for all the three cases, with the coherence length in the N region $\hbar v_F/\pi\Delta$ much larger than L. The first case is obtained when the order parameter orientation on both sides is equal to zero (or $\pi/2$): $\alpha_L = \alpha_R = 0$. The pure d_0/d_0 junctions behave as s-wave superconducting electrodes, with the Josephson current dominated by Andreev states whose energy is close to the gap and that are characterized by an energy dispersion proportional to the junction transparency D (see Fig.2.11(a)). Here the phase dependent energy difference between Andreev bands is known as *minigap* δ, the quasiparticle energy gap in the normal metal due to proximity effect with the superconductor.

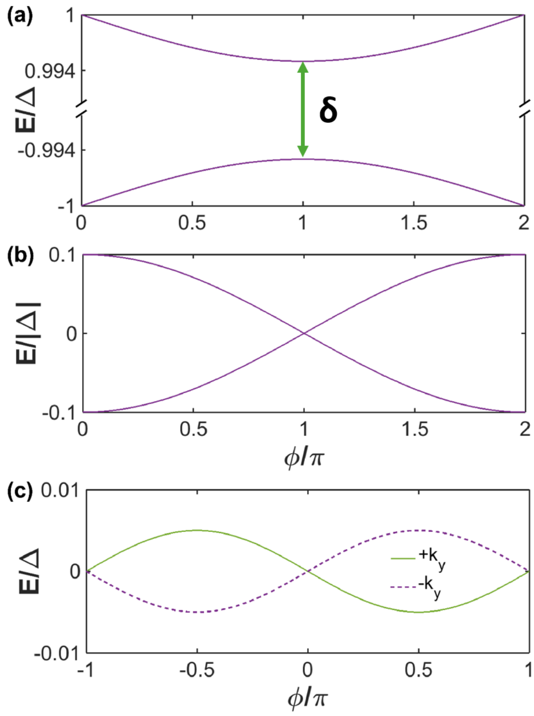

Figure 2.11: Andreev bound states energy dispersion for three different $d-$wave junctions: d_0/d_0 (a), $d_{\pi/4}/d_{\pi/4}$ (b) and $d_0/d_{\pi/4}$ (c). In all the three cases the junction transparency is $D = 0.01$.

The second case, instead, is realized when $\alpha_L = \pi/4$ and $\alpha_R = \pm\pi/4$. The pure $d_{\pi/4}/d_{\pi/4}$ junctions are characterized by specific transport properties related to the presence of the MGS such as: critical current I_c values proportional to $\sqrt{D}$ at low temperature and an anomalous temperature dependence. In this case, the energy dispersion is given by[66] (plotted in Fig.2.11(b)):

$$E_{\pm} = \pm|\Delta|\sqrt{D}\cos\frac{\phi}{2}. \tag{2.13}$$

At zero temperature, only the energy level below the Fermi level is populated and the current of the MGS can be written as:

$$J_{MGS} = \frac{2ek_F}{\hbar} \left\langle |\Delta|\sqrt{D} \right\rangle \sin\frac{\phi}{2}\mathrm{sgn}\left(\cos\frac{\phi}{2}\right). \tag{2.14}$$

Equation (2.14) implies a critical Josephson current proportional to $\sqrt{D}$, which is related to the resonant coupling of the MGS. For low transparancy junctions ($D \ll 1$), Eq.(2.14) results in a much larger Josephson current compared to the conventional Josephson transport ($\propto D$). At finite temperatures, with $E_+ < k_BT$, the upper level also gets populated. Since the current carried by the two MGS energies $E_\pm$ flow in opposite directions ($J_+ = -J_-$), the total current due to the MGS decreases and its temperature dependence is expressed as[66]:

$$J_{MGS} = -\frac{2ek_F}{\hbar} \left\langle \frac{dE_+}{d\phi} \tanh\left(\frac{E_+}{2k_BT}\right) \right\rangle. \tag{2.15}$$

Equation (2.15) indicates that the Josephson current for temperatures T such that $k_BT \gg E_+$ ($\tanh x \simeq x$) is proportional to $1/T$.

Finally for the third case, which can be obtained with orientation angles $\alpha_L = 0$ and $\alpha_R = \pi/4$, both an MGS band and a band at the gap edge are formed. The energy dispersion of a specific MGS is shown in Fig.2.11(c). A $d_0/d_{\pi/4}$ junction is characterized by π periodicity of the current-phase-relation and time-reversal symmetry breaking, which results in the formation of surface currents producing magnetic field at the junction interface.

In real grain boundary high-T_c junctions, all the three cases can occur due to meandering of the GB line (faceting, see section 2.1.3) and scattering at the I interface. Thus, the total Josephson current is the result of a weighted sum of the three different types. A positive curvature of the $I_c(T)$ at low temperature might represent a hint of the presence of MGS in GB junctions.

2.3 Superconducting QUantum Interference Device

In this thesis work, nanometer sized YBCO superconducting quantum interference devices (SQUIDs) are identified as potential tools to employ for the study of the fluxoid quantization at the nanoscale via electrical transport measurement. Moreover, they are also analyzed in the perspective of possible future applications as magnetic flux or field sensors. A SQUID, in fact, is a magnetic flux to voltage transducer, and it is one of the most sensitive magnetic field detectors. It consists of a superconducting loop interrupted by two Josephson junctions, or in general by two weak links. A cartoon of a typical current biased DC-SQUID is presented in figure 2.12.

In most of the cases, especially for HTS grain boundary junctions, the two JJs are characterized by different values of the critical current ($I_{c1} \neq I_{c2}$). In order to describe the physics of the SQUID, the dependence of the critical current as a function of the externally applied magnetic field needs to be derived. In the presence of an externally applied magnetic flux Φ_e, as for any superconducting loop, the fluxoid quantization[2] holds

[2]Since the wave function (order parameter) for a superconducting state is single valued, the fluxoid through a superconducting loop can only be an integer multiple of the flux quantum Φ_0[31].

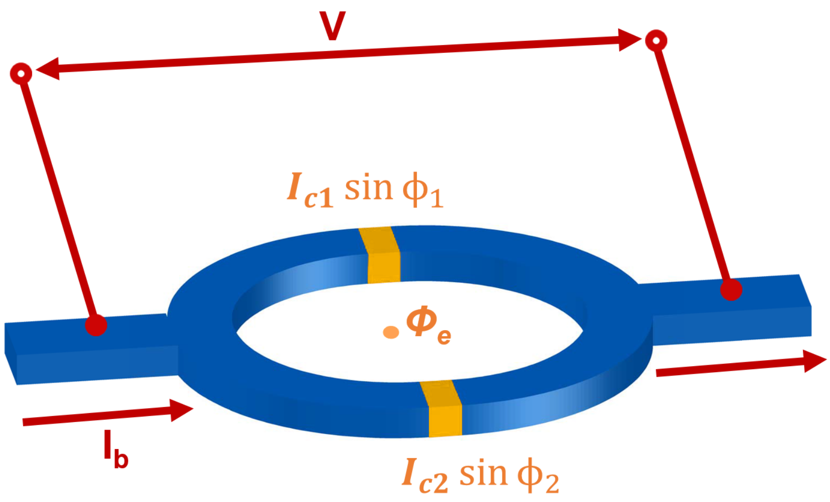

Figure 2.12: Cartoon of a current biased SQUID. A superconducting loop (blue) is interrupted by two Josephson junctions formed by two weak links (orange).

for a SQUID as well. The fluxoid quantization writes as:

$$2\pi n = \phi_1 - \phi_2 + 2\pi \frac{\Phi}{\Phi_0}, \tag{2.16}$$

where $\Phi_0 = h/2e$ is the flux quantum and $\Phi = \Phi_e + LI_s$ is the effective magnetic flux, with $L = L_1 + L_2$ the total SQUID loop inductance and I_s the screening current. The total current flowing in a SQUID is given by the sum of the currents flowing through the two JJs:

$$I_{SQ} = I_{c1} \sin \phi_1 + I_{c2} \sin \phi_2. \tag{2.17}$$

In the case of a symmetric SQUID, i.e. same critical currents for the two JJs ($I_{c1} = I_{c2}$), neglecting both the SQUID inductance ($L \simeq 0$) and the flux through the junctions ($\Phi_J \simeq 0$), the $I_c(\Phi_e)$ can be obtained by substituting ϕ_1 from eq.(2.16) into eq.(2.17), and then maximizing the resulting expression for the current I_{SQ} with respect to ϕ_2. One obtains that the critical current I_c of such SQUID device modulates cosinusoidally with the external magnetic flux as expressed by:

$$I_c = 2I_{c1} \left| \cos \left(\frac{\pi \Phi_e}{\Phi_0} \right) \right|. \tag{2.18}$$

In the general case of a finite loop of inductance $L = L_1 + L_2$, taking into account an asymmetry of the SQUID arms inductances ($L_1 \neq L_2$), the fluxoid quantization writes as follows:

$$2\pi n = \phi_1 - \phi_2 + 2\pi \frac{\Phi}{\Phi_0} + 2\pi \beta_{L1} \sin \phi 1 + 2\pi \beta_{L2} \sin \phi 2, \tag{2.19}$$

where $\beta_{L1,L2} = L_{1,2} I_{c1,c2}/\Phi_0$ are the screening inductance factors. In order to obtain the critical current modulation $I_c(\Phi_e)$ as a function of the externally applied magnetic flux, the maximum of the total current I_{SQ} (eq.(2.17)) has to be determined with the constrain expressed by eq.(2.19) for the phases $\phi_{1,2}$. Different methods can be implemented for the derivation of $I_c(\Phi_e)$. The most suitable is based on Lagrange multipliers reported by Tsang and van Duzer in ref.[72], with which two equations relating Φ_e and $\phi_{1,2}$ at the critical current are obtained. A numerical iteration is then needed to compute $I_c(\Phi_e)$. Details of the numerical computation are reported in ref.[72, 73]. In figure 2.13 (a), the critical current modulation as a function of the external flux for different values of β_L is plotted. Larger values of β_L imply a smaller modulation depth. It has been shown[74] that

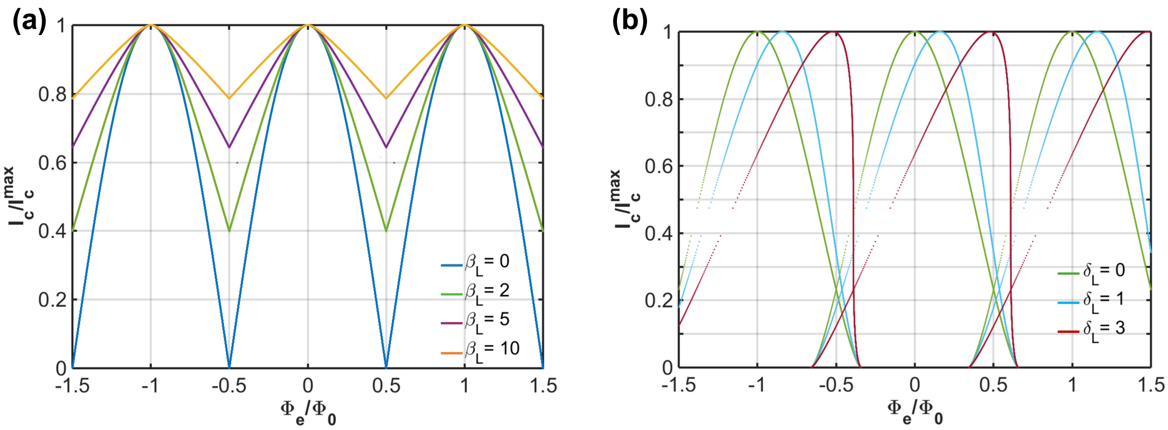

Figure 2.13: (a) Critical current modulation as a function of the externally applied magnetic flux for four different values of the screening inductance factor β_L and $\delta_L = 0$. (b) Critical current modulation as a function of the externally applied magnetic flux for three different values of the SQUID arms inductances asymmetry parameter δ_L. The curves have been calculated following ref.[72, 73]. Here β_L is set to 1.

the relative modulation depth scales as $\frac{\Delta I_c}{I_c} = \frac{1}{\beta_L}$, in the limit $I_c^{max} L \gg \Phi_0$. Figure 2.13 (b) shows the critical current modulation for different values of the asymmetry parameter for the inductances of the SQUID arms: $\delta_L = \frac{L_1 - L_2}{L_1 + L_2}$. Asymmetry in the SQUID arms inductances results in a slanting of the critical current modulation pattern.

2.3.1 Flux noise in a SQUID

As for any other detector, the knowledge of the noise properties is fundamental to establish the possible applications of the SQUID. Being the SQUID a magnetic flux detector, one is mainly interested in the modelling of the flux noise such that it would be possible to optimize the device performances.

The white flux noise limiting the performance of a DC-SQUID originates from voltage noise in the shunting resistance of the Josephson junctions. Each of the current biased JJs in a SQUID can be modelled as a parallel lumped element circuit (see Fig. 2.14), including also a resistor R and a capacitor C (see section 2.1.2). Within this model, at finite temperature T, the limiting flux noise $S_\Phi^{1/2}$ can be calculated as Johnson noise across the resistor R[75, 76], which writes as:

$$S_\Phi^{1/2} = L\sqrt{\frac{4k_B T}{R}}. \tag{2.20}$$

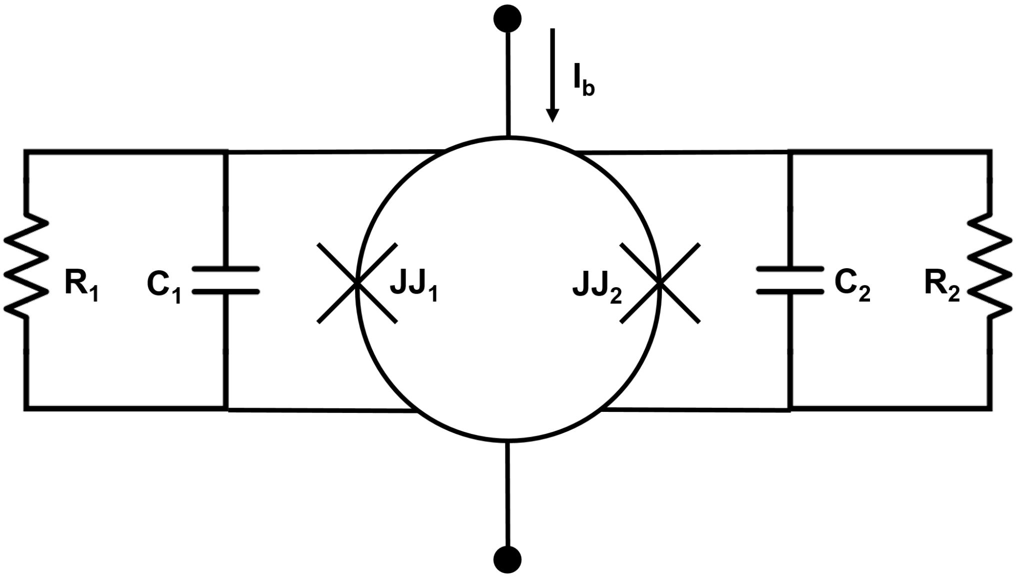

Figure 2.14: Schematic circuit of a current biased SQUID. Each JJ is modelled as a lumped element circuit with a resistor R and a capacitor C in parallel to the junction.

Assuming $\beta_L \sim 1$ and $\beta_C \sim 1$, one obtains:

$$\begin{aligned} \beta_L \sim= \frac{LI_c}{\Phi_0} \sim 1 \quad &\Rightarrow \quad L \sim \frac{\Phi_0}{I_c} \\ \beta_C \sim \frac{2\pi}{\Phi_0} I_c R^2 C \sim 1 \quad &\Rightarrow \quad R \sim \sqrt{\frac{\Phi_0}{2\pi I_c C}}. \end{aligned} \tag{2.21}$$

Substituting equations (2.21) in Eq. (2.20), the flux noise can be written as follows:

$$S_\Phi^{1/2} = \frac{8}{\sqrt{2}} (k_b T L^{3/2} C^{1/2})^{1/2}, \tag{2.22}$$

where L is the total SQUID inductance[3]. From equation (2.22) it infers clearly that, in order to improve the flux sensitivity, one needs to decrease both the SQUID inductance L and the junction capacitance C. A reduction of L is realized by a smaller size of the SQUID loop, whereas a smaller cross section of the JJ will result in a lower value of C. Modern patterning techniques allow for the realization of SQUID loop size in the nanometer range (nanoSQUID). However, reducing the JJ cross section to the nanometer scale might result in a deterioration of the tunneling barrier and therefore of the transport properties of the junction, with an increase of the critical current/normal resistance noise. Moreover, both the critical current and temperature of the JJ will decrease, limiting the operational temperature of the SQUID device to values far below the T_c of the superconducting material. The latter drawback is particularly pronounced when high-T_c superconductors are employed. One of the main advantages of using HTS, in fact, is the possibility to extend the operational temperature of the sensor above the nitrogen boiling temperature (see section 4 for more details).

[3]Equation (2.22) is also obtained from numerical calculations in the limit set by the expressions (2.21)[77].

$1/f$ flux noise in SQUIDs

Noise power spectra proportional to $1/f$ at low frequency are observed in many different physical systems and devices based on various materials, including semiconductors, normal metals and superconductors. Moreover, the $1/f$ noise intensity depends not only on the material but also on the technological methods used to realize the different devices. Several processes, characterized by different relaxation rates γ_r, have been identified as possible sources of $1/f$ noise. In dielectrics, for example, there exist low-energy excitations that result in peculiar temperature dependencies of the dielectric permittivity at low temperature[78], as it will be discussed in section 2.4. These processes are modelled assuming that charged particles can occupy two separated positions, the so-called two-level systems (TLSs), and thence their energy potential is represented by a double-well potential with two non-trivial minima (see Fig.2.15). The $1/f$ noise then results from the sum of many TLSs with a constant distribution in barrier heights and widths. The TLS

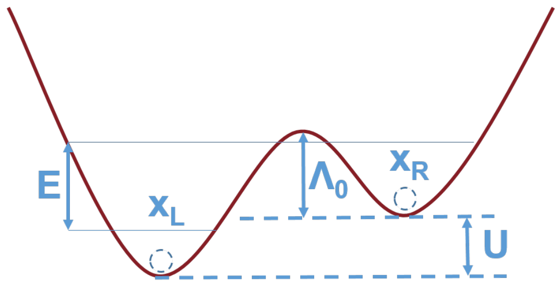

Figure 2.15: Schematic of a double-well potential for a charged TLS. x_L and x_R are the postions at which the particle can be localized, U is the barrier asymmetry and E the excitation energy.

model, first introduced by Phillips[79, 80], contains two main parameters: the potential asymmetry U, which represents the energy difference between the two minima, and the tunnelling strength Λ between the two states. The energy spacing E of a TLS, representing its excitation energy, can be written as:

$$E = \sqrt{U^2 + \Lambda^2}. \tag{2.23}$$

Here, the tunnelling strength Λ is given by:

$$\Lambda = \hbar\Omega(\sigma/\pi)^{1/2}e^{-\sigma}, \tag{2.24}$$

where Ω is the characteristic frequency of the oscillations in an individual well, $\sigma = \left(\frac{2m\Lambda_0}{\hbar^2}\right)^{1/2} l$, m is the particle mass, $l = |x_R - x_L|$ is the separation distance of the two minima and Λ_0 the barrier height. Provided the model, the understanding of the origin of the $S(f) \propto 1/f^\alpha$ behaviour is extremely important from a fundamental physics point of view, but also because of its impact on the application of devices operated at different frequency regimes. The knowledge of the origin can, in fact, help to reduce its effect on the noise properties.

As regards DC-SQUIDs, the origin of $1/f$ magnetic flux noise is not fully understood yet. The fact that the magnitude does not depend on the SQUID area, the superconducting thin film and the substrate used, strongly indicates that $1/f$ flux noise is locally originated. A possible model has been proposed by Koch et al.[81], according to which, electrons can hop on and off from traps, mainly localized above and below the SQUID loop. Each trap locks the electron spin in a specific direction, which randomly varies from trap to trap. Uncorrelated changes of the spins directions result in a series of random telegraph noise (RTN), characterized by a Lorentzian power spectrum, which sum to a total $1/f$ power spectrum. Other models have been proposed, such as: electron spin diffusion[82], magnetic moments locally originated in metal induced gap states[83] and paramagnetic moments from localized electrons resulting in a $\propto 1/T$ temperature dependence of the power spectrum intensity[84]. The latter dependence has been recently observed over a range of frequency around 1 GHz, from the measurement of a tunable gap flux qubit[85]. In the case of HTS SQUIDs, operated at $T = 77$ K, $1/f$ magnetic flux noise has been also associated to thermal activation of vortex motion between different pinning sites. By reducing the device lateral dimensions below $\sqrt{\Phi_0/B}$, where B is the field in which the SQUID is cooled down, this noise source can be eliminated. However, the fact that such $1/f$ behavior is also observed at lower temperatures suggests that a different mechanism is responsible for it.

Another prominent source of $1/f$ noise in DC-SQUIDs has been identified in the critical current noise. This will be discussed in the next section.

Critical current noise

Critical current fluctuations in Josephson junctions are commonly attributed to charge trapping at defects sites in the barrier[86]. The trapped charges prevent tunnelling because of Coulomb repulsion, resulting in an effective reduction of the junction area A_J. Each single charge fluctuator produces random telegraph noise, with a Lorentzian power spectrum and a characteristic relaxation rate $\gamma_r = \tau_u^{-1} + \tau_t^{-1}$, where τ_u and τ_t are the life time of the untrapped and trapped states, respectively. Since charge traps are commonly assumed to be local and non interacting, their distribution produces a sum of Lorentzian features, resulting in a $1/f$ noise power spectrum[87]. Although it is clear that the $1/f$ noise in the critical current of JJ devices results from a superposition of RTN, its origin and specific behaviors, such as $\propto T^2$[88, 89] in contrast to $\propto T$[90] temperature dependencies, are not fully understood yet. A more detailed review of the different observed trends, is reported in ref.[91]. However, the fact that similar TLS densities and noise characteristics are extracted from different experiments and using different materials, has led to the conclusion that these noise sources are independent from the interfaces and are mainly located in the insulating layer[91]. The effect of the critical current fluctuations on the total voltage noise in SQUID applications can be minimized by operating a bias reversal scheme for the SQUID readout[92]. With bias reversal, the working point is periodically varied in a closed loop, including four different combinations of current and flux bias.

2.3.2 Nanowire based nanoSQUID

A possible successful solution to reduce white flux noise in a SQUID consists in the implementation of nanowires in a Dayem bridges configuration instead of JJs, acting as weak links between the superconducting electrodes (see Fig. 2.16 (a)). Depending on the lateral dimensions of the nanowires, their transport properties may differ from a conventional Josephson junction. In particular, the current-phase relation (CPR) changes from the sinusoidal form expressed by Eq. (2.1).

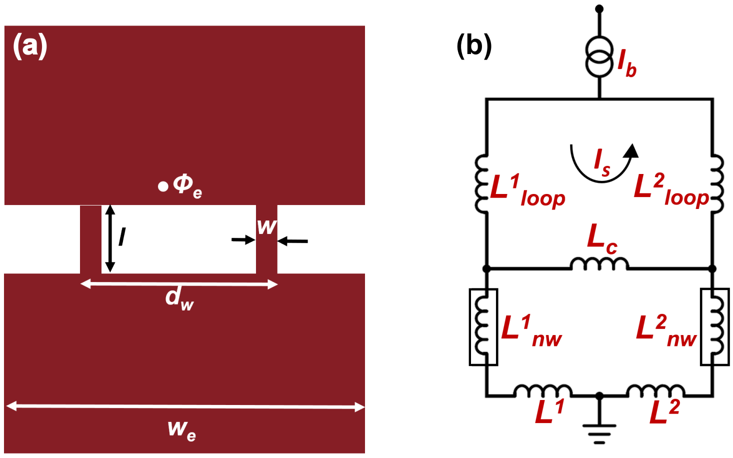

Figure 2.16: (a) Cartoon of a nanowire based nanoSQUID. The SQUID loop is formed by two nanowires of length l and width w, bridging two electrodes whose width is w_e. (b) Schematic circuit network for a nanowire based nanoSQUID inductively coupled to a larger pickup loop. L_c is the coupling inductance. The nanowires are represented by the inductances L^1_{nw} and L^2_{nw}. The pickup loop inductance is given by the sum $L_{pl} = L_c + L^1_{loop} + L^2_{loop}$ and the nanoSQUID loop inductance by the sum $L^1_{nw} + L^2_{nw} + L_c + L^1 + L^2$. I_b and I_s are respectively the bias and the screening current.

In the limit of short and one dimensional (1D) bridges, where "short: $l < \xi$" and "1D: $w, t < \xi$" are defined comparing the lateral dimensions of the wire (length l, width w and thickness t) to the characteristic coherence length ξ of the superconductor, the junction are still characterized by a sinusoidal CPR as derived in ref.[93]. Josephson CPR still holds for short but not 1D bridges ($w \gg \xi$). However, by increasing the wire length above a critical value ($l > 3.46\xi$), the CPR modifies from a single valued expression (typical of Josephson behavior) to a multi valued one (see Fig. 2.17 (a)). In this case, the CPR has been determined by Likharev-Yakobson[93]:

$$J_s^{LY} = \frac{\Phi_0}{2\pi\mu_0\xi\lambda_L^2}\left[(\frac{\xi}{l})\phi - (\frac{\xi}{l})^3\phi^3\right], \tag{2.25}$$

where ϕ represents the phase difference between the two ends of the nanowire. Equation (2.25) results in a critical current density given by:

$$J_d = \frac{\Phi_0}{3\sqrt{3}\pi\mu_0\lambda_L^2\xi}, \tag{2.26}$$

where μ_0 is the magnetic permeability of vacuum. Equation (2.26) corresponds to the Ginzburg-Landau depairing current, at which breaking of the Cooper-pairs takes place, valid for temperatures close to T_c.

Considering the very small value of the coherence length of HTS ($\xi_{ab} \simeq 2$ nm for YBCO, see table 1.1), nanowires realized with these materials are normally characterized by lateral dimension larger than ξ. In particular, for bridges with $w > 4.44\xi$ and $l > 3.49\xi$,

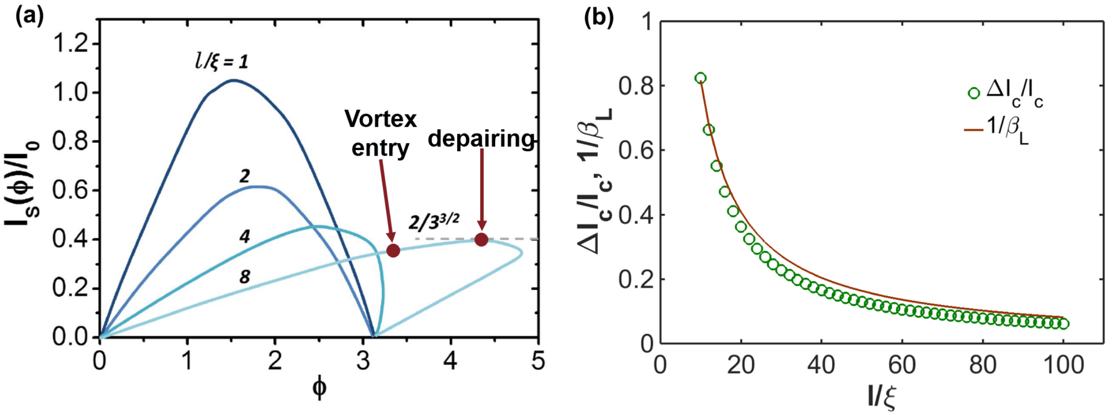

Figure 2.17: (a) Current-phase relation for different values of the l/ξ ratio (adapted from[94]). (b) Critical current relative modulation $\Delta I_c/I_c$ (green open circles) as a function of the wire length l. $1/\beta_L$ is plotted for comparison (red solid line). Both $\Delta I_c/I_c$ and β_L have been calculated following ref.[72, 73].

the transport is affected by coherent motion of Abrikosov vortices[95]. If $t < \lambda$ and $w < \lambda_P$ with $\lambda_P = 2\lambda^2/t$ the Pearl length, the CPR still writes as for the 1D wires (eq.(2.25))[96]. However, in this case the maximum critical current density is determined by the critical phase value ϕ_v at which an Abrikosov vortex overcomes the energy barrier at the edge of the wire $\phi_v = l/2.71\xi \simeq 0.64\phi_d$, and it writes as follows (see ref.[97] for more details):

$$J_v \simeq 0.826 J_d. \tag{2.27}$$

When substituting conventional junctions in a SQUID with nanowires, the proper CPR has to be used in Eq. (2.17), in order to calculate the critical current modulation as function of the externally applied magnetic flux ($I_c(\Phi_e)$). Nevertheless, the methods discussed in section 2.3 can be still used. In particular, for $|\phi| < \phi_v$ the CPR in Eq. (2.26) can be linearly approximated and writes as:

$$I = \frac{\Phi_0}{2\pi L_{kin}}\phi, \tag{2.28}$$

where L_{kin} is the kinetic inductance of the nanowire. The kinetic inductance is a physical parameter that arises from the inertial mass of moving charge carriers. In superconductors it is associated to the motion of Cooper-pairs, and it can be calculated equating their kinetic energy to a correspondent inductive energy. In particular, if one considers a superconducting wire with $wt \ll \lambda_L^2$ (homogeneous current density through the wire), the Cooper-pairs kinetic energy writes as:

$$\frac{1}{2}(2mv^2)(n_s lwt) = \frac{1}{2}L_{kin}I^2, \tag{2.29}$$

where v is the velocity of the Cooper-pairs. Recalling that the current is given by $I = (2en_s v)wt$, L_{kin} can be written as:

$$L_{kin} = \frac{m}{2e^2 n_s}\frac{l}{wt} = \frac{\mu_0\lambda_L^2}{wt}l, \tag{2.30}$$

where in the last step the definition of the London penetration depth has been used (see section 1.2). Because of the large value of λ_L for YBCO (see table (1.1)), the effect of the kinetic inductance could be dominant over the geometric one ($L_{ex} \simeq \mu_0 l$) as it will be discussed in chapter 4. Equation (2.28) indicates that the nanowire acts an inductor, characterized by a supercurrent increasing linearly with the phase difference ϕ between its two ends. From numerical calculations of $I_c(\Phi_e)$ using the CPR (2.25), it can be demonstrated that the relationship $\frac{\Delta I_c}{I_c^{max}} \simeq \frac{1}{\beta_L}$ still holds. Figure 2.17(b) shows the relative modulation depth $\frac{\Delta I_c}{I_c^{max}}$ (green open circles) as a function of the nanowire length, in comparison with $1/\beta_L$ (solid red line). Here $\beta_L = \frac{I_{c,max} L_{nS}}{\Phi_0}$ has been calculated by replacing the SQUID inductance L_{nS} with the nanowires inductance, which is dominated by the kinetic inductance contribution (Eq.(2.30)).

Indeed, for nanowire based nanoSQUIDs[4], the kinetic inductance L_{kin} plays an important role in determining the properties of the device, such as the modulation depth ΔI_c.

Another important parameter determining the performances of a SQUID is its effective area A_{eff}, which represents the portion of the device that contributes to magnetic flux when an external magnetic field B_a is applied. In the next section, the physical mechanisms determining the effective area of a nanoSQUID, and in particular the role of the kinetic inductance, will be discussed.

Effective area of a nanoSQUID

The effective area A_{eff} of a nanoSQUID is generally larger than the geometrical one A_{geo}. This is due to the extra phase gradient in the two electrodes, generated by the screening current I_s induced by the externally applied magnetic field. In the limit $t \leq \lambda_L$, it can be shown that (see Appendix C and section 4):

$$A_{eff} \simeq d_w * w_e, \tag{2.31}$$

where d_w is the separation distance between the two nanowires and w_e the electrode width. In general, a large effective area for a SQUID is desirable, because it results in a higher magnetic field sensitivity (lower field noise), assuming a fixed value of the magnetic flux noise, which is expected to be independent of A_{eff}. It infers clearly from the expression for the magnetic field spectral noise: $S_B^{1/2} = S_\Phi^{1/2}/A_{eff}$. Referring to equation (2.31), in order to get a larger A_{eff} of a nanoSQUID, one could implement wider electrodes and/or increase the distance d_w. However, this would result in a larger total inductance L of the SQUID loop, with a consequent deterioration of the flux noise as it can be deduced from Eq. (2.22). Moreover, wider structures are more prone to vortex trapping, which could have detrimental effects on the noise properties.

Another possible solution is to employe a large pickup loop inductively coupled to the small SQUID loop. The full device can be represented as an equivalent circuit, where the nanowires and the pickup loop act as inductors (see Fig. 2.16(b)). For this representation, the effect of the pickup loop on the A_{eff} can be determined using an interacting loop-current model for superconducting networks in the presence of an externally applied magnetic field and satisfying the fluxoid quantization condition[98]. Following as

[4]This applies also for any other device employing nanowires or nanostripes: e.g. single photon detectors, for which the kinetic inductance is used to detect photons impinging on superconducting stripes.

described in Appendix A, one obtains the following expression for the effective area of the device:

$$A_{eff} = A_{eff}^{nS} + A_{eff}^{pl} \frac{L_c}{L_{pl}}, \tag{2.32}$$

where A_{eff}^{nS} and A_{eff}^{pl} are respectively the effective area of the nanoSQUID loop and of the pickup loop, L_c and $L_{pl} = L_{loop}^1 + L_{loop}^2 + L_c$ are respectively the coupling and the total pickup loop inductance.

2.4 Superconducting Co-Planar Waveguide resonators

Superconducting resonators represent one of the main building blocks for microwave quantum circuits. In this thesis work, they are specifically employed for the investigation of microwave dielectric losses from the materials implemented as substrates for the epitaxial growth of YBCO and cuprates in general. Moreover, they have been used for probing and read-out operation of YBCO Josephson junctions, aiming at the study of decoherence intrinsic to the material itself. The main advantage in using a microwave circuit lies in decoupling the JJs from a shunting admittance that results from e.g. the employment of a DC current biasing circuit. In particular, throughout the whole thesis work, superconducting co-planar waveguide (CPW) resonators have been used. A co-planar waveguide resonator on a dielectric substrate consists of a center conductor stripe separated by a gap from a semi-infinite ground plane. Then, depending on the specific design, different boundary conditions are set by shorting the center conductor to the ground plane or by coupling it to the external environment (see Fig.2.18(a)). This device allows the propagation of standing transversal electromagnetic (TEM) modes. Around its fundamental

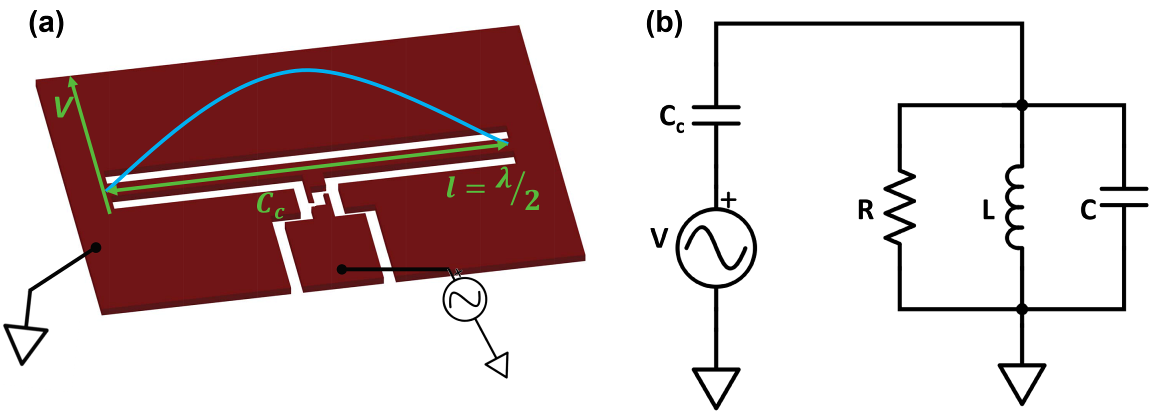

Figure 2.18: (a) Cartoon of an half-wavelength CPW resonator. The voltage of the fundamental mode is sketched. (b) Lumped element RLC circuit modelling the CPW resonator near its fundamental resonance frequency f_0.

resonance frequency f_0, the CPW resonator can be modelled as a single mode lumped element RLC circuit (see Fig.2.18 (b)). The electromagnetic energy can be stored either in the magnetic field related to the L or in the electric field of C. Thus, the energy oscillates between these two elements with a frequency typical of the LC circuit, representing the resonance frequency: $f_0 = 1/2\pi\sqrt{LC}$. In particular, for this thesis work, half-wavelength ($\lambda/2$) CPW resonators have been employed. In this case, the fundamental resonance frequency is given by:

$$f_0 = \lambda^{-1} v_{ph} = \frac{c}{2l\sqrt{\varepsilon_{eff}}}, \tag{2.33}$$

where $v_{ph} = c/\sqrt{\varepsilon_{eff}}$ is the phase velocity, with ε_{eff} the effective dielectric constant. The effective dielectric constant of the device is a number between 1 and the relative dielectric constant of the substrate ε_r (typically $\simeq \varepsilon_r/2$), which depends on the geometrical dimensions of the center conductor, and reflects the fact that not the all electric field lines are inside the dielectric material itself. Here it is important to specify that Eq.(2.33) does not account for the contribution of the kinetic inductance, which is significant in determining the value of f_0 when employing superconductors characterized by a large value of λ_L like YBCO. Details of the resonator modelling are presented in section 3.1. For reflectivity measurements, a $\lambda/2$ resonator is realized with the coupling capacitance C_c at the middle of the center conductor (voltage anti-node), while the two ends are shorted to ground as shown in Fig.2.18 (a).

A CPW resonator is also characterized by the quality factor Q, which is inversely proportional to the damping and defines its bandwidth. The Q factor is defined as follows:

$$Q = \frac{\text{energy stored}}{\text{energy dissipated per radian}}, \tag{2.34}$$

which indicates that resonators with high quality factor have a lower energy dissipation rate compared to the energy stored inside, and therefore the TEM mode in the CPW dies out slowly. Different sources of losses can contribute to determine the Q value of a CPW resonator: coupling to the external environment (experimental setup), radiation, conductor and dielectrics involved in the fabrication. When coupled to the experimental setup, for example via the coupling capacitance C_c, one speaks of loaded quality factor Q_L. The loaded quality factor is given by:

$$Q_L^{-1} = Q_0^{-1} + Q_{ext}^{-1}, \tag{2.35}$$

where Q_0 is the unloaded quality factor, associated to the photons dissipated inside the device and Q_{ext} is the external (or coupling) quality factor, taking into account dissipation of photons to the external environment via C_c. Three different regimes can be distinguished depending on the relative values of Q_0 and Q_{ext}. First, if $Q_0 < Q_{ext}$, the resonator is said to be "undercoupled". Most of the photon energy is lost inside the device. When $Q_0 = Q_{ext}$, the resonator is "critically coupled". The magnitude signal deviates from the Lorentzian shape and drops to zero at the resonance frequency. Finally, if $Q_0 > Q_{ext}$, the resonator is "overcoupled". In this regime most of the photons leak out from the resonator via the coupling capacitor, with a consequent improvement of the signal detection. For this reason, the last regime is desirable for most experiments.

Microwave losses in a superconducting resonator are both temperature and probing power dependent[99, 100, 101, 102]. Losses can be studied from the unloaded quality factor Q_0, which in turn is extracted from the fitting of the reflection or transmission signal of the resonator. Different mechanisms, such as: conductor, dielectric and radiation losses, contribute to establish the value of Q_0:

$$Q_0^{-1} = Q_{cond}^{-1} + Q_{diel}^{-1} + Q_{rad}^{-1}. \tag{2.36}$$

Radiation losses ($1/Q_{rad}$) are geometry dependent and can be minimized by a proper device designing[103]. Dielectric losses ($\tan\delta = 1/Q_{diel}$) are proportional to the sum over all the microwave absorption processes (α_n): $\tan\delta \propto \Sigma_n \alpha_n$. In particular, in the millikelvin temperature range and at low input power, microwave dielectric losses have been associated to resonant absorption due to the presence of a bath of two-level systems (TLSs), which couple via their electric dipole ($\vec{d}$) to the electromagnetic field in the resonator[99, 100, 101, 102]. TLSs, whose energy splitting (ΔE) matches hf_0, are responsible for the resonant absorption mechanism. In this case, the temperature and power dependence for $\tan\delta$ can be derived and writes as[104]:

$$\tan\delta(T,P) = F\alpha_{TLS}\left[1+\left(\frac{P}{P_c}\right)\right]^{-1/2}\tanh\left(\frac{hf_0}{2k_BT}\right) \tag{2.37}$$

where $\alpha_{TLS} = \frac{\pi N d^2}{3\epsilon}$. Here, F is the filling factor, which depends on the geometry and the electric field distribution, N is the constant TLS density of states, $\epsilon = \epsilon_r\epsilon_0$ is the absolute permittivity of the host dielectric material and ϵ_0 the vacuum permittivity. At fixed temperature, $\tan\delta$ saturates for power below the critical value P_c: $\tan\delta(T) = F\alpha_{TLS}\tanh\left(\frac{hf_0}{2k_BT}\right)$ (low power limit, $P \ll P_c$), whereas it decreases as $P^{-1/2}$ by increasing the power above P_c. The critical power is specific for each dielectric material and it can be expressed as follows: $P_c = 3\hbar^2\epsilon/2d^2T_1T_2$, where T_1 and T_2 are, respectively, the relaxation and the dephasing time of the TLSs. The $F\alpha_{TLS}$ product represents the ultimate value of dielectric losses in the low temperature ($k_BT \ll hf_0/2$) and low power limit ($P \ll P_c$).

Since not all the microwave power at input P_{inp} is transferred into the device, it is more appropriate to introduce the circulating power P_{cir} defined as follows[101]:

$$P_{cir} = P_{inp}\left[\frac{Q_0^2 Q_{ext}}{\pi(Q_0+Q_{ext})^2}\right]. \tag{2.38}$$

The circulating power P_{cir} is a measure of the average number of photons in the resonator: $N_{ph} = P_{cir}/hf_0^2$. Moreover, since the microwave field is not uniform over the volume V_f containing the bath of TLS, a numerical calculation of the spatial field distribution over V_f is needed for a proper theoretical treatment. However, it has been proven[101] that experimental data can be reproduced by a modified version of Eq.(2.37):

$$\tan\delta(T,P_{cir}) = F\alpha_{TLS}\left[1+\left(\frac{P_{cir}}{P_c'}\right)^{\beta}\right]^{-1/2}\tanh\left(\frac{hf_0}{2k_BT}\right) \tag{2.39}$$

where β is an extra fitting parameter and P_c' is a geometry dependent critical power. Experimental discrepancies from the expected $\tan\delta \propto P^{-1/2}$ have been modelled in terms of interacting TLSs[105].

Microwave conductor losses ($1/Q_{cond}$) are generally quantified in terms of the surface resistance R_s. In a $s-$wave superconductor the temperature dependence of R_s is described by the *Mattis-Bardeen* theory[106]. The theory predicts an exponential suppression of the conductor losses as the temperature decreases such that, for temperatures below $T \sim \frac{T_c}{10}$ (with T_c the critical temperature), conductor losses are expected to be less dominant compared to other loss mechanisms.

An adequate modelling of conductor losses for high critical temperature superconductors is complicated by the lack of a microscopic theory describing the mechanism leading to superconductivity in these materials. A phenomenological approach, known as two-fluid model, is commonly used instead[107]. The model consists in describing the electron subsystem of a superconductor as a combination of two non-interacting fluids: the superconducting fluid (S-fluid) formed by the charge carriers in the superconducting state and the normal fluid (N-fluid) formed by the charge carriers in the normal state (quasiparticle excitations). A necessary starting point for the model is to postulate a temperature dependence for the densities of the charge carriers in the S- and N-state. The simplest and most used dependencies are expressed as follows:

$$\begin{aligned} n_S(T) &= n_0[1-(T/T_c)]^\gamma, \qquad && \text{for } T \le T_c \\ n_N(T) &= n_0[(T/T_c)]^\gamma, \qquad && \text{for } T \le T_c \end{aligned} \tag{2.40}$$

where n_0 is the total electron density and γ is a power exponent that usually has a value between 1 and 2. With this assumption, following ref. [107], an expression for the surface resistance R_s for thin film ($t \le 2\lambda_L$) at $T < T_c$, can be derived:

$$R_s(T) = (\omega\mu_0)^2 \frac{\lambda_L^4(T)}{t}\sigma_N(T), \qquad \text{for } t \le 2\lambda_L. \tag{2.41}$$

Here, the temperature dependencies for both the normal conductivity $\sigma_N(T)$ and the London penetration depth $\lambda_L(T)$ can be obtained starting from equation (2.40). In general for HTSs, by decreasing the temperature below $T \simeq T_c/10$, one observes a saturation of the surface resistance to values larger than the ones measured for LTSs[108, 109].

2.5 Superconducting artificial two-level system

In order to build an artificial atom (two-level system) based on circuit elements, one can start from the simple LC circuit as sketched in Fig.2.19(a). This circuit includes a linear inductor L_r and a linear capacitor C_r, and can be described by the following classical Hamiltonian:

$$H = \frac{Q^2}{2C_r} + \frac{\Phi^2}{2L} \tag{2.42}$$

where Q is the charge stored on the capacitor and Φ is the flux stored in the inductor. In such a circuit, the energy oscillates between the inductance and the capacitance with a characteristic resonant frequency given by $\omega_r = 1/\sqrt{L_r C_r}$. Using this definition, Eq.2.42 can be rewritten as:

$$H = \frac{Q^2}{2C_r} + \frac{1}{2}C\omega_r^2\Phi^2. \tag{2.43}$$

The latter Hamiltonian has the same form as that of a particle moving in a harmonic potential and characterized by mass m, momentum p_m and position x:

$$H = \frac{p_m^2}{2m} + \frac{1}{2}m\omega_m^2 x^2. \tag{2.44}$$

Following with the analogy, one can quantize the Hamiltonian Eq.2.43 by promoting the classical variables Q and Φ into quantum operators $\hat{Q}$ and $\hat{\Phi}$ (see ref.[110, 18] for

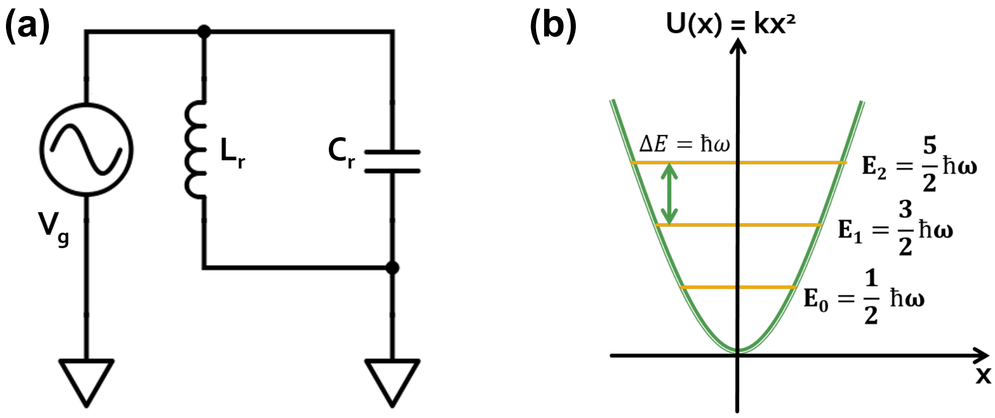

Figure 2.19: (a) Sketch of an LC circuit. (b) Potential energy U as a function of the flux Φ for a quantum harmonic oscillator. The energy level spacing is given by $\Delta E = \hbar w_r$.

formalism). Thence, introducing the creation $a^\dagger$ and the annihilation a operators for the oscillator excitations, defined as:

$$a^\dagger = \sqrt{\frac{C\omega_r}{2\hbar}}\left(\hat{\Phi} - i\frac{\hat{Q}}{C\omega_r}\right) \qquad a = \sqrt{\frac{C\omega_r}{2\hbar}}\left(\hat{\Phi} + i\frac{\hat{Q}}{C\omega_r}\right) \tag{2.45}$$

with the commutator $[a, a^\dagger] = 1$, the quantum Hamiltonian of an LC circuit can be written as follows:

$$H = \hbar\omega_r\left(a^\dagger a + \frac{1}{2}\right). \tag{2.46}$$

A quantum system described by the Hamiltonian in Eq.2.46 is characterized by an harmonic energy spectrum with equally spaced energy levels, as shown in Fig.2.19(b). For this reason, it is not possible to individually address energy transitions, and therefore, such system can not be used as a two-level system. For an artificial atom the anharmonicity of the energy levels spacing is necessary, and can be obtained by adding a nonlinear element to the circuit. For superconducting circuits, a JJ acts as a nonlinear inductor with low dissipation (see section 2.1.1, Eq.(2.5)), and it results in an additional cosine term to the potential energy $U(\phi) = E_J(1 - \cos(\phi))$, where ϕ is the phase difference across the junction. The modified LC circuit and the cosine potential together with the energy levels are shown respectively in Fig.2.20(a) and Fig.2.20(b). The anharmonicity induced by the nonlinearity of the JJ allows to address individual energy transitions and use this circuit as an artificial atom, with the ground and the first excited state forming a qubit. In order to observe the quantum behavior of an atom, an additional condition has to be respected: $k_B T \ll \hbar\omega_{10} \ll \Delta$, where $k_b T$ is the thermal energy of the system, with k_B the Boltzman constant and T the temperature, and Δ is the energy gap of the superconductor.

There are three possible different superconducting Josephson junction qubits: charge[111, 112], flux[113, 114] and phase[8], differing on their relevant degree of freedom. In this thesis, a modification of the charge qubit, the so-called *transmon* design[115], has been used. The basic principles of the transmon are described in the next section.

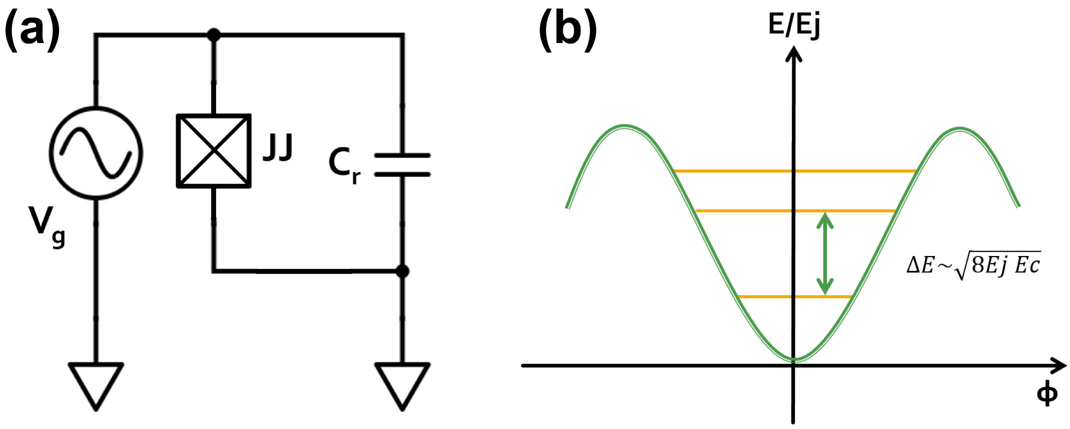

Figure 2.20: (a) Sketch of an anharmonic LC circuit where the linear inductor has been replaced by a Josephson junction, i.e. a non-linear inductor. (b) Potential energy U as a function of the flux Φ for a quantum anharmonic oscillator. The energy level spacing is anharmonic and the 0-1 transition is determined by the Josephson energy E_J and the charging energy E_c .

2.5.1 The transmon qubit

A transmon qubit is an anharmonic LC oscillator made of one or two Josephson junctions (usually in a SQUID configuration) embedded in a CPW resonator. The transmon is a design modification of the Cooper pair box (CPB) qubit, which is operated at a much larger ratio of the Josephson energy E_J and the charging energy $E_c = e^2/2C_\Sigma$, with C_Σ the total transmon capacitance. The E_J/E_c ratio is increased by means of a large shunt capacitance C_B (see Fig.2.21). Such modification leads to a significant improvement of the dephasing times, due to a much lower charge dispersion of the energy levels. The charge dispersion and the anharmonicity of the energy levels represent the two crucial quantities for optimal operation of the transmon, and they both are determined by the ratio E_J/E_c. By increasing this ratio, the charge dispersion reduces, but it also decreases the energy levels anharmonicity. The breakthrough of the transmon is given by the fact that the anharmonicity decreases algebraically with a slow power law in E_J/E_c, whereas the charge dispersion reduces exponentially in E_J/E_c[115]. This implies that operating the transmon at a large E_J/E_c ratio will significantly reduce the dephasing from charge dispersion, with a small loss of anharmonicity.

In figure 2.21 a schematic of the effective circuit diagram of a transmon is sketched. Two Josephson junctions, characterized by capacitance C_J and Josephson energy E_J, are prepared in a DC-SQUID loop configuration, such that $E_J = E_{Jmax}|\cos(\pi\Phi/\Phi_0)|$ can be tuned by means of an external magnetic flux Φ. Here, Φ_0 is the magnetic flux quantum, and $E_{Jmax} = I_c\Phi_0/2\pi$ is the maximum Josephson energy with I_c the critical current of the SQUID. The main modification in comparison to the CPB is the presence of a large shunting capacitance C_B with a similar increase of the gate capacitance C_g. The latter, together with a gate voltage V_g is used to control the offset charge $n_g = V_gC_g/2e + Q_r/2e$ (measured in terms of the Cooper pair charge $2e$) of the device. For a nonlinear oscillator, this offset must be added to the total Hamiltonian; here, Q_r represents an extra offset charge due to external sources different than the gate. Finally, L_r and C_r are used to

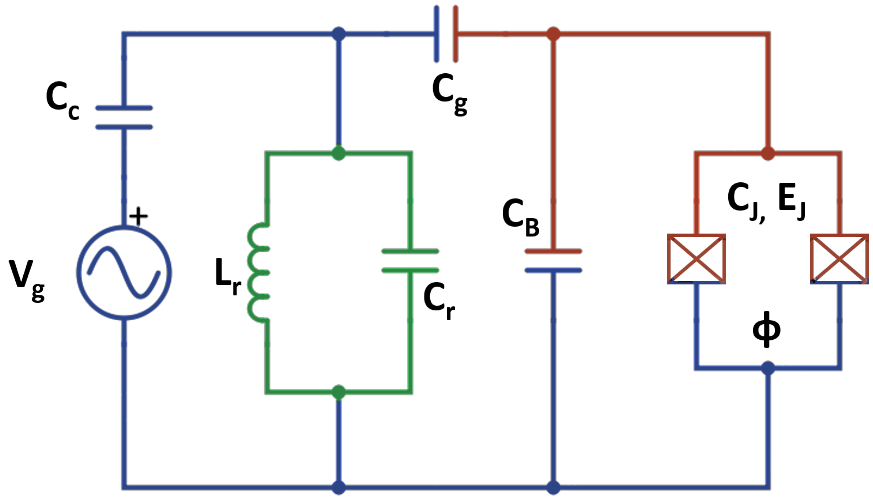

Figure 2.21: Schematic circuit diagram of the transmon qubit (Adapted from ref. [115]). Two Josephson junctions in a SQUID loop, with capacitance C_J and energy E_j, are shunted by a large capacitance C_B, which is matched by a comparable gate capacitance C_g. L_r and C_r represent the CPW resonator. The device is coupled to the external environment via the coupling capacitance C_c.

model the resonator. Thanks to the additional capacitance C_B, the charging energy $E_c = e^2/2C_\Sigma$, with $C_\Sigma = C_J + C_B + C_g$, can be made small and allow for a large E_J/E_c ratio. Following ref.[115], the effective Hamiltonian of a transomn can be reduced to a form identical to the one of a CPB, which in terms of the number operator $\hat{n} = -Q/2e$ for the Cooper pairs and the gauge-invariant JJ phase difference $\hat{\phi}$ writes as:

$$H = 4E_c(\hat{n} - n_g)^2 - E_J \cos\hat{\phi}. \tag{2.47}$$

This Hamiltonian (Eq.2.47) can be solved analytically by means of Mathieu functions[116], and the eigenenergies can be written as follows:

$$E_m(n_g) = E_c a_{2[n_g + k(m,n_g)]}(-E_J/2E_c), \tag{2.48}$$

where $a_\nu(q)$ is the Mathieu's characteristic value, and $k(m, n_g)$ is a integer-valued function that appropriately sorts the eigenvalues[115].

In Figure 2.22 the three lowest eigenenergies E_0, E_1 and E_2, calculated from Eq.2.48, are plotted as a function of the charge offset n_g for four different ratios $E_J/E_c = 1, 5, 10, 50$. From the plots it clearly infers that both anharmonicity and charge dispersion depend on the E_J/E_c ratio: while the charge dispersion of the energy levels decreases with increasing E_J/E_c, the anharmonicity is reduced as well. In order to better visualize the latter point, one can derive the charge dispersion of the mth level, defined as:

$$\epsilon_m \equiv E_m(n_g = 1/2) - E_m(n_g = 0), \tag{2.49}$$

from Eq.2.48, in the limit of large Josephson energy $E_J/E_c \gg 1$. Taking the asymptotic Mathieu characteristic values, it results in an exponential decrease of the charge dispersion

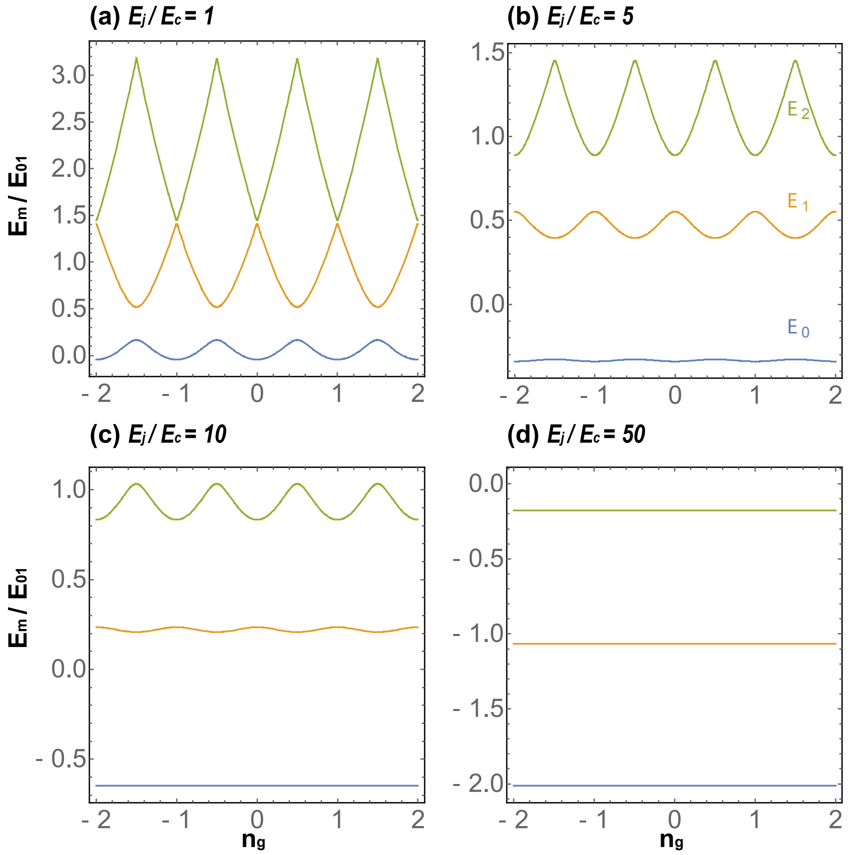

Figure 2.22: First three eigenenergies E_m $(m = 0, 1, 2)$ of the transmon Hamiltonian (Eq.2.47) as a function of the charge offset n_g for different values of the E_J/E_c ratio. E_m are plotted in units of the transition energy E_{01}, evaluated at the degeneracy point $n_g = 1/2$.

with $\sqrt{E_J/E_c}$, as expressed by the following equation:

$$\epsilon_m(n_g) \simeq (-1)^m E_c \frac{2^{4m+5}}{m!} \sqrt{\frac{2}{\pi}} \left(\frac{E_J}{2E_c}\right)^{\frac{m}{2}+\frac{3}{4}} e^{-\sqrt{8E_J/E_c}}. \tag{2.50}$$

The charge dispersion, in units of the energy transition E_{01}, is plotted in Fig.2.23(a) as a function of the E_J/E_c ratio for the first four energy levels (m =0, 1, 2, 3).

The significant reduction of the charge dispersion by increasing the E_J/E_c ratio is associated with a loss of anharmonicity. A sufficient anharmonicity is needed to use the transmon as a qubit, addressing the lowest two of the many energy levels of the system via control pulses. The absolute α and the relative anahrmonicity α_r are defined as:

$$\alpha \equiv E_{m,m+1} - E_{m-1,m}, \qquad \alpha_r \equiv \alpha / E_{m-1,m}, \tag{2.51}$$

where $E_{m,n} = E_m - E_n$ is the energy transition between the m and n levels. Using the perturbation theory in the limit $(E_J/E_c)^{-1} \ll 1$, one can prove that the relative anharmonicity α_r decreases only algebraically with increasing E_J/E_c. In fact, by expanding the cosine term in eq.(2.47) around $\hat{\phi} = 0$ up to the fourth order, the following approximation

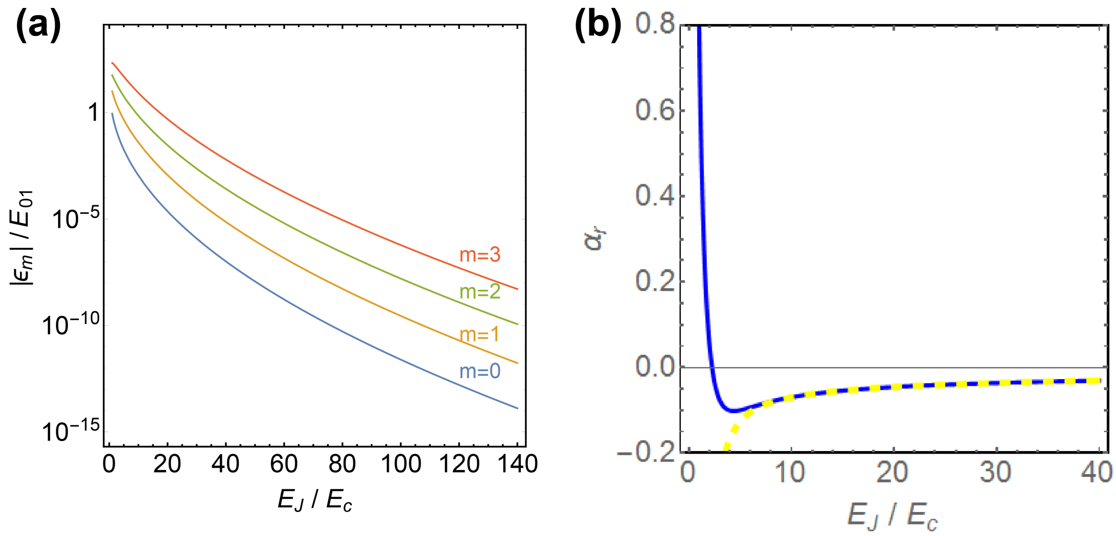

Figure 2.23: (a) Charge dispersion versus the E_J/E_c ratio for the first four energy levels. (b) Relative anharmonicity versus the E_J/E_c ratio (blue solid line). The approximated expression for α_r in Eq.(2.53) is plotted in yellow.

for the eigenenergies is obtained:

$$E_m \simeq -E_J + \sqrt{8E_cE_J}\left(m + \frac{1}{2}\right) - \frac{E_c}{12}(6m^2 + 6m + 3), \tag{2.52}$$

from which, the asymptotic expressions for α and α_r can be written as follows:

$$\alpha \simeq E_c, \qquad \alpha_r \simeq -(8E_J/E_c)^{-1/2}. \tag{2.53}$$

In Figure 2.23(b) the relative anharmonicity obtained from exact solution of Eq.(2.48) is plotted against E_J/E_c, and compared to the approximated expression in Eq.(2.53), showing a good agreement for large E_J/E_c ratios. The exponential gain in charge-noise insensitivity, paid by only an algebraically reduction of the anharmonicity represents the main breakthrough of the transmon design.

2.5.2 Transmon qubit readout operations

To allow for qubit operations, implemented by means of microwave pulses, and readout of the qubit state, the transmon is generally embedded in a superconducting resonator. The resonator also helps to protect the transmon qubit from classical and quantum fluctuations of the external environment. The dynamic of a two-level system with a transition frequency $f_a = \omega_a/2\pi$, coupled to an electromagnetic mode of frequency $f_0 = \omega_0/2\pi$ in the resonator, is described by the well-known Jaynes-Cummings (JC) model. Within this model, the qubit is represented by the Pauli σ_z matrix, whereas the resonator by the creation $a^\dagger$ and annihilation a operators. The full Hamiltonian of the coupled qubit-cavity system writes as:

$$H = -\hbar\omega_a\frac{\sigma_z}{2} + \hbar\omega_0\left(a^\dagger a + \frac{1}{2}\right) + \hbar g_{01}(\sigma_+ + \sigma_-)(a + a^\dagger). \tag{2.54}$$

The third term in Eq.(2.54) is the coupling, of which g_{01} is the strength, and it represents the interaction between the qubit and the resonator. Here σ_+ and σ_- are respectively the raising and lowering qubit operators. Details for the estimation of g_{01} are discussed in section 3.1. The coupling consists of four terms: $a\sigma_+$, $a^\dagger\sigma_-$, $a\sigma_-$ and $a^\dagger\sigma_+$. The first two are nearly energy conserving, moving the excitation between qubit and resonator. The last two, instead, can be neglected in the limit $\Delta_0 = |\omega_a - \omega_0| \ll \omega_a$, the so-called rotating wave approximation (RWA). In this case, the Hamiltonian in eq.(2.54) can be simplified as follows:

$$H = -\hbar\omega_a \frac{\sigma_z}{2} + \hbar\omega_0 \left(a^\dagger a + \frac{1}{2}\right) + \hbar g_{01}(a\sigma_+ + a^\dagger \sigma_-). \tag{2.55}$$

Resonant regime: vacuum Rabi splitting

The Jaynes-Cummings Hamiltonian acts on a Hilbert space spanned by the vector states $|0\rangle\,|n\rangle$ and $|1\rangle\,|n\rangle$, where $|0\rangle$ and $|1\rangle$ are the qubit ground and excited states, and $|n\rangle$ is the photon number state. At zero detuning $\Delta_0 = |\omega_a - \omega_0| = 0$, qubit and resonator are on resonance, and the coupling term lifts the degeneracy between the $|0\rangle\,|n+1\rangle$ and the $|1\rangle\,|n\rangle$ states with an energy splitting of $2\hbar g\sqrt{n+1}$ (vacuum Rabi splitting). The coupled system is then described by eigenstates, given by the superposition of qubit and resonator states, which are known as *dressed states* and write as:

$$|n, \pm\rangle = \frac{|0\rangle\,|n+1\rangle \pm |1\rangle\,|n\rangle}{\sqrt{2}}. \tag{2.56}$$

In this regime, in fact, the energy will be coherently swapped between these two eigenstates with a frequency $\Omega_R = 2g\sqrt{n+1}$, known as Rabi frequency. The dressed states can be experimentally observed via transmission measurements through the qubit-cavity system, from which the coupling strength g_{01} can be determined (see chapter 6).

Dispersive regime

In case of large detuning $\Delta_0 \gg g_{01}$, one speaks of dispersive regime, and the coupling can not induce any transition in the qubit. Nevertheless, a dispersive coupling, leading to a renormalization of the system energies, is still present. In this regime, the JC Hamiltonian can not be solved analytically, and a second order perturbation theory needs to be used. By applying the perturbation theory in terms of g_{01}/Δ, the resulting dispersive Hamiltonian can be written as[115]

$$H_{disp} = \hbar\omega_0 \left(a^\dagger a + \frac{1}{2}\right) + \frac{\hbar}{2}\left(\omega_a + \frac{2g_{01}^2}{\Delta_0} a^\dagger a + \frac{g_{01}^2}{\Delta_0}\right)\sigma_z. \tag{2.57}$$

From the dispersive Hamiltonian (2.57) it can be inferred that the qubit energy splitting depends on the photon number $n = a^\dagger a$, and that ω_a is shifted by an amount $\frac{2g_{01}^2}{\Delta_0}$ per photon number. This effect is known as *AC-Stark shift*. Moreover, the qubit transition frequency ω_a is also shifted by a constant amount $\frac{g_{01}^2}{\Delta_0}$, known as *Lamb shift*. In the dispersive regime also the cavity frequency ω_0 depends on the qubit state, and more specifically it shifts such that: $\omega_0' = \omega_0 \pm \chi\sigma_z$, where the dispersive shift χ is given by:

$$\chi = \chi_{01} - \frac{\chi_{12}}{2} = -\frac{g_{01}^2}{\Delta_0}\left(\frac{E_c}{\Delta_0 - E_c}\right), \tag{2.58}$$

with $\chi_{ij} = \frac{g_{ij}^2}{(\omega_{ij}-\omega_0)}$. This shift in the resonator frequency allows for a dispersive readout of the qubit. Applying a microwave field at frequency close to ω_0, the state of the qubit can be inferred from the measurement of the amplitude or the phase of the transmitted signal through the qubit-resonator system.

2.5.3 Transmon decoherence

For qubit applications in quantum computers, it is fundamental that the qubit retains its quantum information for a time long enough to allow for gate operations[117]. The time over which a qubit maintains a given superposition of states is called *decoherence time* T_2. The main processes contributing to decoherence in a qubit are of two kinds: energy relaxation and dephasing. Energy relaxation processes, due to noise of the environment at the qubit transition frequency, result in a de-excitation (or excitation) of the qubit, and their characteristic time scale is denoted as T_1. Dephasing processes, which are caused by low frequency noise i.e. fluctuations of the environment at frequencies $\ll \omega_a$, instead, are responsible for a random change in the phase of the quantum state, and the characteristic time scale is denoted as T_ϕ. The total decoherence time T_2 is a linear combination of both types of processes characteristic times and writes as:

$$\frac{1}{T_2} = \frac{1}{2T_1} + \frac{1}{T_\phi}. \tag{2.59}$$

In this thesis work, the measurement of decoherence time of an all YBCO transmon qubit is used to investigate intrinsic properties of the material itself, which can be directly related to physical mechanisms describing the superconducting state. As extensively discussed in the previous section (2.5.1), the transmon qubit is characterized by a very low sensitivity to charge noise. This represents the main benefit in using a transmon as compared to other superconducting qubits. However, other noise channels contribute to decoherence in a transmon qubit. In this section the effect of various noise sources on the transmon relaxation T_1 and dephasing T_ϕ times are presented in details, with particular attention to those sources that are expected to be prominent when using HTS cuprates.

Relaxation by spontaneous emission

The coupling of the transmon with the electromagnetic mode in the resonator, via dipole interaction, induces relaxation by spontaneous emission. The resulting T_1 time can be estimated by considering the average power P emitted into free space by a electric dipole d, oscillating at angular frequency ω, and it writes as[115]:

$$T_1^{rad} = \hbar\omega_{01}/P = \frac{12\pi\epsilon_0\hbar c^3}{d^2\omega_{01}^3}. \tag{2.60}$$

In order to get T_1^{rad}, a numerical estimate for the dipole moment d is needed. It can be obtained as $d = 2eL$, where L is the distance over which a Cooper pair travels when tunnelling between the two superconducting electrodes forming a Josephson junction.

Purcell effect

The decay rate of a system placed in a resonator is altered as a result of the Purcell effect[118]. In particular, the spontaneous relaxation rate of each transmon level acquires an extra Purcell contribution γ_κ, which for the first excited state is given by:

$$\gamma_\kappa^{(01)} = \kappa \frac{g_{01}^2}{\Delta_0^2}, \tag{2.61}$$

where κ is the resonator decay rate.

Dielectric losses

Intrinsic dielectric losses $\tan\delta$ from the insulating materials, involved in the fabrication of superconducting qubits (see section 2.4), represent one of the main sources of relaxation for these devices. In particular, the dielectric losses affect the electric field interacting with the qubit, and the resulting relaxation rate is proportional to $\tan\delta$:

$$\Gamma_1 = 1/T_1 \propto \tan\delta. \tag{2.62}$$

Therefore, a proper choice of the dielectric materials to employ for the realization of HTS transmon qubits is crucial, as discussed in section 2.4 and chapter 5.

Relaxation and dephasing due to quasiparticle tunnelling

Both relaxation and dephasing in superconducting qubits are affected by the presence of quasiparticles in the system. More specifically, the relaxation rate $\Gamma_1 = 1/T_1$ is directly proportional to the quasipraticles tunnelling rate Γ_{qp} and the number of quasiparticles N_{qp}[115]. It can been shown that in LTS transmon qubits, below 100 mK, the relaxation due to quasiparticles is not significant, as a direct consequence of a very low N_{qp} in the limit $T \to 0$. Moreover, differently from a charge qubit, adding or removing a quasiparticle does not influence the transition frequency of a transmon qubit because of the exponentially flat charge dispersion (see section 2.5.1), and hence it does not affect the dephasing.

The situation is completely different for an HTS transmon qubit. Due to the $d-$wave symmetry of the superconducting order parameter, in fact, the system is characterized by the presence of nodal quasiparticles (along the nodal direction). In addition to that, for some specific interface angles α of a SIS junction involving $d-$wave superconductors, the quasiparticles conductance is enhanced by the presence of the midgap states (see section 2.2 for more details). In this case, the decoherence time T_2 has been estimated to be in the $5 - 150$ ns range[119], depending on the junction parameters. More details are discussed in the next section.

Decoherence due to MGS

The quasiparticle conductance in $d-$wave superconductors SIS junctions is enhanced by the presence of midgap states (see section 2.2). Therefore, MGS can contribute significantly to the quantum decoherence of a $d-$wave superconducting qubit. In ref. [119] the phase dependent quasiparticles conductance $G(\phi)$ is calculated for a an asymmetric $d_{0,\frac{\pi}{4}}$ junction, i.e. with order parameters in the superconducting electrodes are such that

$\alpha_L = 0$ and $\alpha_R = \frac{\pi}{4}$, where $\alpha_{L,R}$ represents the orientation angle of the order parameter in respect to the surface normal direction, respectively for the left and right superconductor (see Fig.2.10). $G(\phi)$ is calculated assuming a non-linear coupling to an Ohmic heat bath, and the decoherence rate is then proportional to the bath spectrum taken at resonance with the qubit. One of the main results is that the quasiparticle conductance of a GB JJ depends strongly on the phase difference across the junction. Moreover the conductance peaks at $\phi = 0, \pi$ become much less significant at low temperatures. Using experimental critical current values in the 5-100 nA range, typical of the YBCO GB junctions used in this thesis work (see section 6), a decoherence time in the range $T_2 \simeq 150 - 5$ ns is estimated at $T = 0.05T_c$ (lower I_c correspond to a larger T_2). An important point is that G, and thence T_2, depend on the value of the imaginary part of the quasiparticles energy η, which is associated to impurity and roughness scattering processes. A larger η results in a larger G. The increase of G is attributed to a broadening of the MGS with η, enhancing their overlapping around the Fermi energy. However, the presence of a subdominant order parameter, opening a gap also in the nodal directions, would result in significant reduction of the quasiparticle conductance G and a consequent improvement of the overall transmon coherence time.

Dephasing due to critical current noise

Qubit dephasing is associated to fluctuations of the transition frequency due to the coupling to an external environment. In the case of a transmon qubit, the main source of dephasing are critical current fluctuations, which directly influence the Josephson energy E_J. The critical current fluctuations δI_c are commonly associated to bistable charge trapping states in the junction barrier, resulting in an overall $1/f$ critical current noise power spectral density (see section 2.3.1). Trapping and detrapping of charges causes a modification of the tunnel barrier, with a consequent change in the critical current and hence in E_J. The resulting dephasing time can be written as follows[115]:

$$T_\phi \simeq \frac{\hbar}{A} \left| \frac{\partial E_{01}}{\partial I_c} \right|^{-1} = \frac{2\hbar I_c}{A E_{01}}, \tag{2.63}$$

where A is the square root of the amplitude of the $1/f$ critical current noise power spectral density. While the amplitude A is $10^{-6} I_c$ in typical LTS tunnel junctions[86], biepitaxial grain boundary HTS junctions, with similar junction areas A_J as those employed in this thesis work, are characterized by critical current fluctuations with an amplitude $A_{GB} \simeq 10^{-4} - 10^{-3} I_c$[120]. Therefore the resulting dephasing time for a YBCO transmon qubit is expected to be about $2-3$ orders of magnitude shorter compared to an LTS one.

Chapter 3

Modelling, fabrication and experimental techniques

In this chapter the main steps towards the realization and the experimental investigation of the presented devices are discussed. First, the modelling leading to the actual design of the devices is presented. In particular, the section is focused on the designing of the CPW resonators taking into account the different substrates involved, and on the proper modelling of both the resonators coupling C_c and the transmon total C_Σ capacitance. Then, the fabrication methods, with a particular attention on the realization of the YBCO grain boundary junctions, are discussed in details. Finally, the experimental setups used for the microwave reflection and transmission measurements, and for the noise characterization of the nanoSQUIDs are described.

3.1 Devices modelling

In this section, the modelling of the devices realized for this thesis work, made prior to their design, is discussed. In particular, first the method used for the estimation of the main physical parameters of the CPW resonators is introduced, then the evaluation of the transmon characteristic energies E_J and E_c (see section 2.5.1) is shortly described.

CPW resonator

The first requirement to be fulfilled when designing a CPW resonator is the matching of its total characteristic impedance Z to the one of the experimental environment: $Z \approx Z_0 \approx 50\,\Omega$. Since the characteristic impedance is given by: $Z = \sqrt{\frac{L'}{C'}}$, where L' and C' are respectively the total inductance and capacitance per unit length of the CPW, a numerical evaluation of L' and C' is needed. One could follow two different approaches: a full electromagnetic simulation[121] via computational tools like MW Office or use approximated analytic expressions obtained using the conformal mapping method[122]. This last method provides estimations for L' and C' with a reasonably good accuracy for frequencies up to 20 GHz[123]. The approximated expression for L' and C' are written in terms of the complete elliptic integrals whose modulus are given by the relative ratios of the geometrical dimensions of the device, including the thickness of the dielectric materials involved (see Fig.3.1 (a)). When dealing with superconducting materials characterized by a large value of the London penetration depth λ_L like YBCO ($\lambda_L \simeq 150 - 300$ nm for thin films[124]), the kinetic inductance of the center conductor L'_{kin} needs to be taken into account (see table 3.1). For this reason, a modelling of L'_{kin} is also required, and for this thesis work the method reported in ref. [108] has been followed. There, an analytic expression for the kinetic inductance is obtained in a static field approximation and comparing it to the results of a partial wave analysis[108]. As highlighted in Fig.3.1 (a), the

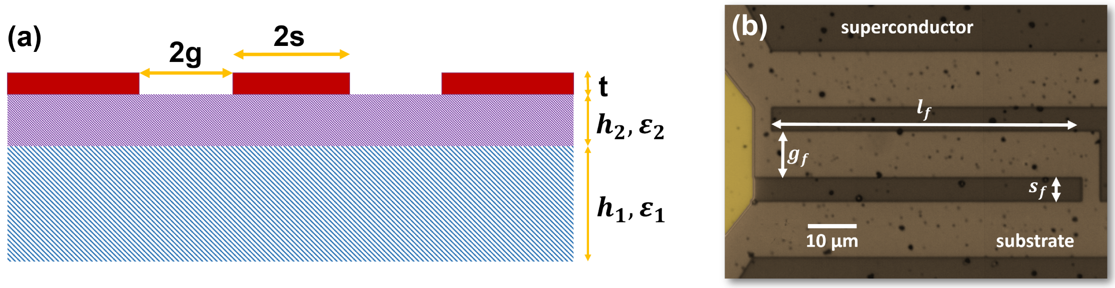

Figure 3.1: (a) Schematic representation of a CPW resonator used for the conformal mapping method. h_1, ε_1 (h_2, ε_2) are respectively the thickness and the relative dielectric permittivity of the first (second) dielectric layer; t is the thickness of the conductor, $2s$ and $2g$ are respectively the width of the center conductor and the gap, i.e. the distance between the center conductor and the ground plane. (b) Optical image of the finger coupling capacitance used for the YBCO CPW resonator employed in the transomon qubit device. The dimensions for the capacitance modelling are labeled: l_f is the overlapping finger length, g_f is the gap between two adjacent fingers and s_f is the fingers width.

physical parameters describing a CPW resonators depend also on the type of the dielectric materials employed, more specifically on the resulting effective dielectric permittivity ε_{eff}. For this reason a proper prior modelling is necessary every time the substrate is changed or a combination of two different dielectrics is used instead (like for the YBCO transmon, see section 3.2). From the estimation of ε_{eff}, the fundamental resonance frequency can also be evaluated using Eq.(2.33) if the kinetic inductance contribution is negligible. To enable for its probing, the resonator is commonly capacitively coupled to the external environment. Therefore another important parameter, whose design needs to be simulated, is the coupling capacitance C_c. The coupling capacitance is directly related to the external quality factor Q_{ext} as expressed by:

$$Q_{ext} \approx \frac{(C_R + C_c)}{(\omega_0 Z_R C_c^2)}. \tag{3.1}$$

Equation (3.1) is obtained by modelling the CPW resonator, around its fundamental frequency f_0, as a single mode RLC lumped element circuit, with L_R, C_R and $Z_R = \sqrt{\frac{L_R}{C_R}}$ representing the equivalent inductance, capacitance and impedance, respectively. The values of L_R and C_R can be obtained from L' and C', taking into account the specific CPW resonator geometry. In the case of a $\lambda/2$ resonator, they write respectively as: $L_R = L'\frac{4l}{\pi^2}$ and $C_R = C'\frac{l}{4}$, where l is the total resonator length. Depending on the resonator regime that one requires (under-, critically- or over-coupled), different C_c designs can be chosen.

From the lumped element circuit modelling a more accurate estimate of the fundamental resonance frequency f_0 is given by:

$$f_0 = \sqrt{\frac{1}{[2\pi(L_R + L_{kin})(C_R + C_c)]}}. \tag{3.2}$$

In fact, differently from Eq.(2.33), equation (3.2) accounts also for the kinetic inductance contribution and the coupling capacitance. For the devices reported in this thesis and in the appended papers, a finger capacitance design has been used (see Fig.3.1 (b)). Again, the value of the resulting capacitance can be evaluated, starting from its geometry, using both full electromagnetic simulation and approximated analytic expression obtained with the conformal mapping method. The optimized geometrical dimensions of the CPW resonators are the following: $2s = 20\,\mu$m, $2g = 12\,\mu$m, $t = 200$ nm and $t = 120$ nm respectively for the Nb and the YBCO devices. In table 3.1, the resonators parameters for such geometry, obtained via the conformal mapping method for the different substrates employed, are listed. Here, the prime sign indicates that the values are per unit

Substrate	ε_{eff}	$C^{'}$(F/m)	$L^{'}$(H/m)	$L^{'}_{kin}$(H/m)	C_c(fF)	$Z(\Omega)$	f_0(GHz)
MgO ($\varepsilon_r \simeq 9$)	5	0.13 n	0.44 μ	6.3 n	4	75	5.1
LAO ($\varepsilon_r \simeq 25$)	13	0.33 n	0.44 μ	6.3 n	4	47	4.8
LSAT ($\varepsilon_r \simeq 23$)	11.5	0.29 n	0.44 μ	6.3 n	4	49	5
sapphire ($\varepsilon_r \simeq 11$)	6	0.15 n	0.44 μ	6.3 n	4	68	4.7
LSAT/CeO_2	12	0.3 n	0.44 μ	6.3 n/46 n*	5.2	50	4.9

Table 3.1: CPW resonators parameters obtained from conformal mapping for different substrates. *This value is obtained using $\lambda_L = 150$ nm and $t = 120$ nm proper of the YBCO resonator. All th other values for $L^{'}_{kin}$ are for the Nb resonators using $\lambda_L = 90$ nm.

length. The length l has been chosen such that f_0 is close to 5 GHz, appropriate value for the experimental setup utilized (see section 3.3). The fundamental resonance frequency is evaluated using eq.(3.2), which for the YBCO case provides a more accurate estimation because it also accounts for the kinetic inductance. Since the dielectric losses due to resonant absorption from a bath of TLSs are geometry dependent (see section 2.4), the resonators have been patterned with identical geometry in order to make a proper comparison between the different substrates. For this reason, while the dimensions are optimal for resonators patterned on LAO, LSAT and LSAT/CeO_2, in the case of MgO and sapphire the characteristic impedance Z does not perfectly match the $50\,\Omega$ of the experimental setup (see table 3.1). This has resulted in a non perfectly symmetric line shape of the resonance dip. However, taking into account the asymmetry in the fitting procedure (see ref.[125] for details), it is still possible to extract the unloaded quality factor Q_0 with a good accuracy.

Transmon qubit

As already extensively discussed in section 2.5.1, the two energy scales characterizing the transmon qubit design are the Josephson E_J and the charging energy E_c. They, in fact, determine the transmon transition frequency $hf_{0\to 1} = \sqrt{8E_JE_c} - E_c$, and the ratio $k = E_J/E_c$ regulates the balance between anharmonicity and charge dispersion (see section 2.5.1). When designing a transmon, one needs to estimate the optimal E_J and E_c values for the required frequency $f_{0\to1}$ and ratio k.

The Josephson energy depends on the value of the critical current I_c of the Josephson junction (or of the two JJ in SQUID configuration) used for the device, and can be tuned by external magnetic flux. In fact, recalling Eq.(2.6), E_J in case of a DC-SQUID writes as:

$$E_J = E_{Jmax} \left| \cos\left(\frac{\pi\Phi_e}{\Phi_0}\right) \right|, \tag{3.3}$$

where $E_{Jmax} = I_c\Phi_0/2\pi$ is its maximum value. The charging energy $E_c = e^2/2C_\Sigma$, instead, depends on the total transmon capacitance C_Σ. Indeed, with the choice of a frequency close to 5 GHz and a ratio $k \approx 100$, an $I_c \approx 30$ nA and a $C_\Sigma \simeq 75$ fF are needed. A prior and precise estimation for E_J when bi-epitaxial GB YBCO Josephson junctions are employed is not straightforward. In fact, while high quality nanometer sized YBCO junctions carrying critical current in the nA range can be realized[126, 127], the actual I_c value is difficult to predict with a good accuracy. Moreover, since HTS junctions in a SQUID configuration are normally asymmetric ($I_{c1} \neq I_{c2}$), one can not rely much on the tuning by external magnetic field for tuning E_J to the needed value. On the other hand, E_c can be modelled with much better accuracy by means of the full capacitance network sketched in Fig. 3.2 (b). Using the network, the total transmon capacitance

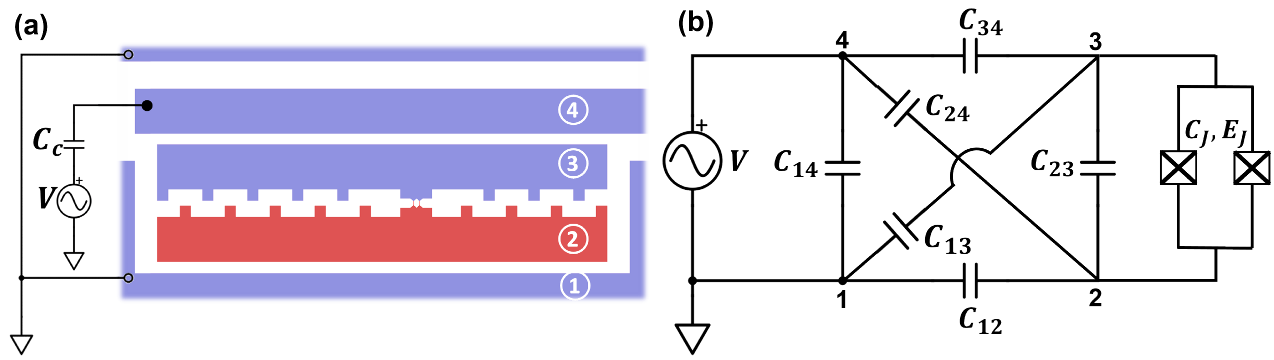

Figure 3.2: (a) Cartoon of the transmon design used for the devices presented in the thesis. The different parts are enumerated (b) Schematic of the full capacitance network circuit associated to the transmon device.

$C_\Sigma = C_J + C_B + C_g$ can be evaluated. In fact, the additional capacitance is $C_B = C_{23}$, whereas the gate capacitance C_g is given by:

$$C_g = \frac{C_{12}C_{34} - C_{13}C_{24}}{(C_{12} + C_{34} + C_{13} + C_{24})}; \tag{3.4}$$

finally, the Josephson capacitance C_J for nano-junctions can be neglected. For the geometry chosen for this thesis work, sketched in Fig. 3.2 (a), C_Σ has been simulated using the electrostatic environment[1] of Comsol Multiphysics. The following values have been

[1] Although not accurate as a full electromagnetic simulation, this method provides estimations with a maximum 20% error.

obtained: $C_g \approx 8$ fF, $C_{23} \approx 49$ fF, and thence $C_\Sigma \approx 57$ fF. From the values of the capacitances, the coupling energy expressed by:

$$\hbar g_{ij} = 2\beta e V^0_{rms} < i|\hat{n}|j > . \tag{3.5}$$

can be calculated. Here $\beta = C_g/C_\Sigma$, $V^0_{rms} = \sqrt{\frac{\hbar\omega_r}{2C_r}}$ is the rms voltage of the vacuum fluctuations of the resonator, and $< i|\hat{n}|j > \approx \sqrt{\frac{j+1}{2}} \left(\frac{E_J}{8E_c}\right)^{1/4}$ is the matrix element of the number operator $\hat{n}$. Using the values aforementioned, a value of $g_{01} \approx 200$ MHz is obtained.

3.2 YBCO nano-patterning

The patterning of the YBCO at the micro and nanoscale is a challenging task. This is mostly due to its high chemical instability and oxygen out-diffusion. Moreover because of the short coherence length ξ, the YBCO is very sensitive to defects and disorder. Different approaches have been explored during the last decades, such as: focused ion beam (FIB) milling[128, 129], contact mode atomic force microscopy (AFM)[130], porous hard templates[131] and e-beam lithography[132, 133], to fabricate YBCO nanostructures.

In our group a reliable nano-fabrication technique, which allows to get grain boundary junctions at the nanoscale and YBCO nanowires, has been developed[134]. In short, the patterning of the YBCO at nanoscale is done via a gentle Ar^+ milling etching through an e-beam defined carbon mask. A crucial point is the coverage of the YBCO film with a gold capping film, which acts as protective layer for the YBCO during the fabrication steps involving the use of chemicals and resist. Moreover, the Au capping also helps to avoid overheating of the YBCO during the Ar^+ milling and the consequent oxygen loss.[2] Such fabrication technology allows for the realization of YBCO nanowires characterized by electrical transport properties close to those of the pristine bulk material. The measurement of large values of the critical current density, approaching the depairing limit[135], in nanowires realized with this technique, has served to prove the high uniformity of their superconducting properties. These structures represent ideal candidates for the investigation of basic physical properties of cuprates [136].

3.2.1 Bi-epitaxial grain boundary HTS junctions

In this thesis, nanometer sized bi-epitaxial grain boundary YBCO junctions have been fabricated, investigated and implemented for engeneering an all HTS transmon qubit. The bi-epitaxial technique, first introduced by Char et al.[63], makes use of a seed layer to change the epitaxial relations of the YBCO thin films with the substrate(see section 2.1.3). In particular for the junctions presented here, an $(110)La_{0.3}Sr_{0.7}Al_{0.65}Ta_{0.35}O_3$ (LSAT) substrate in combination with a CeO_2 seed layer is used. LSAT is an ideal substrate for applications in microwave devices working at millikelvin temperatures and at low input power regime (see chapter 5 for details). Moreover, high quality submicron YBCO JJs patterned on such dielectric have been recently reported[127].

[2]For devices like resonators and transmon, the final gold removal is necessary to avoid microwave dissipation due to the normal conductor layer.

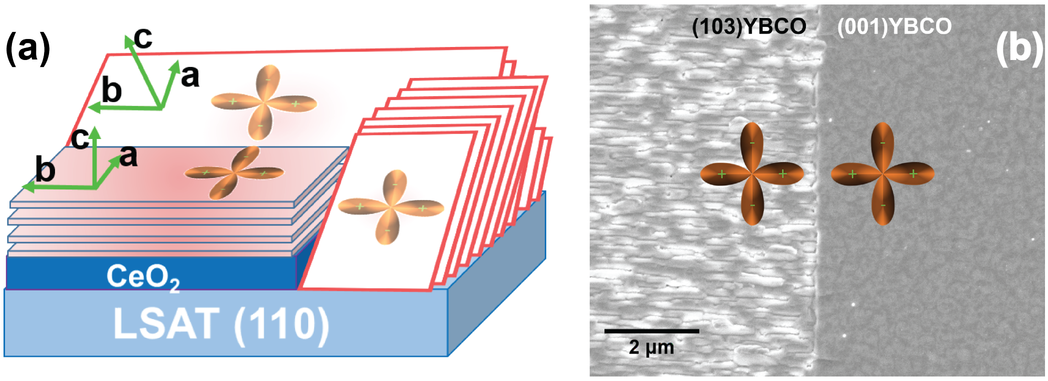

Figure 3.3: (a) Cartoon of a bi-epitaxial YBCO junction, obtained combining (110)LSAT substrate with a patterned CeO_2 thin film acting as template layer. A possible configuration of the CuO_2 planes is depicted. (b) SEM image of a YBCO film deposited on a CeO_2 layer patterned on top of an LSAT substrate. The image shows the morphology characterizing the two different YBCO epitaxial growths. A grain boundary forms at the interface between the two different crystal orientations.

The YBCO, deposited at high temperatures by pulsed laser deposition (PLD) technique, grows preferably (103)-oriented on the bare (110)LSAT substrate (see Fig.3.3(a)). Specifically, the LSAT substrates used here are characterized by a 3.5 degree vicinal cut, in order to avoid a mixture of (103) and (-103) YBCO grains equally probable on exact substrate. Details on the growth mechanisms can be found in ref. [137]. On top of the CeO_2 seed layer, instead, the YBCO grows c-axis (001) oriented (see Fig.3.3(a)). Therefore by a proper patterning of the CeO_2 seed layer, a grain boundary forms at the interface between the c-axis and the (103)-oriented YBCO. The SEM image in Fig.3.3(b) shows a typical bi-epitaxial grain boundary: on the left, the (103)YBCO growth characterized by elongated grains due to the different YBCO growth velocity in the two in-plane directions; on the right, the (001) growth characterized by a rather uniform film. The final typology of grain boundary also depends on the in-plane rotation around the c-axis YBCO on CeO_2. In-plane rotation can be checked by $\phi-$scan x-ray diffraction (XRD) measurements. Since randomly in-plane rotated c-axis grains would cause a degradation of the microwave performances of the YBCO (large surface resistance R_s value), an epitaxial YBCO is required for the realization of a transmon qubit. An XRD characterization of c-axis YBCO films used in this thesis is presented in figure 3.4. The $2\theta - \omega$ scan (Fig. 3.4(a)) shows that the film is fully (001) oriented, whereas the ϕ scan (Fig. (b)) shows only four peaks at 90° from each other, which demonstrates a complete in plane epitaxy. The fabrication technology previously introduced can be used to realize nanometer sized junctions. In figure 3.5 a schematic cartoon of the main fabrication steps, used to define such junctions, is shown. In the following a detailed description of each step is listed (see Appendix B for details of the fabrication recipes utilized):

1. a 40 nm thick CeO_2 film (seed layer) is first deposited by magnetron sputtering and then patterned via optical lithography and Ar^+ milling.

2. A 100-140 nm thick YBCO film is deposited by PLD; the YBCO grows (103) oriented on the bare LSAT substrate and c-axis on the CeO_2. To avoid chemical

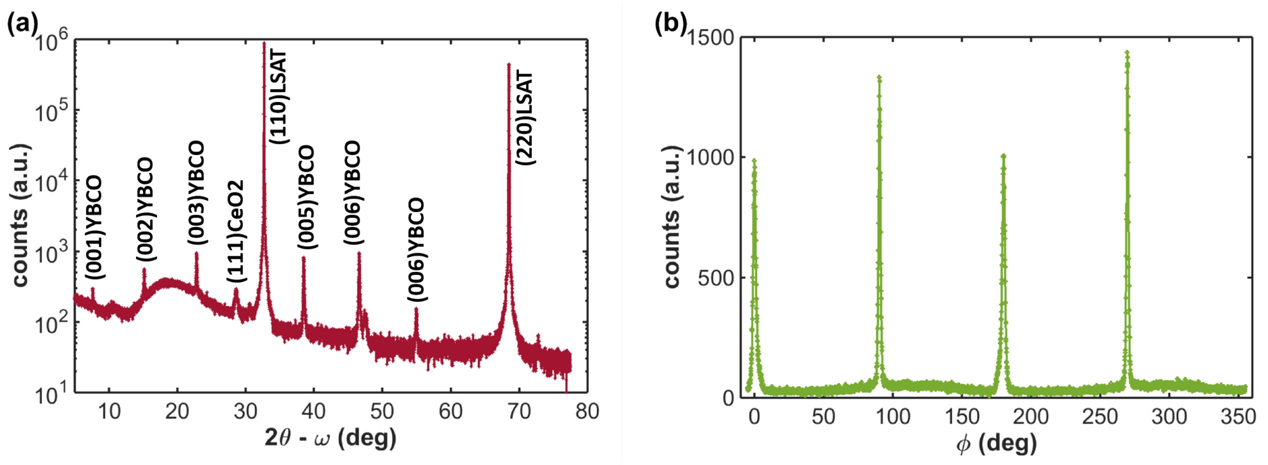

Figure 3.4: (a) $2\theta - \omega$ scan of a 100 nm thick YBCO film deposited on (110) LSAT covered by 40 nm thick CeO_2 film. The (00n) peaks of the YBCO, together with the peaks of both CeO_2 and LSAT, are labeled. (b) XRD ϕ scan of the same YBCO film. The presence of only four peaks indicates that there are no in-plane rotations.

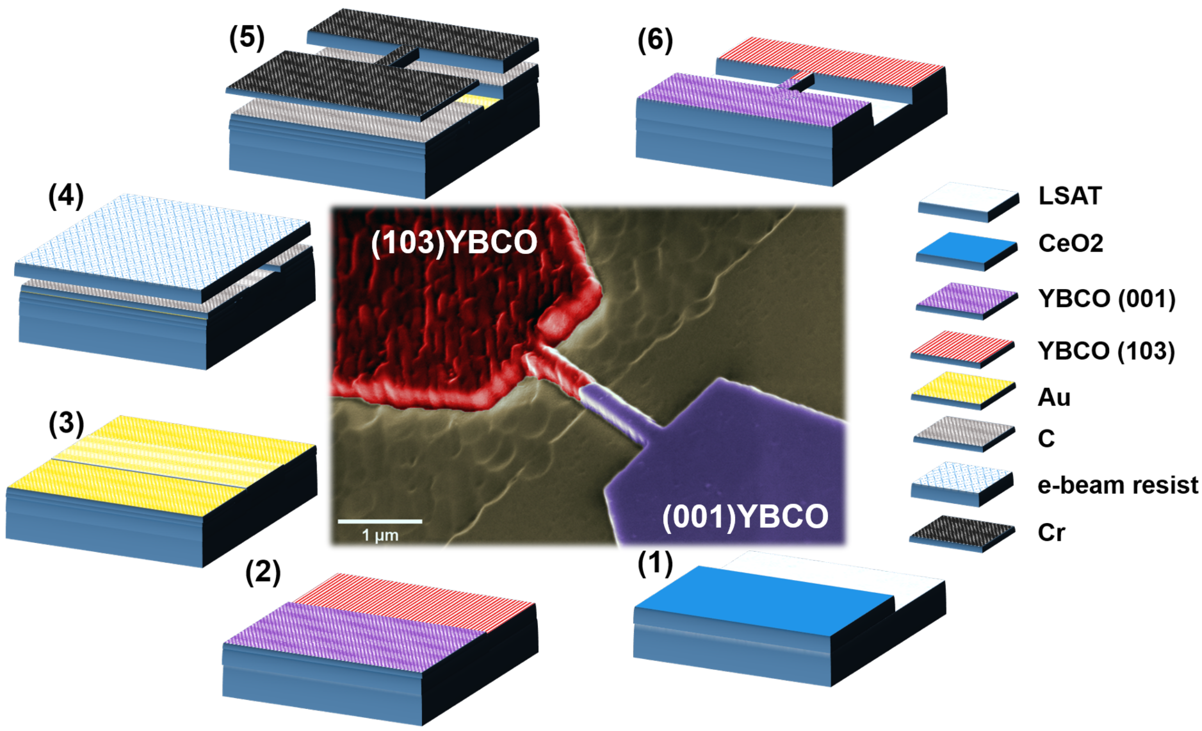

Figure 3.5: Schematic of the fabrication process for a bi-epitaxial YBCO Josephson junction. A simplified, not in scale, cartoon of the main steps is shown together with a legend of the different materials involved in the process. An SEM image (false color) of a finalized junction is also shown.

reactions between the CeO_2 and the YBCO possibly induced by the high deposition temperature, a template technique is used. First a 20 nm thick YBCO film is deposited at $T = 770\,^{\circ}$C, and then the remaining film is deposited at $T = 810\,^{\circ}$C. The presence of the YBCO template layer prevents any chemical reaction when the temperature is raised to the optimal value.

3. The YBCO film is covered by a 100 nm thick gold layer, deposited by magnetron sputtering. Markers, for the alignment of the submicron junctions are patterned in the gold film by optical lithography and Ar^+ etching. The gold layer is then partially etched. The 40 nm Au layer left on the YBCO acts as protective layer for the YBCO during the rest of the fabrication process.

4. The sample is covered by a 70 nm thick amorphous carbon film, which acts as a hard mask during the Ar^+ milling procedure to define the submicron junctions.

5. After e-beam exposure and resist development, a 12 nm thick chromium film is deposited by e-beam evaporation. After a lift-off procedure a Cr mask is defined on top of the Carbon. This is then transferred to the Carbon by O_2 plasma.

6. A gentle Ar^+ milling, with an acceleration voltage slightly above the etching threshold for YBCO, is used to define the desired structures. Then the remaining carbon layer is removed again by O_2 plasma etching. Finally, the gold capping layer is etched away by Ar^+ milling or O_2 plasma etching.

Following these steps, 200-300 nm wide bi-epitaxial YBCO junctions have been fabricated and employed for the realization of an all YBCO transmon qubit.

3.3 Experimental setups

The measurement of superconducting quantum devices requires, first of all, that the latter are cooled down to temperatures below the critical temperature T_c of the superconducting material involved. In the case of the YBCO thin films ($T_c \approx 90$ K), the use of liquid nitrogen should be sufficient. However, depending on the particular kind of measurement technique and on the specific physical properties to study, lower temperatures are desirable. For this reason, an ^{3}He cryostat with a base temperature of ≈ 300 mK has been used for the electrical transport and noise characterization of the YBCO nanowire based nanoSQUIDs. Whereas a ^{3}He/^{4}He dilution (dry) refrigerator has been employed for the reflection and the transmission measurements of the bare Nb/YBCO CPW resonators and of the YBCO transmon qubit, respectively.

In the following a description of the actual experimental setups, specifically used for this thesis work, is presented.

Microwave measurements

Although the YBCO T_c is larger than the liquid nitrogen boiling temperature (77 K), a transmon qubit is commonly operated in the single photon limit, which necessitates much lower temperatures. In fact, typical experiments involving transmon devices are designed to work in the frequency range 4-8 GHz for $f_{0\to1} = |E_0 - E_1|/h$ (transition frequency from the ground to the first excited state), which requires temperatures in the millikelvin range (5 GHz≅250 mK). Indeed, working at the base temperature of a ^{3}He/^{4}He dilution refrigerator ($T \approx 20$ mK) ensures that no thermal excitation takes place, and in general creates a very low noise environment. Moreover, single photon limit also requires very low input power such that the device is probed with few photons on average. For this reason the input lines are strongly attenuated (see Fig.3.6). The circulating power P_{cir} corresponding to the number of photons in the resonator N_{ph} depends on the coupling capacitor (see section 2.4), therefore the actual input power is tuned by room temperature attenuators.

In figure 3.6 a schematic representation of the experimental setup employed for microwave measurements is shown. The different stages of the dilution refrigerator with all the microwave components used are depicted. In particular, the samples are glued in a

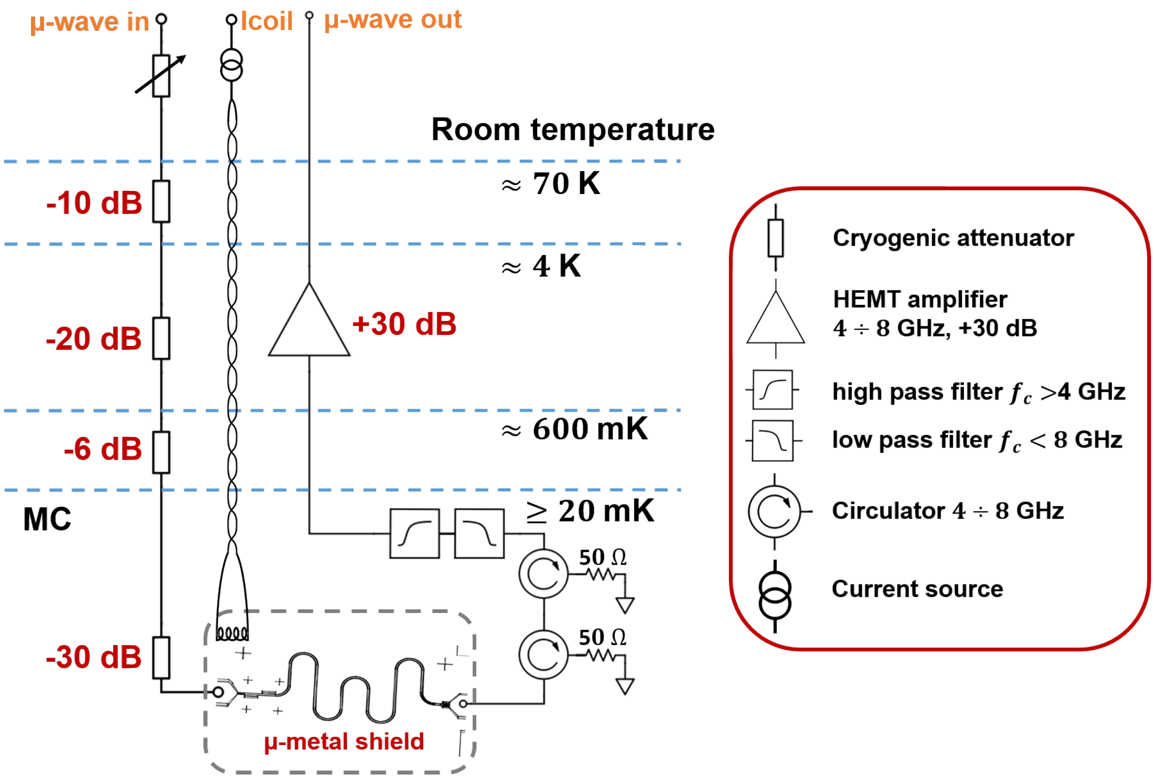

Figure 3.6: Schematic of the experimental setup used for microwave measurements from room temperature down to the lowest stage of the dilution cryostat. The different instruments and components are labeled.

home made rf-tight, oxygen-free cooper box, containing a PCB whose center conductor is soldered to microstrip launchers connected through the box to SMA connectors via glass beads. The sample box is thermally anchored to the mixing chamber (MC) of the dilution refrigerator. A NbTi coil is attached to the sample box for magnetic flux biasing of the transmon device. Moreover, a μ-metal shield is used to screen the devices from ambient magnetic field[3]. The transmitted[4] signal via the two circulators in series is filtered and

[3]No μ-metal shield is used for the measurements at high magnetic field.

[4]For reflectivity measurements, a similar experimental setup has been used. More details can be found on the appended papers[102, 138].

then amplified by a HEMT low noise cryogenic amplifier ($T_{noise} \approx 2$ K) placed at the ≈ 4 K stage, before reaching the room temperature detection instrumentation. The circulators also prevent that black-body radiation from the different thermal stages reaches the device along the output line, which is not attenuated (see Fig.3.6). This experimental setup has been successfully tested via the measurement of low-T_c superconducting transmon qubit and single photon router devices reported in refs. [139, 140]. At room temperature, multi-tones probing of the devices is possible thanks to two different microwave generators and a power combiner, as schematically illustrated in Fig.3.7. The input microwave signals are shaped by arbitrary waveform generators and frequency mixers. Here the mixers are used as switches, which are turned on by DC pulses. The output signal instead, after a further amplification, is sampled and downconverted by a microwave digitizer with an operational frequency up to 6 GHz. For the microwave losses investigation via reflectivity measurement, instead, a vector network analyzer (VNA) has been used for both generation and detection of the microwave signal. The VNA allows for the measurement of both the amplitude and the phase of the complex reflected signal V_{out}/V_{in} within the specified frequency range (up to 20 GHz).

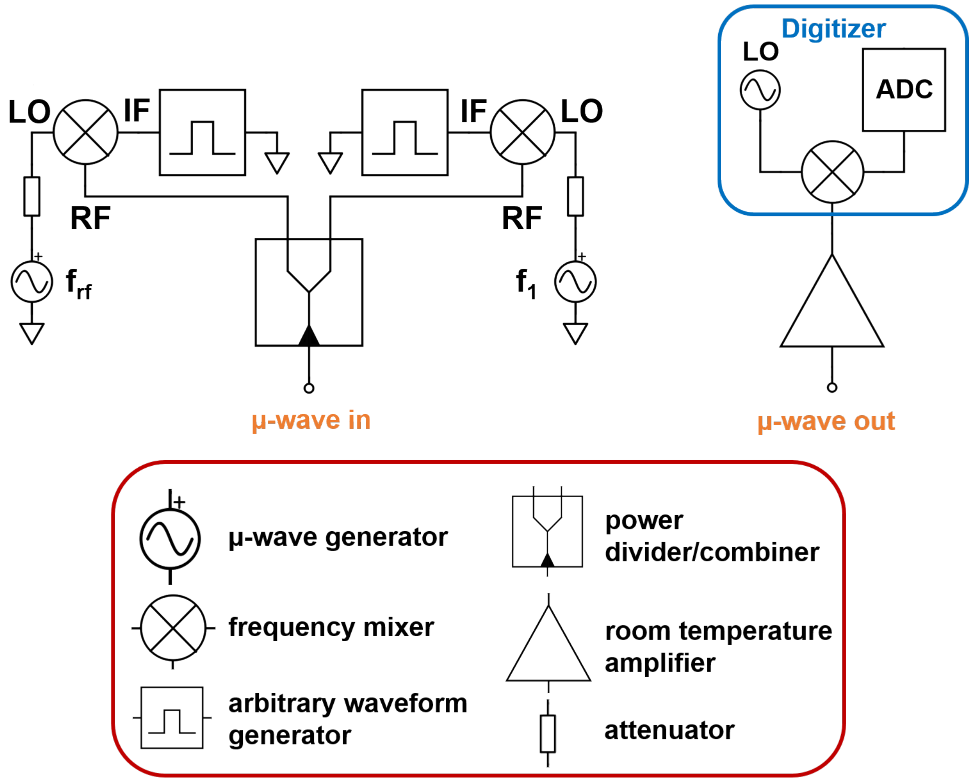

Figure 3.7: Schematic of the room temperature experimental setup used for microwave measurements. The different instruments and components are labeled.

Noise characterization

The magnetic flux noise characterization of the nanoSQUIDs has been performed in an open loop configuration and using a cross correlation scheme. A schematic of the employed experimental setup is sketched in Fig.3.8. The cross correlation setup was used to reduce the contribution of the amplifiers input noise to the total measured voltage noise. Using typically $N \simeq 100$ number of averages, a reduction of the voltage input noise contribution from 4 nV/$\sqrt{\text{Hz}}$ (single amplifier) down to ≈ 0.7 nV/$\sqrt{\text{Hz}}$ is obtained with two amplifiers in a cross correlation scheme. As it is shown in Fig. 3.8, the nanoSQUID device is current biased by a DC-current slightly larger than its critical current value, and flux biased to a working point corresponding to the maximum of the transfer function of the voltage-magnetic flux characteristic $V(\Phi_e)$, defined as: $V_\Phi = \max(\frac{\partial V}{\partial \Phi_e})$. Then the cross correlated voltage noise density across the device $S_V^{1/2}$ is measured. Finally, the flux noise $S_\Phi^{1/2}$ is evaluated using the following expression: $S_\Phi^{1/2} = S_V^{1/2}/V_\Phi$.

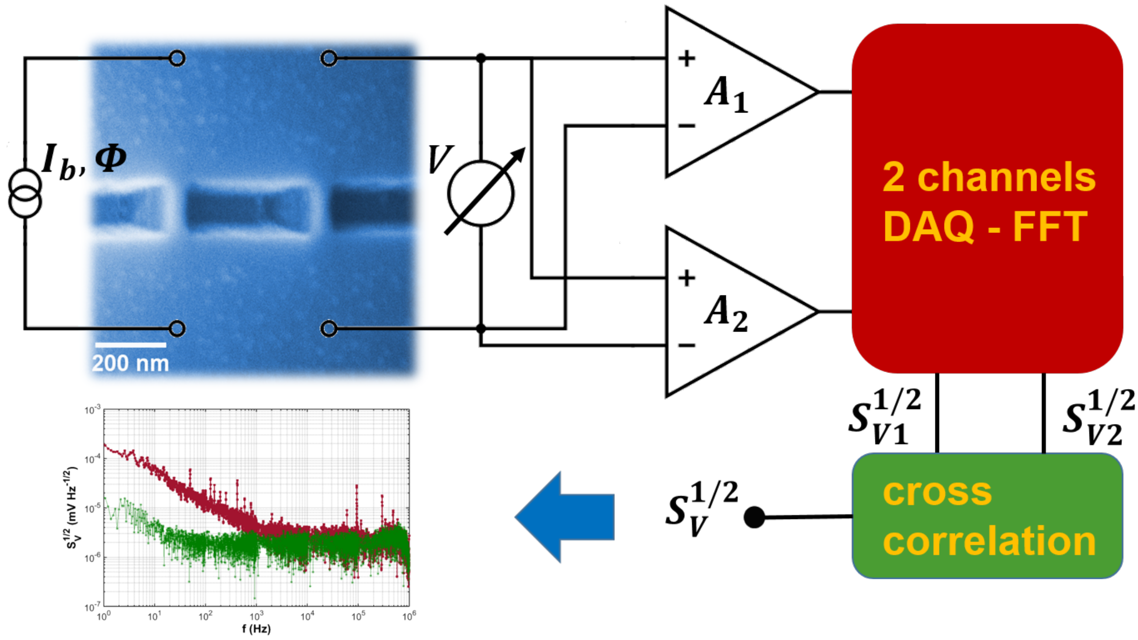

Figure 3.8: Schematic of experimental setup for noise characterization of the nanowire based nanoSQUIDs. A_1 and A_2 are two differential voltage amplifiers. $S_V^{1/2}$ is the cross correlated noise spectral density. An example of a measured flux noise spectral density is also shown.

Chapter 4

YBCO nanowire based nanoSQUIDs

This chapter is an extension of the appended papers I and II. Here the results from the electrical transport characterization of YBCO nanoSQUIDs implementing nanowires in a so-called Dayem bridge configuration are reported. First, the device is shortly introduced (see section 2.3.2 for details of the working principles), with a particular focus on the possible applications such as magnetic flux sensors and basic studies related to the fundamental charge of the superconducting condensate. Next, the critical current modulations as a function of the externally applied magnetic flux $I_c(\Phi_e)$, measured in the whole range of temperature up to the T_c of the device, are presented. The extracted values of the periodicity and modulation depth for I_c are successfully compared to numerical calculations. Finally, the noise performances of the nanoSQUIDs, also in the presence of an inductively coupled pickup loop to increase the effective area, are discussed and analyzed in details.

4.1 Motivations and design

The electron-electron attraction responsible for the formation of Cooper pairs is the base on which the BCS theory for conventional superconductors is built (see section 1.2). Indeed, for a full understanding of the microscopic physical mechanisms in cuprates high-T_c superconductors, the knowledge of the charge pairing represents an essential requirement. In order to determine the fundamental charge e^* of the condensate, different methods such as: Little-Park experiment[141] and Shapiro steps measurements[142, 143], have been pursued, and all seem to agree on a predominant $2e$ charge pairing. However, the recent experimental demonstrations of the existence of different forms of order, including pair density wave (PDW), for which a spatial periodic modulation of the order parameter has been observed[144], have led to a reconsideration of the charge pairing in cuprates. In particular, a $4e$ superconducting state has been theoretically predicted as direct consequence of the presence of PDW[145]. The fundamental charge of the superconducting state can be extracted from the value of the flux quantum Φ_0, for example by looking at the fluxoid quantization via transport measurement in superconducting loops. For a BCS superconductor the fundamental charge is given by the Cooper pair and results in $\Phi_0 = h/2e$. Instead, for a superconductor with a pair density wave order (periodic variation of the pair density in space), a $4e$ superconducting state has been predicted resulting in a value of the flux quantum $\Phi_0 = h/4e$[145]. For this task, nanoSQUID loops implementing nanowires, with lateral dimensions comparable to the characteristic length of PDW ($\simeq$ 10 nm) and characterized by highly uniform superconducting properties, represent ideal candidates.

Furthermore, nanoSQUIDs have attracted a lot of attention because of their extremely high magnetic flux sensitivity. Flux noise, in fact, depends on the total inductance of the device ($S_{\Phi}^{1/2} \propto L^{3/2}$), therefore a nanometer sized loop is needed to reduce it (see section 2.3.2). Indeed, with nanoSQUIDs the magnetic flux sensitivity can be significantly improved, enabling the possibility of quantum limited measurements. For this reason nanoSQUIDs are ideal magnetic flux sensors for applications in nanomagnetism, aiming at the detection of a single spin, which represents a holy grail in fundamental measurement techniques[76]. While this technology is well established for LTS[146], the realization of HTS nanoSQUIDs has made significant improvements only during the last few years[147, 148, 149]. The use of HTSs allows to extend the operation range for both temperature and magnetic field, due to the larger values of the critical temperature T_c and the upper critical magnetic field H_{c2} (see table 1.1 for a numerical comparison between YBCO and the most common LTSs). However, other important SQUID applications, such as magneto encephalography[12, 13] and low field magnetic resonance imaging[14], require a low magnetic field noise: $S_B^{1/2} = S_{\Phi}^{1/2}/A_{eff}$, where A_{eff} is the effective area of the device. Due to their small loop area, nanoSQUIDs have a poor magnetic field sensitivity. In order to increase the effective area A_{eff} of the device, while keeping the low flux noise (small loop area), with a consequent improvement of the magnetic field sensitivity, one can directly couple the nanoSQUID to a much larger pickup loop. The pickup loop approach is preferable over a SQUID washer design[16], since the implementation of a large washer to enhance the effective area will at the same time also increase the SQUID inductance. Moreover, it only involves a single layer patterning technique, making the pickup loop simpler and more attractive compared to an inductively coupled multiturn flux transformer.

YBCO nanowire based nanoSQUIDs have been realized on c-axis oriented 50 nm thick films deposited on MgO(110) and MgO(001) substrates, using the patterning technology described in details in section 3.2[1]. In figure 4.1 SEM and AFM images of the typical devices are shown in false colors. The main geometrical dimensions are labeled. The nanometer sized nanoSQUID loop is realized in the so-called Dayem bridge configuration: two nanowire $65 - 100$ nm wide (w_n) and with a length l ranging between 100-300 nm, connect two electrodes whose width w_e ranges from 4 μm to 16 μm. The separation distance between the two nanowires d_w has been varied from few hundreds of nm up to 1 μm. For nanoSQUIDs coupled to the pickup loop, the width and the length of the two nanowires is kept fixed to 65 nm and 200 nm, respectively. The nanowires act as bridges between an electrode, 1 or 2 μm wide (d_w), and a pickup loop, whose inner diameter d ranges from 40 μm up to 400 μm (see Fig.4.1(c) and (d)). As it infers from eq. (2.32), for these specific devices, the coupling inductance L_c plays the major role in determining the increment of the effective area. In order to enhance the value of L_c, the pickup loop is designed such that its width w is 2 μm in the vicinity of the nanowires and it then widens up to 10 μm over a distance of $\approx 30\,\mu$m far from them (see Fig. 4.1(c) and (d)).

[1]For these devices the gold capping layer is kept after the fabrication process.

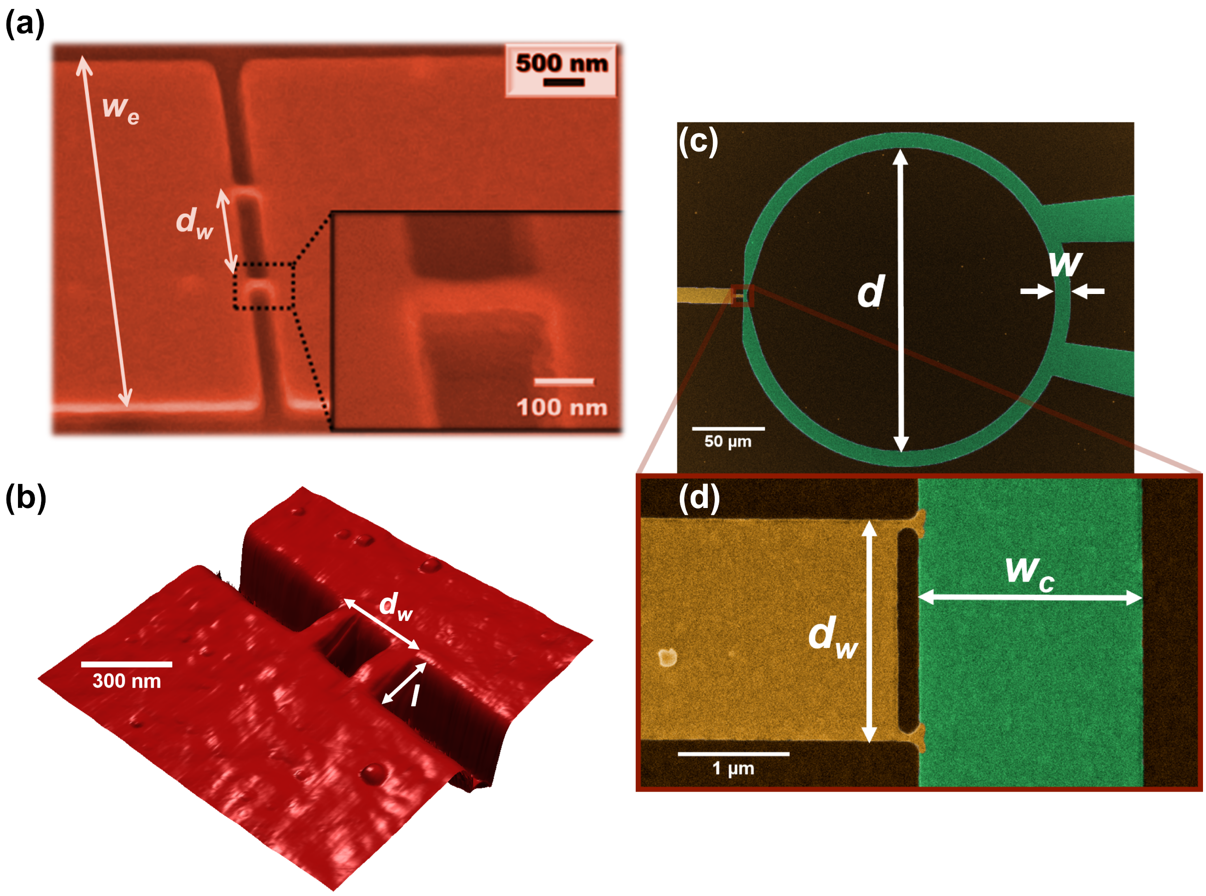

Figure 4.1: Collection of SEM and AFM images of typical YBCO nanowire based nanoSQUIDs, both bare nanoSQUIDs and inductively coupled to an in-plane large pickup loop. The YBCO structures are shown in false colors, whereas the dark regions represent the MgO substrate. (a) SEM image and (b) 3D AFM image of two typical nanoSQUID devices. w_e is the width of the electrode, l is the nanowire length and d_w is the separation distance between the two nanowires. (c) Overview of a typical nanoSQUID device coupled to a pickup loop, showing the geometry of the pickup loop (green regions), the diameter d and the width w are labeled. (d) Zoom-in highlighting the device in the vicinity of the nanowires. The nanoSQUID loop is formed by a narrow electrode (orange region) connected to the pickup loop (green) via the two nanowires. d_w and w_c are respectively the separation distance between the two bridges and the the width of the pickup loop in the vicinity of the nanowires.

4.2 Electrical transport characterization

In this section the electrical transport characterization of the nanoSQUIDs, with a particular focus on the critical current modulation as a function of the external magnetic flux $I_c(\Phi_e)$, is presented. The transport measurement has been performed at low temperature in a ^{3}He cryostat, properly shielded from ambient magnetic field (see section 3.3). The devices are characterized by critical current densities in the range of $3-6\times10^7$ A/cm^2 at $T = 5$ K, close to the GL depairing limit[134, 135]. The IV characteristics show typical flux-flow behaviour, and a supercurrent is observed up to the critical temperature of the device ($T_c \simeq 83$ K). In figure 4.2 (a) a typical IV curve of a nanoSQUID, measured at

$T = 5$ K, is shown. Figure 4.2 (b), instead, shows the resistance vs temperature measurement of a nanoSQUID. The fitting method, from which one can extract the values of T_c, λ_0 and ξ_0, are based on the thermal assisted vortex entry model and are described in ref.[150]. The critical current modulations as a function of the externally applied mag-

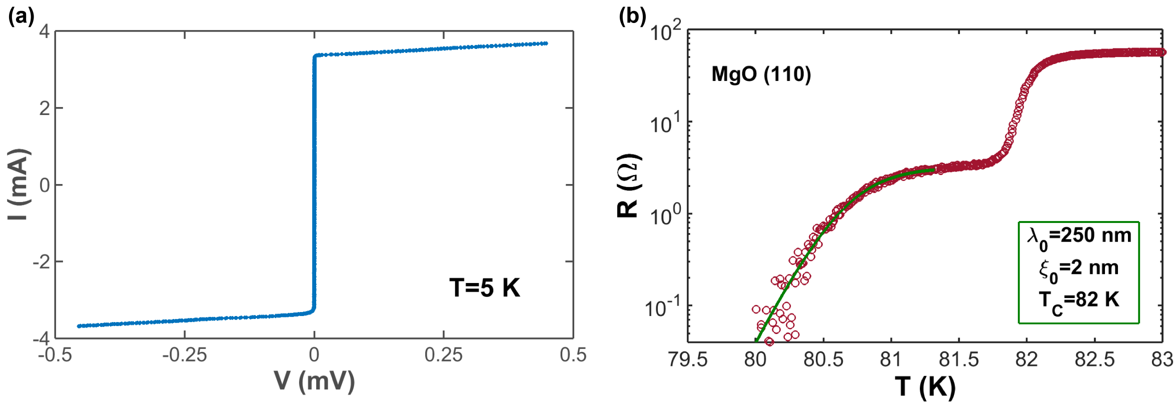

Figure 4.2: (a) Typical IV characteristic of a nanoSQUID device measured at $T = 5$ K. (b) Resistance versus temperature of a typical nanoSQUID. The solid line represents the fit to the thermal assisted vortex entry model.

netic flux and field for different nanoSQUIDs, including the case of a device coupled to a pickup loop, are shown in Fig. 4.3. The critical current values have been extracted from the measured IV characteristics using a voltage criterion, which has been chosen taking into account the shape and the noise level of the IV curves. Nevertheless, this voltage value is commonly of the order of $\approx 2\,\mu$V. The $I_c(\Phi_e)$ modulations are characterized by a more triangular shape compared to Josephson junctions based SQUIDs, as expected from the non sinusoidal current-phase relation characterizing nanowires with lateral dimensions larger than the coherence length ($w, l > \xi$, see section 2.3.2). Moreover, the effect of the non negligible inductance of the nanowires, mainly kinetic (L_{kin}), results in a $\beta_L \neq 0$ and consequently in a relative modulation depth $\Delta I_c/I_c^{max} = (I_c^{max} - I_c^{min})/I_c^{max}$ much smaller than 1. The nanoSQUID $I_c(\Phi_e)$ is superimposed on the critical current modulation of a single nanowire. This results in a tilting of the $I_c(\Phi_e)$ (different lobes are characterized by slightly different I_c^{max}) as it can be clearly seen in Fig. 4.3(a) and (b). It is important to highlight that the nanoSQUIDs presented here exhibit critical current modulation in the whole range of temperature up to the T_c of the device (see Fig. 4.3(b)). This represents a big step forward compared to previously reported HTS nanoSQUIDs[151, 152], whose operational temperature range has always been limited due to the detrimental effects of the fabrication methods employed. Another crucial result, which can be deduced comparing Fig. 4.3 (c) and (d), is the significant reduction of the modulation period ΔB when the nanoSQUID loop is inductively coupled to a much larger pickup loop (400 μm in the case reported in Fig. 4.3 (d)). Finally, figure 4.3 also suggests a temperature dependence of the critical current modulation depth ΔI_c, which can be extracted from the $I_c(B)$ plots as illustrated in the Fig. 4.3 (a). In the next section, a quantitative analysis of the temperature dependence of ΔI_c, in comparison to numerical calculations, is discussed. A comparison between numerical estimations and experimental data for the effective area of the different nanoSQUIDs configurations employed is made as well.

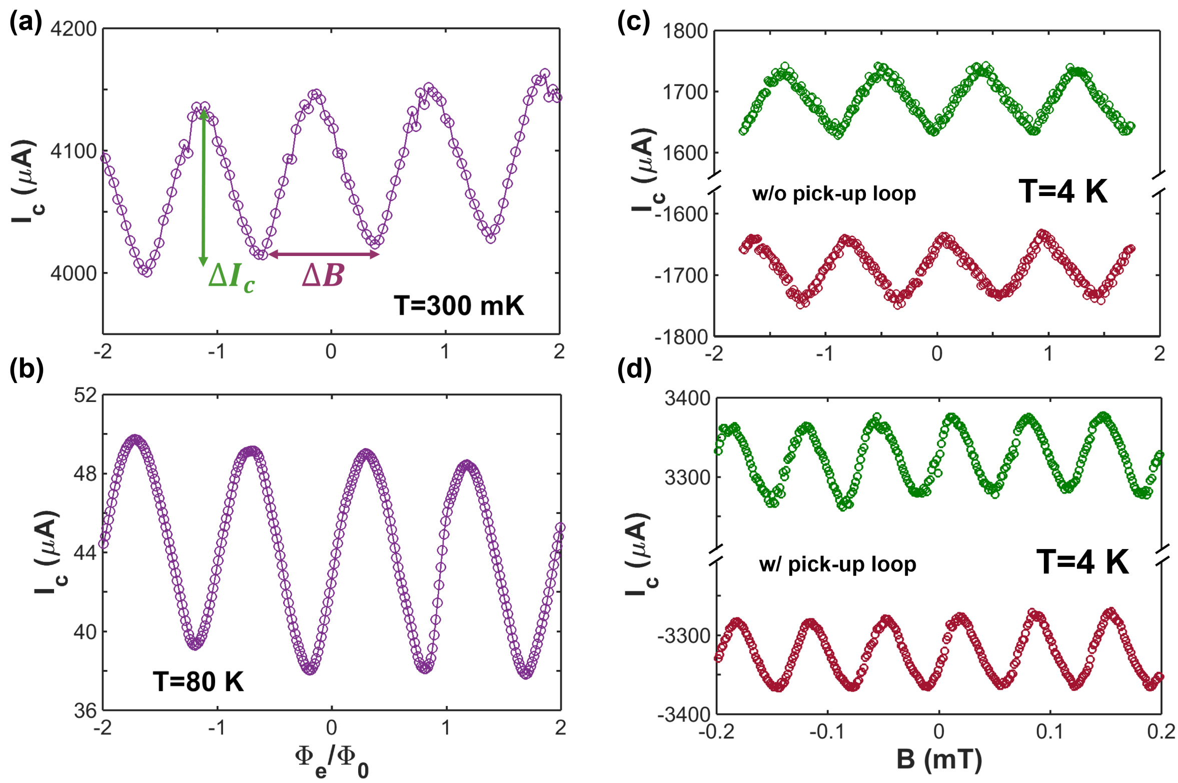

Figure 4.3: Critical current modulations as a function of the externally applied magnetic flux and field. (a) $I_c(\Phi_e)$ for a nanoSQUID at $T = 300$ mK. ΔI_c is the difference between the maximum and the minimum values of I_c, and ΔB is the modulation period. (b) $I_c(\Phi_e)$ for the same nanoSQUID device as in (a) at $T = 80$ K. (c) $I_c(B)$ for a nanoSQUID without and for another one with pickup loop (d) measured at $T = 4$ K. Although the nanoSQUID loops are characterized by similar geometrical areas, the presence of the pickup loop results in a larger A_{eff} and a significant smaller ΔB.

4.3 Numerical analysis

As discussed in section 2.3.2, the CPR for bridges with dimensions as the nanowires implemented for the nanoSQUID devices reported here is given by the Likharev-Yakobsen expression (2.25). The effect of the CPR of the nanowires on the critical current modulation can be accounted for by adding the kinetic inductance of the nanowires to the total SQUID inductance. Therefore, the total inductance L_{nS} of the nanoSQUID loop can be modelled as the sum of the wires and the electrodes inductances. In particular, the main contribution to L_{nS} comes from the kinetic inductance of the two nanowires, which at base temperature ($T = 300$ mK) is an order of magnitude larger than the geometric one $L_{ex}^{nw} \simeq \mu_0 l$ ($L_{kin} \approx 15$ pH). In fact, the critical current modulation depth ΔI_c is given by $\Delta I_c = \frac{\Phi_0}{L_{nS}}$, and at fixed temperature, nanoSQUIDs characterized by a larger inductance will exhibit a smaller ΔI_c (see section 2.3.2). In order to calculate ΔI_c, a numerical estimation of the nanoSQUID total inductance is needed. Numerical methods, based on the solution of the Maxwell and London equations (see Appendix C for details), allow to estimate L_{nS}. The numerical calculation can be used for any geometry of the superconducting loop. To account for the temperature dependence, a modified two-fluid model expression for the London penetration depth has been used:

$$\lambda_L(T) = \frac{\lambda_0}{\sqrt{1 - \left(\frac{T}{T_c}\right)^n}}, \quad (4.1)$$

where λ_0 is the London penetration depth at zero temperature and n is an experimentally determined power exponent, which commonly is ≈ 2 for YBCO thin films. In figure 4.4, the experimental values of $\beta_L^{exp}(T)$ calculated as:

$$\beta_L^{exp}(T) = \frac{I_c^{max}(T)}{\Delta I_c(T)} \quad (4.2)$$

are plotted (open circles) as a function of the temperature up to the T_c, for nanoSQUID devices patterned on both MgO(110) and MgO(001) substrates. The dashed lines represent numerical estimations given by:

$$\beta_L^{num}(T) = \frac{I_c^{max}(T) L_{nS}^{num}(T)}{\Phi_0}, \quad (4.3)$$

for which λ_0 has been used as the only fitting parameter (I_c^{max} is taken from experimental data and n has been kept fixed to 2). A $\lambda_0 = 260$ nm value, typical for nanometer sized YBCO devices[147, 150], results in numerical estimations that are in very good agreement with the experimental data (see Fig. 4.4). In particular, in the case of the nanoSQUIDs patterned on top of MgO(110), an anisotropy for the London penetration depth in the $ab-$plane has been considered ($\lambda_L^b = \lambda_L^a/1.3$). This is a direct consequence of the untwinned growth of the YBCO on such substrate, with the nanowires patterned along the $b-$axis. On the contrary, the YBCO films are twinned when grown on the MgO(001) substrate, and consequently no anisotropy in the $ab-$plane transport is present. Comparable estimations of λ_0 have been obtained by fitting the resistance versus temperature of the devices (see Fig. 4.2)(b). This further confirms the correctness of the numerical calculations used to quantitatively analyze the critical current modulations extracted from the electrical transport characterization of the nanoSQUIDs.

Using the same numerical methods, the effective area of the nanoSQUIDs can be evaluated and compared to the experimental A_{eff}^{exp}, extracted from the critical current periodicity in applied magnetic field ΔB: $A_{eff}^{exp} = \Delta B/\Phi_0$. Here it is important to emphasize that the value of the flux quantum $\Phi_0 = h/e^*$ to be used depends on the fundamental charge of the superconducting state e^*, which commonly is given by: $e^* = 2e$. Therefore a proper numerical estimation of the device effective area is crucial to get insights about the pairing in YBCO nano-structures. First, it has to be noted that A_{eff}^{exp} is larger than the nanoSQUID geometric area, which for our specific design (see figure 4.1) is given by the product of the separation distance between the two nanowires and their length: $A_{geo} = d_w * l$. This is a consequence of the extra phase gradient $\Delta\phi$ between the two nanowires produced by the screening current I_s in the electrodes or in the pickup loop, if the latter is present. The effective area of the device can be numerically estimated from the magnetic moment generated by the screening current in the nanoSQUID loop, as expressed by Eq. (C.9). In figure 4.5 both the experimentally obtained and the numerically

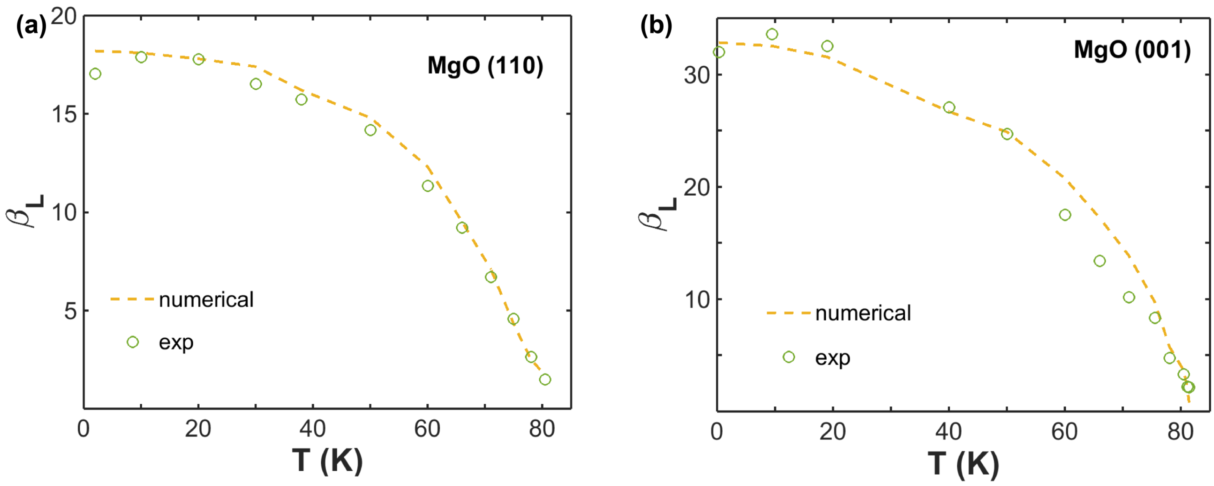

Figure 4.4: Temperature dependence of the screening inductance factor β_L (green open circles) for a YBCO nanoSQUID patterned on an MgO(110) (a) and MgO(001) (b) substrates. The orange dashed line represents the numerical calculations.

estimated effective area values are plotted as a function of the separation distance between the two nanowires. Here, the length l and the electrode width w_e are kept fixed to 150 nm and 4 μm respectively. No pickup loop has been employed in this case. Experimental

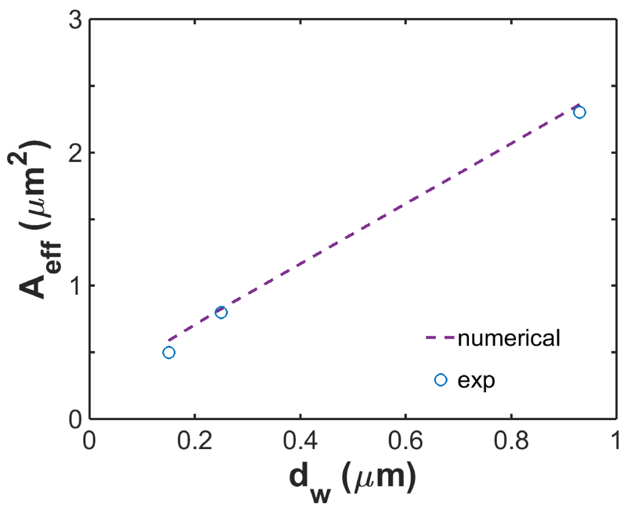

Figure 4.5: Experimental effective area (open light blue circles) as function of the separation distance of the two nanowires d_w. The values of A_{eff}^{exp} have been calculated from the critical current modulation periodicity of nanoSQUIDs characterized by the same wires length ($l \approx$ 150 nm) and same electrodes width ($w_e = 4\,\mu$m). The dashed line represents the numerical estimations.

data and numerical calculations are in a very good agreement, using the standard value for the fundamental charge $e^* = 2e$ in the evaluation of A_{eff}^{exp}. Therefore, there is no clear hints of the effect of PDW on the charge pairing in the presented devices. One possible explanation could be related to the fact that the nanoSQUIDs have been patterned on YBCO films close to the optimal doping, whereas the presence of PDW has been predicted and experimentally observed for underdoped cuprates. Indeed, nanodevices patterned on underdoped YBCO films could provide better evidences regarding eventual effects due to the presence of PDW[94]. Moreover, the data resemble a scaling of the effective area $A_{eff} \simeq \frac{w_e d_w}{1.5}$, which is comparable to the one determined from flux focusing effect on thin film grain boundary Josephson junctions[153].

In the case of nanoSQUIDs inductively coupled to a pickup loop, the numerical estimation of the effective area is slightly more complicated by the presence of the two interacting loops. To calculate the current distribution in the SQUID structure, the pickup loop in the zero flux state (zero vorticity) and no circulating current in the nanoSQUID loop have been assumed. Given the current distribution, the effective area can be estimated from the computation of the fluxoid Φ' around the nanoSQUID loop and the externally applied magnetic field B: $A_{eff}^{num} = \Phi'/B$ (see Appendix C for details). The effective areas calculated in such a way can be furthermore compared to values calculated via Eq.(2.32) and using the following analytic expressions, including both the geometric (L_{ex}) and the kinetic (L_{kin}) contributions to the pickup loop L_{loop} and the coupling L_c inductance[154]:

$$\begin{aligned} L'_{loop} &= \frac{\mu_0 \lambda_L}{w} \coth\left(\frac{t}{\lambda_L}\right) + \frac{\mu_0}{2\pi}\left[\ln\left(\frac{16r}{w}\right) - 2\right] \\ L'_c &= \frac{\mu_0 \lambda_L}{w_c} \coth\left(\frac{t}{\lambda_L}\right) + k/2. \end{aligned} \tag{4.4}$$

Here, w and r are the average radius and width of the pick-up loop respectively, and w_c is the width of the YBCO strip where the two loops meet (see Fig.4.1(d)). $k \simeq 0.3$ pH/μm is an empirical expression for a slit inductance per unit length, obtained from measurements and simulations[16]. The geometric term of L'_c is, thence, approximated as half slit inductance. The prime sign indicates that equations (4.4) are per unit length.

Figure 4.6 shows the experimentally determined effective area A_{eff}^{exp} versus the pickup loop inner diameter d, for nanoSQUIDs with nanowires separation $d_w = 1\,\mu$m (open circles) and $d_w = 2\,\mu$m (diamonds), both at $T = 5$ K and at $T = 77$ K. The solid and the dashed lines represent respectively the numerically estimated (A_{eff}^{num}) and the analytically calculated (A_{eff}^{an}) effective area. Figure 4.6 indicates a much better agreement between experimental data and the numerical method compared to the values obtained via the analytic expressions. In this case, the best fitting of A_{eff}^{exp} has been obtained using $\lambda_0 = 150$ nm at $T = 5$ K, and a $\lambda_L(T = 77\text{ K}) \approx 400$ nm, calculated using eq.(4.1) with $T_c = 83$ K and $n = 2$. The smaller value (closer to the one for bulk YBCO) for λ_0 compared to the one used for the nanowire inductance in nanoSQUIDs in absence of the pickup loop, could be related to the much larger lateral dimensions of the entire SQUID device. On the contrary, the analytic estimations do not provide a good fitting for any of the λ_0 value in the range $150 - 260$ nm. This reflects an inaccuracy in the evaluation of the geometric inductance, which would be even more pronounced if more complex device geometries are employed.

Finally, it is important to highlight that in the presented devices the kinetic contribution dominates over the geometric one for the coupling inductance L_c. In fact, the geometric term accounts only for $\approx 34\%$ at $T = 5$ K, and only for roughly the 7% at $T = 77$ K, with a ratio $L_c^{kin}/L_c^{ex} \approx 14$. Indeed, the coupling between the nanoSQUID

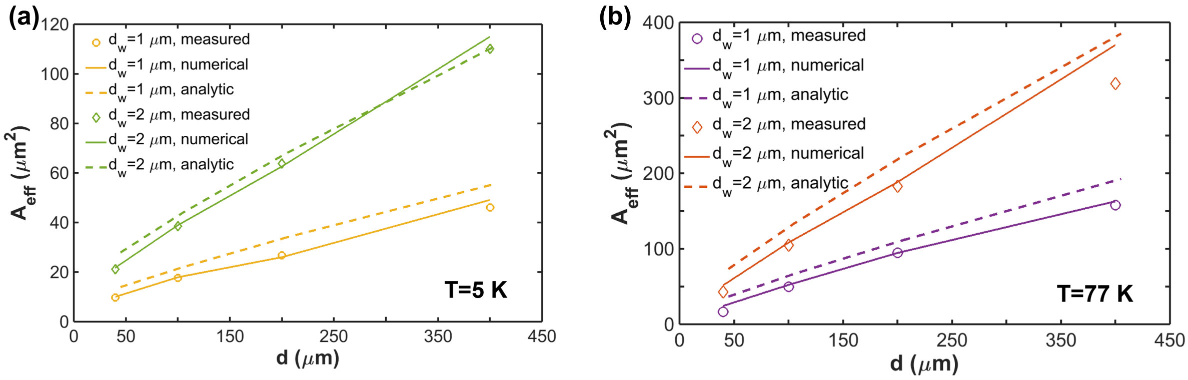

Figure 4.6: Experimentally determined effective area as a function of the pickup loop inner diameter d, for nanoSQUIDs with a wires separation of 1 μm (open circles) and 2 μm (diamonds), obtained at $T = 5$ K (a) and $T = 77$ K (b). The solid and the dashed lines represent the numerical and the analytic calculations, respectively.

loop and the pickup loop takes place mainly via kinetic inductance. For this reason, these devices, with an optimized geometry, could be employed for the measurement of the London penetration depth in superconducting thin films.

4.4 Noise characterization

In this last section of the chapter the magnetic flux noise characterization is presented and analyzed for nanoSQUID devices with and without pickup loop. However, here a particular attention is paid on the effect of the pickup loop on the noise performances. While the results presented in the previous section demonstrate that the pickup loop allows for a significant increase of the device effective area, the effect of the pickup loop on the flux noise needs to be discussed. The flux noise measurements have been performed using an open loop configuration and a cross correlation scheme, as described in details in section 3.3. Figure 4.7 shows the magnetic flux noise spectrum $S_\Phi^{1/2}$ for a typical device in absence of the pickup loop. As result of the nanometer sized loop, nanoSQUIDs exhibit an ultra low flux noise, characterized by a white level below 1 $\mu\Phi_0/\sqrt{\text{Hz}}$ limited by the electronics background. This value is among the lowest reported in literature for generic HTS nanoSQUID devices[147, 148, 149]. In Figure 4.8(b), instead, a typical spectral density of magnetic flux noise, measured at T=5 K for a nanoSQUID coupled to a pickup loop, is shown. In particular, the reported measurement is taken at a DC bias current $I_b = 1.76$ mA and a flux bias such that $V_\Phi = 2.4$ mV$/\Phi_0$, as shown in Figure 4.8(a). The measured flux noise is frequency dependent, with a value of about 100 $\mu\Phi_0/\sqrt{\text{Hz}}$ at $f = 10$ Hz, and it is limited by the electronics noise background (violet line) for frequencies above 100 kHz. Therefore, an upper limit of $S_\Phi^{1/2} \simeq 1$ $\mu\Phi_0/\sqrt{\text{Hz}}$ is taken as the white noise level of the device. As for the device presented in Fig. 4.7, the $f-$dependent noise is not realted to the flux bias point, thence it has to be attributed to critical current fluctuations. While critical current fluctuations in ordinary tunnle-like JJs are usually associated to the presence of bistable charge trapping states modifying the junction barrier transparency (see section 2.3.1), there is no clear evidence of their physical origin in nanowires. Here, critical

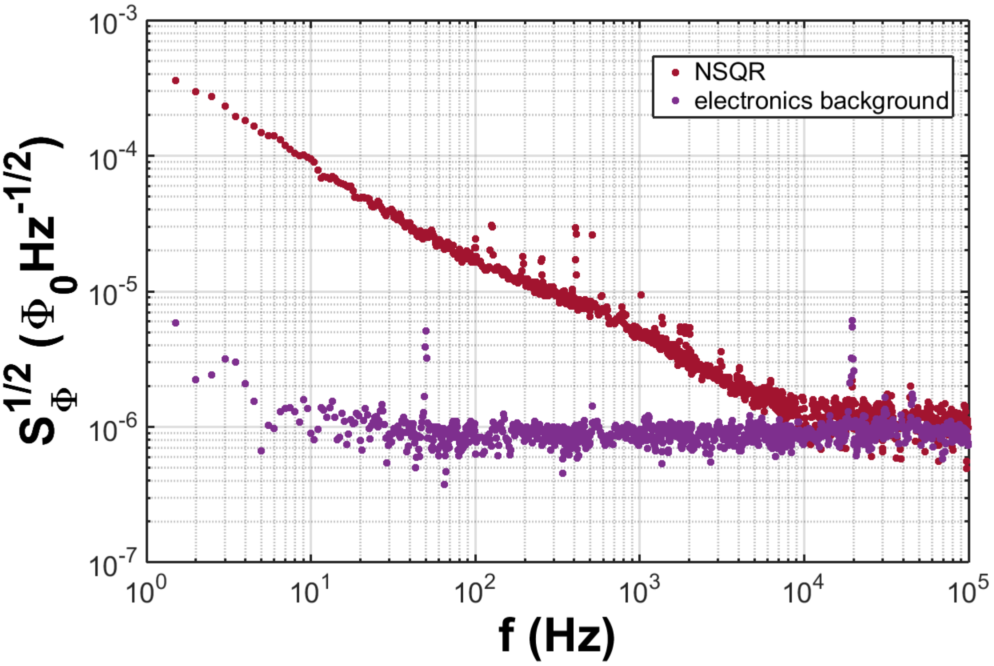

Figure 4.7: Magnetic flux noise spectrum (dark red disks), measured at $T = 8$ K, for a nanoSQUID in absence of the pickup loop (NSQR). The electronics background noise spectrum is also plotted (violet disks).

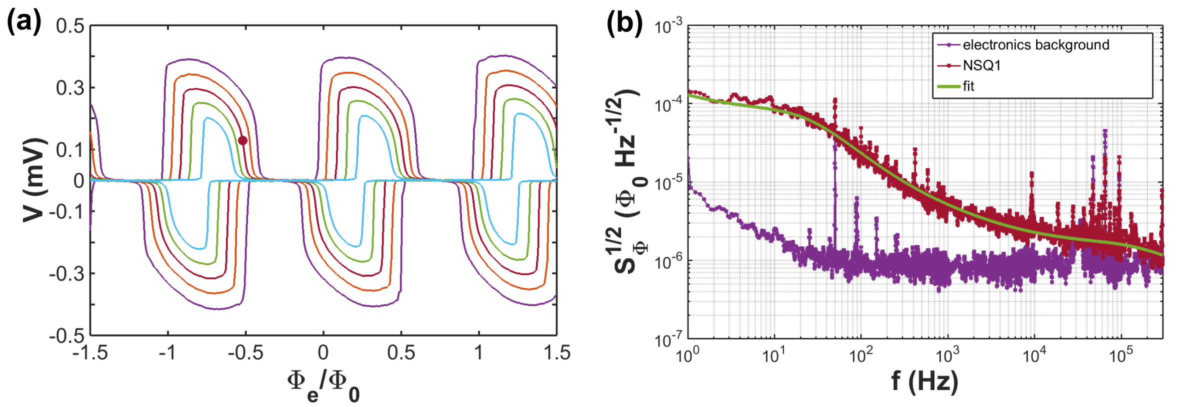

Figure 4.8: (a) Voltage versus external magnetic flux for different DC bias currents. The dark red dot indicates the working point ($I_b = 1.76$ mA), at which the flux noise spectrum has been measured, corresponding to a transfer function $V_\phi = 2.4$ mV$/\Phi_0$. (b) Magnetic flux noise spectrum (dark red line), measured at $T = 5$ K, for a nanoSQUID characterized by $d_w = 1\,\mu$m and a pickup loop with an inner diameter $d = 100\,\mu$m (NSQ1). The solid green line represents the fit to $F^{1/2}(f)$. The electronics background noise spectrum is also plotted (violet line).

current noise could be caused by fluctuations of the electronic nematic order[155, 156] or by changes in the oxygen order and concentration in the CuO chains[157], resulting in a variation of the energy barrier for the vortex entry dynamics in the nanowires[158]. However systematic studies, including geometry and temperature dependencies, are needed for a complete and clear understanding of the physical mechanisms responsible for such behavior. Moreover, using a flux-locked loop (FLL) configuration in combination with a bias reversal scheme, the effect of the critical current fluctuations on the flux noise can be eliminated. Nevertheless, a more detailed and quantitative analysis can be done by fitting the spectrum to the sum of one or more Lorentzians $F_{L,i=}^{1/2}F_{0,i}^{1/2}/[1+(f/f_{c,i})^2]^{1/2}$ with an amplitude $F_{0,i}^{1/2}$ and a characteristic frequency $f_{c,i}$, a contribution $F_{1/f}^{1/2} \propto 1/f^{1/2}$, and a constant white noise term $F_w^{1/2}$. In Figure 4.8(b) the solid green line represents the fit to the expression $F^{1/2}(f) = \sqrt{\Sigma_i F_{L,i} + F_{1/f} + F_w}$. For the presented measurement, the best fitting is obtained using two Lorentzians, and the following parameters have been extracted: $f_{c,1} = 25$ Hz, $F_{0,1}^{1/2} = 80\ \mu\Phi_0/\sqrt{\text{Hz}}$ and $f_{c,2} = 200$ kHz, $F_{0,2}^{1/2} = 1.4\ \mu\Phi_0/\sqrt{\text{Hz}}$, and a white noise $F_w^{1/2} = 0.8\ \mu\Phi_0/\sqrt{\text{Hz}}$.

For a direct comparison of the flux noise measured for nanoSQUIDs with and without pickup loop, the main parameters including the effective area and the magnetic field white noise level (or its upper limit as set by the read-out electronics employed), are listed in table 4.1. These results indicate that the magnetic flux noise performances of

Device	**d**(μ)m	$\mathbf{A_{eff}}(\mu m^2)$	$\mathbf{V_\Phi}(mV/\Phi_0)$	$\mathbf{S_{\Phi,w}^{1/2}}(\mu\Phi_0/\sqrt{Hz})$	$\mathbf{S_{B,w}^{1/2}}(pT/\sqrt{Hz})$
NSQ1	100	24	2.4	<1	<86
NSQ2	400	62	0.75	<2	<66
NSQR	-	2.8	1.5	<1	<740

Table 4.1: Main parameters of some investigated nanoSQUIDs, characterized by different effective areas. V_Φ is the value of the transfer function at the work point used for the noise measurement at $T = 5$ K. $S_{\Phi,w}$ is the magnetic flux white noise upper limit of the device, as set by the electronics background noise. NSQR is a device without pick-up loop reported for comparison.

the nanowire based YBCO nanoSQUIDs presented in this thesis are not affected by the presence of the pickup loop and the consequent significant increase of the effective area. Therefore, the use of a larger pickup loop ($d \approx 8$ mm) and larger coupling inductance (5 times bigger L_c) would allow to further improve the magnetic field sensitivity and reach a noise level of of $S_B^{1/2} \approx 100$ fT$/\sqrt{\text{Hz}}$, which represents the ultimate goal for various SQUID applications[12, 13, 14, 15].

Noise at 77 K

As regards the SQUID applications, one of the main advantage of using YBCO compared to any LTSs is the possibility to extend the temperature operation range above the liquid nitrogen temperature ($T = 77$ K). In figure 4.9 the magnetic flux spectral density $S_\Phi^{1/2}(f)$, taken at $T = 5$ (violet line) K and $T = 77$ K (yellow line), is shown for two different devices, labelled as NSQ1 (a) and NSQ2 (b) and whose parameters are listed in table (4.1). For both the devices presented here, the white voltage noise at $T = 77$ K is limited by the electronics background. Moreover, once translated into flux noise, the white level is limited to roughly $40\,\mu\Phi_0\text{Hz}^{-1/2}$, as a consequence of the low value of the transfer function V_Φ. This reflects a very low sensitivity to flux fluctuations, due to the small amplitude of

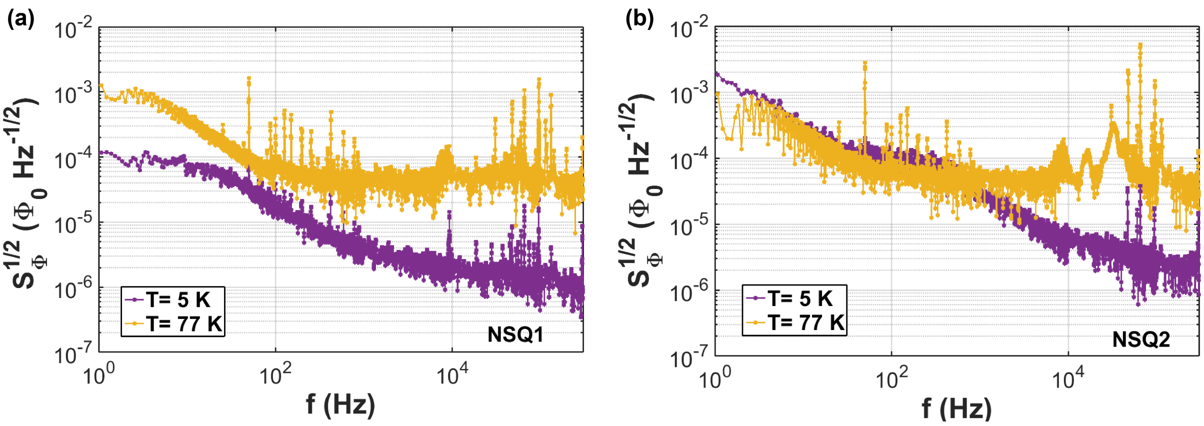

Figure 4.9: Magnetic flux spectrum taken at $T = 5$ K (violet line) and at $T = 77$ K, for the devices labelled as NSQ1 (a) and NSQ2 (b).

the voltage modulation as a function of the externally applied magnetic flux. In order to increase the transfer function and thence improve the flux sensitivity, a larger differential resistance $R_d = \frac{\partial V}{\partial I_b}$ is required. This can be understood by simply writing the relationship between voltage and magnetic flux fluctuations:

$$\delta V = \left(\frac{\partial V}{\partial \Phi}\right) \delta\Phi = R_d \left(\frac{\partial I_b}{\partial \Phi}\right) \delta\Phi. \tag{4.5}$$

A possible way to increase R_d is to employ thinner YBCO films for the realization of the nanowire based nanoSQUIDs, as reported in ref. [159].

Chapter 5

Microwave losses in YBCO resonators in the single photon limit

In this chapter the main results from the characterization of CPW resonators, demonstrating the feasibility of a YBCO transmon, are reported. First, the microwave dielectric losses from the most common substrates employed for the epitaxial growth of YBCO thin films are presented and analyzed. In particular, both the power dependence and the temperature dependence in the single photon limit (millikelvin temperatures and low input power) are discussed. These results indicate $(La_{0.3}Sr_{0.7})(Al_{0.65}Ta_{0.35})O_3$ (LSAT) as ideal dielectric material to be used as substrate for YBCO microwave devices operated in this specific regime. Finally, the microwave properties of YBCO CPW resonators patterned on a $LSAT/CeO_2$ bilayer, suitable for the realization of biepitaxial GB JJ, are presented in comparison to an analogous Niobium resonator.

5.1 Motivations and design

A HTS artificial two-level quantum bit (qubit), realized with YBCO Josephson junctions, could be employed to study fundamental physical mechanisms in previously not easily accessible regimes. In particular, the measurement of the characteristic coherence times of the YBCO JJ would be affected by dissipation and dephasing effects related to the intrinsic nature of the material. Thence, this measurement could deliver detailed information regarding the superconducting ground state and the low-energy quasiparticle excitation spectrum, and provide new hints about the microscopic mechanisms leading to superconductivity in cuprates. However, losses coming from the dielectric materials involved in the fabrication of superconducting circuits operating in the microwave regime, have been recently identified as one of the main sources of dissipation. Many studies about microwave losses, have been performed on sapphire and SiO_2/Si, which are the dielectric materials commonly used for LTSs. For these materials, microwave dielectric losses have been associated to the presence of a bath of two-level systems (TLSs), which couple via their dipole moment $\vec{d}$ to the electromagnetic field in the resonator (see section 2.4 for more details). In the following, a detailed characterization of the dielectric losses from materials compatible with the epitaxial growth of cuprates, in the millikelvin range of temperature and at very low input power (single photon limit), is presented. In particular, the experimental results from the investigation of the microwave proprieties of MgO ($\epsilon_r \approx 9$), $LaAlO_3$ (LAO, $\epsilon_r \approx 25$) and $(La_{0.3}Sr_{0.7})(Al_{0.65}Ta_{0.35})O_3$ (LSAT, $\epsilon_r \approx 23$) in the single photon regime, are presented in comparison to the TLS resonant absorption theory in order to distinguish among different sources of dissipation. Here, ϵ_r is the relative dielectric permittivity at room temperature.

To study the dielectric losses, the unloaded quality factor Q_0 of a Niobium $\lambda/2$ CPW resonator has been extracted from the fitting of the measured complex reflectivity signal (S_{21}). The Nb resonators have been patterned[1] on the different investigated substrates with a specific design, which minimizes radiation losses. Details of the modelling of these devices are extensively described in sections 3.1. The measurements have been performed in a dilution refrigerator using the experimental setup illustrated in section 3.3. In figure 5.1 an optical image of a typical Nb CPW resonator, depicted in false color, is shown. The main geometric dimensions are labelled, and a zoom-in of the finger coupling capacitance is displayed.

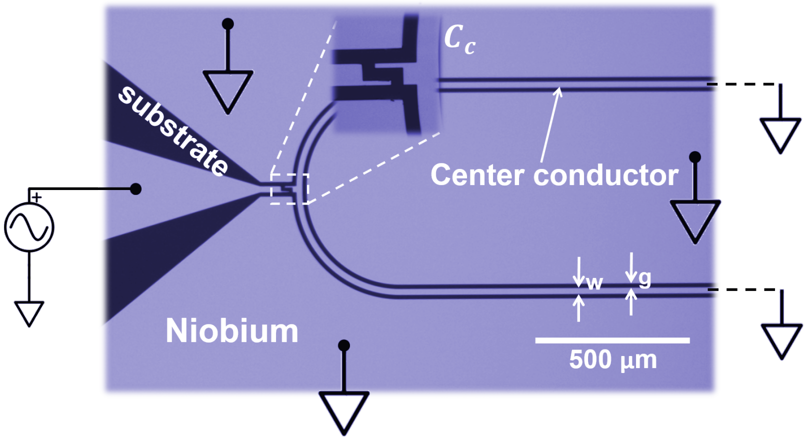

Figure 5.1: Optical image of a typical Niobium (false color) $\lambda/2$ CPW resonator, the dark regions represent the substrate. The finger coupling capacitance is shown in a zoom-in. w and g are respectively the center conductor width and its separation distance to the ground plane.

5.2 Microwave dielectric losses analysis

In this section both the power and the temperature dependence of the microwave dielectric losses is reported for the three different substrates employed. For temperatures below $T^* \simeq \frac{T_c}{10}$ ($T^* \approx 1$ K, for Nb), the microwave losses $1/Q_0$ are expected to be dominated by the dielectric losses $\tan\delta$. Therefore, the conductor losses from the superconductor can be included in a background term, containing also the radiation and other possible losses mechanisms. Dielectric losses $\tan\delta(T, P)$, instead, are given by the theoretical expression eq. (2.39) obtained from the TLS resonant absorption theory. Thence, one can generally

[1]A 200 nm thick Nb film, deposited on annealed substrates by magnetron sputtering in an ultra high vacuum environment, has been patterned by e-beam lithography and NF_3 reactive ion etching (RIE).

write:

$$\frac{1}{Q_0}(T,P) = \tan\delta(T,P) + \frac{1}{Q_b}, \tag{5.1}$$

here, the background term $\frac{1}{Q_b}$ is treated as a constant in the investigated temperature and power ranges. This is not valid for $T > T^*$, at which the conductor losses vary exponentially with temperature as expressed by Mattis-Bardeen theory (see section 2.4). Both the unloaded quality factor Q_0 and the fundamental resonance frequency f_0 have been extracted via the fit of the complex valued reflection signal S_{21} around f_0, using the following expression:

$$\Gamma = \frac{Q_{ext}^{-1} - Q_0^{-1} - 2i\delta x}{Q_{ext}^{-1} + Q_0^{-1} + 2i\delta x}, \tag{5.2}$$

where $\delta_x = \frac{f-f_0}{f_0}$ and Q_{ext} is the external quality factor associated to the coupling to the external environment (see section 2.4). In figure 5.2 the fit to Eq.(5.2) (green solid line) of the amplitude of the reflection signal for a typical Nb CPW resonator is displayed.

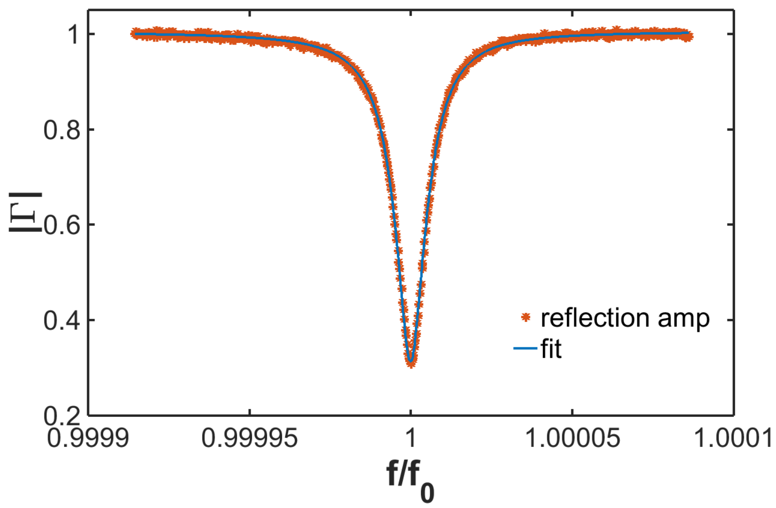

Figure 5.2: Amplitude of the reflection coefficient as a function of the normalized frequency. The blue solid line represents the fit to equation (5.2).

Power dependence at base temperature

In order to study the power dependence, the bath temperature is kept fixed at $T = 20$ mK and the input power is varied via an external attenuator (see section 3.3) down to a value corresponding to few photons on average inside the resonator. In figure 5.3 the microwave losses $\frac{1}{Q_0}$ are plotted as a function of the circulating power P_{cir}, defined by Eq.(2.38) and the average number of photons $N_{ph} = P_{cir}/hf_0^2$ in the resonator. The solid lines represent the best fit to eq.(2.39), for which the dielectric losses $F\alpha_{TLS}$, the critical power P_c' and the power exponent β are used as fitting parameters. Experimental data for both MgO and LSAT show a plateau for power below P_c' and a significant reduction of the microwave losses with increasing P_{cir}, as result of the progressive saturation of the TLS bath. At high power, when all the TLS bath is saturated, the unloaded quality factor value would be

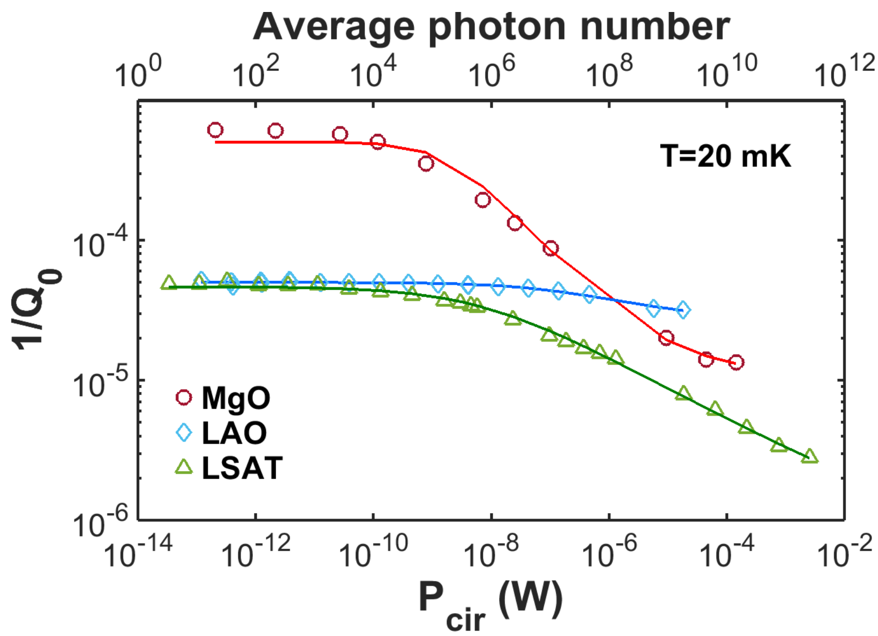

Figure 5.3: Microwave losses as a function of the circulating power P_{cir} (bottom axis) and the average number of photons (top axis) at $T = 20$ mK, for the three different studied substrates. The solid lines represent the best fitting to Eq.(2.39).

limited by the background term. However, due to limitations in the experimental setup, optimized for working at low power, a saturation of Q_0 at high power is not observed and it has not been possible to extract a value for $1/Q_b$. On the contrary, LAO data show only a weak variation as a function of the power, suggesting a larger contribution to the overall microwave losses from the conductor ones in the superconductor, for which no power dependence is expected. This could be due to the presence of defects at the surface of the Nb films grown on LAO, or at the interface with this specific substrate, resulting in a significant degradation of the microwave properties. The $F\alpha_{TLS}$ values for the different dielectrics, extracted from the fitting, are listed in table 5.1. In the same table the values obtained using sapphire as substrate are reported for comparison.

Substrate	MgO	LAO	LSAT	Sapphire
$\mathbf{Q_0}$	1.6×10^3	2×10^4	2.6×10^4	9.3×10^4
Coupling	under	critical	critical	over
$\mathbf{F\alpha_{TLS}}$ (5.1, 2.37)	3.3×10^{-4}	1.8×10^{-5}	3.4×10^{-5}	7.9×10^{-6}
$\mathbf{F\alpha_{TLS}}$ (5.3)	5.5×10^{-4}	N.A.	4.6×10^{-5}	4.8×10^{-6}
$\mathbf{F\alpha_{TLS}}$ (2.39)	4.9×10^{-4}	2.5×10^{-5}	4.6×10^{-5}	1.4×10^{-5}
$\mathbf{1/Q_b}$ (5.1, 2.37)	3.8×10^{-5}	3.1×10^{-5}	5.6×10^{-6}	3.6×10^{-6}
$\mathbf{\frac{F\alpha_{TLS}}{1/Q_b}}$ (5.1, 2.37)	8.7	0.6	6.1	2.2

Table 5.1: (Top part) Q_0 values and resonators coupling at $T = 20$ mK and in the low power limit. (Bottom part) $F\alpha_{TLS}$ and $1/Q_b$ values for the different dielectrics, extracted from fits to the equations indicated in parenthesis.

Temperature dependence in the low power limit

For the investigation of the temperature dependence, the input power is kept fixed below the critical value P_c, corresponding to few photons on average inside the resonator (low power limit). At this value of the input power, the microwave losses are power independent as shown by experimental data plotted in Fig. 5.3. The reflection signal S_{21} has been measured varying the mixing chamber temperature up to the critical temperature of the Nb film ($T_c \approx 9$ K), and the unloaded quality factor Q_0 has been extracted from the fit to Eq.(5.2). Figure 5.4 shows the microwave losses $1/Q_0$ for the three studied dielectric materials as a function of the temperature in the millikelvin range, where conductor losses are expected to be constant. The solid lines represent the best fit to Eq.(5.1) and Eq.(2.37) for $P \ll P_c$, from which the ultimate intrinsic dielectric losses $F\alpha_{TLS}$ and the background term $1/Q_b$ are used as fitting parameters. The arrows point to the value of $1/Q_b$ obtained for each substrate. Both MgO and LSAT show a strong temperature dependence with

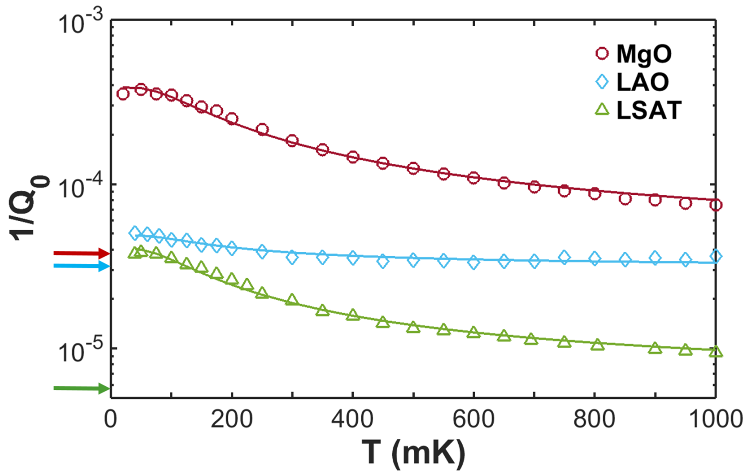

Figure 5.4: Microwave losses as a function of the temperature in the millikelvin range, at input power below the critical value, for the three different studied substrates. The solid lines represent the best fit to Eq.(5.1) and Eq.(2.37).

a significant reduction of the microwave losses with increasing the bath temperature. The experimental data are very well represented by the TLS resonant absorption theory. Indeed, the large value of the product $F\alpha_{TLS}Q_b > 1$ (see table 5.1) for these two substrates clearly indicates that the overall microwave losses are dominated by the TLS resonant absorption mechanism in the dielectric. The value obtained for the background term $1/Q_b$ is, most probably, associated to the onset of microwave losses due to the relaxation absorption process[78], taking place at higher temperature. On the other hand $1/Q_0$ from the resonator patterned on LAO is characterized by a weak temperature dependence, with a small value for the product $F\alpha_{TLS}Q_b < 1$ (see table 5.1). The large extracted value $1/Q_b \approx 3.1 \times 10^{-5}$ suggests that the background contributions are the dominating losses mechanisms for this specific device. Specifically, the large background term could be due to high conductor losses caused by inhomogeneities in the Nb film. These inhomogeneities could be induced by the well reported presence of twin domains in LAO substrates, but a detailed microscopic analysis is needed for more accurate conclusions.

The resonator fundamental resonance frequency f_0 in the low power limit ($P < P_c$) is also temperature dependent. Starting from eq.(2.37), neglecting the power dependence and using the *Kramers-Kronig* equations, one obtains an expression for the resonance frequency shift δf_0, defined as: $\delta f_0(T) = \frac{f_0(T) - f_0(T_0)}{f_0(T_0)}$, which writes as[104]:

$$\delta f_0(T) = \frac{F\alpha_{TLS}}{\pi} \left\{ \ln\left(\frac{T}{T_0}\right) - [g(T, f_0) - g(T_0, f_0)] \right\}, \tag{5.3}$$

where $g(T, f) = Re[\Psi(1/2 + hf/2\pi i k_B T)]$, Ψ is the complex digamma function and T_0 is a reference temperature. The digamma function is significant only for temperatures such that $k_B T \leq hf_0/2$ and it results in an upward turn below $T = hf_0/2k_B$. In our specific case ($f_0 \approx 5$ GHz), this temperature corresponds to $T \simeq 120$ mK which has been set as reference temperature T_0 for the presented data. Equation (5.3) accounts only for dielectric losses from resonant absorption by TLS. Therefore, the intrinsic microwave dielectric losses $F\alpha_{TLS}$ can be also extracted from the temperature dependence of δf_0, and used to discriminate among the possible different mechanisms. In figure 5.5 the temperature dependence of the resonance frequency shift is shown for all the investigated dielectrics. The solid lines represent the fit to eq.(5.3). Once again the behavior observed

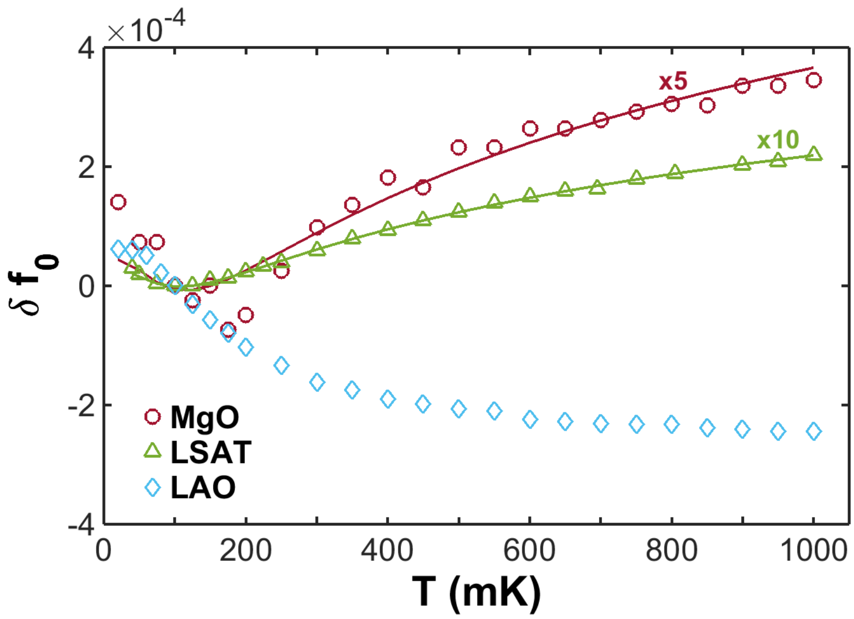

Figure 5.5: Resonance frequency variation δf_0 as a function of the temperature in the millikelvin range, at input power below the critical value, for the three different studied substrates. The solid lines represent the best fit to eq.(5.3). The data for MgO and LSAT have been multiplied respectively by a factor 5 and 10 for a clear visualization.

for the device patterned on LAO substrate differs from the one of MgO and LSAT. In fact, MgO and LSAT show the expected trend for δf_0, and the experimental data are in a very good agreement with the TLS theory. Moreover, the $F\alpha_{TLS}$ values extracted are consistent with those obtained from the power and the temperature dependencies of $1/Q_0$ (see table 5.1 for a numerical comparison). LAO, instead, shows a monotonic decrease of

δf_0 with temperature, which resembles the temperature dependence of an effective kinetic inductance[160], and does not allow for any determination of $F\alpha_{TLS}$ for this substrate. This confirms, once more, that a mechanism different than resonant absorption from TLS is the main responsible for microwave losses of Nb resonators on LAO.

In summary, dielectric losses in MgO and LSAT are very well represented by the TLS resonant absorption theory, whereas this is not the case for LAO. The microwave losses in Nb resonators patterned on LAO are, in fact, dominated by a background contribution. This has been identified as conductor losses from the Nb film. The microwave proprieties of Nb films grown on LAO might be degraded by the presence of defects and inhomogeneities induced by the presence of twin domains in this dielectric material. Nevertheless, the experimental data presented here strongly indicate LSAT as the ideal substrate to be employed for YBCO microwave devices. First, among the studied substrates, it is the one characterized by the lowest value of the intrinsic dielectric losses at low power and millikelvin temperature $F\alpha_{TLS}$. Moreover, since these losses are very well modeled by TLS resonant absorption, one can use this information for a proper design optimization of microwave devices aiming at the minimization of the TLS contribution, which is geometry dependent as discussed in section 2.4.

5.3 Microwave losses in YBCO films on LSAT/CeO_2

In the previous section LSAT has been identified as the best substrate, among the different dielectric materials compatible with epitaxial growth of YBCO, for microwave devices operated in the single photon limit. However, for the realization of a YBCO transmon qubit, proper Josephson junctions are needed. Macroscopic quantum tunnelling and energy level quantization have been recently observed in YBCO bi-epitaxial grain boundary junctions[22, 23], which therefore represent an ideal choice to implement for quantum devices as the transmon. However, bi-epitaxial GB junctions require an additional dielectric layer (see section 3.2). A possibility is to use LSAT in combination with a CeO_2 film acting as the seed layer. The understanding of the microwave losses, at millikelvin temperature and at low input power, from YBCO resonators patterned on LSAT substrate covered by a CeO_2 seed layer is therefore necessary. In this section, a characterization of YBCO resonators in the single photon limit is presented in comparison to a Nb device realized on the same combination of dielectrics.

In figure 5.6 the microwave losses $1/Q_0$, extracted from the measurement of reflection signal from YBCO CPW resonator patterned on top of LSAT/CeO_2 bilayer, are plotted as a function of the average number of photons in the device. The experimental data from the analogous resonator made of Nb is shown for comparison. While the Nb resonator shows a weak power dependence, the YBCO one is power independent in the investigated range. The temperature dependence is, thence, studied at powers corresponding to an average number of photons $N_{ph} < 1000$ (low power limit), which ensures no power dependence for both devices. Figure 5.7 shows the experimental values of the microwave losses versus temperature, in the millikelvin range and in the low power limit, for both a YBCO (orange triangles) and Nb (violet circles) resonator. The solid lines represent the fit to Eq.(5.1) and Eq.(2.37) used in the low power limit $P \ll P_c$, i.e. neglecting the power dependence. For both the devices the microwave losses $1/Q_0$ monotonically decrease with increasing the temperature, in a very good agreement with the TLS resonant absorption theory.

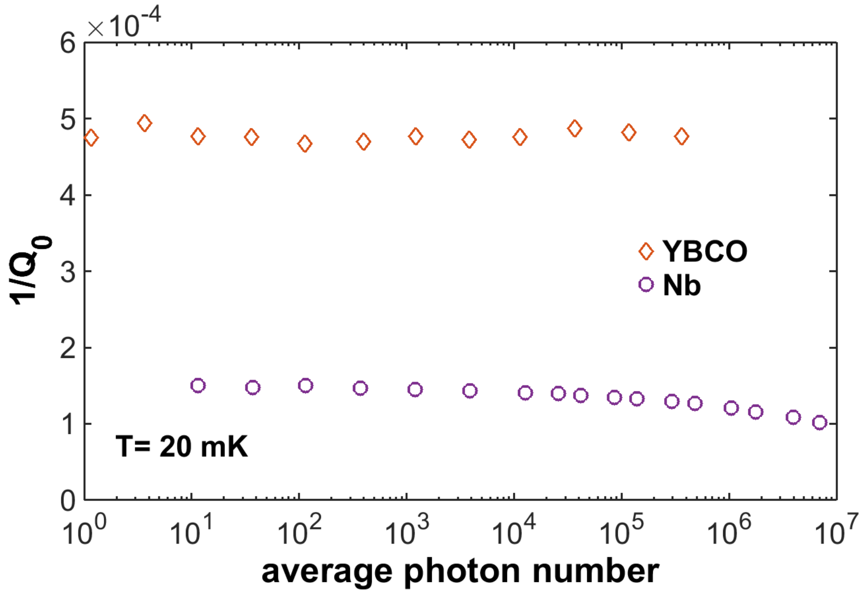

Figure 5.6: Microwave losses versus average photon number at $T = 20$ mK for YBCO (orange diamonds) and Nb (violet circles) resonators patterned on a LSAT/CeO_2 bilayer.

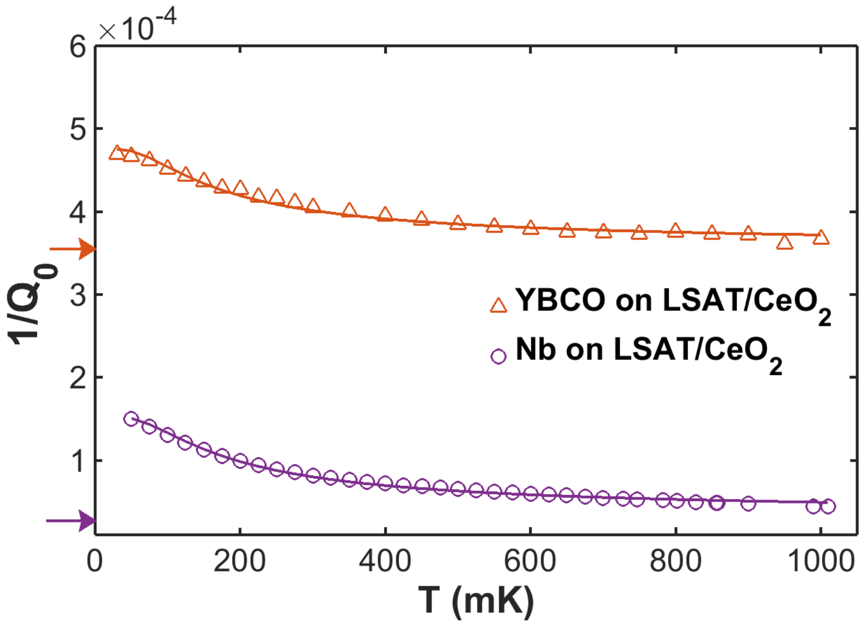

Figure 5.7: Microwave losses as a function of the temperature, in the low power limit and in the millikelvin range, for YBCO (orange triangles) and Nb (violet circles) CPW resonators patterned on a LSAT/CeO_2 bilayer. The solid lines represent the best fit to Eq.(5.1) and Eq.(2.37). The arrows point to the values of the background term $1/Q_b$ extracted from the fit.

The values for the intrinsic dielectric losses $F\alpha_{TLS} = 1.17 \times 10^{-4}$ extracted from the fitting coincide for the two resonators (see table 5.2), and it is roughly 3 times larger than the one obtained from Nb CPW resonators patterned on bare LSAT substrates (see table 5.1). This increase in the dielectric losses in the single photon limit, thence, has to be attributed to the additional CeO_2 seed layer. While the same values for $F\alpha_{TLS}$ have been extracted from the measurement of the two devices, the background terms differ by about an order of magnitude (see table 5.2). In particular, the YBCO resonator shows a $1/Q_b$ term approximately 3 times larger than the dielectric losses $F\alpha_{TLS}$. The radiation losses for the geometry used for the studied devices are expected to be much smaller ($\ll 10^{-5}$)[103], therefore the large value for $1/Q_b$ is attributed to conductor losses in YBCO. Using a value for the London penetration depth $\lambda_L \approx 200$ nm together with the value extracted for Q_b, a surface resistance $R_s \approx 70\,\mu\Omega$ is obtained. This value is a good agreement with those reported in literature for YBCO thin films at low temperature and at frequencies around 5 GHz[109].

Device	$\mathbf{f_0}$ (GHz)	$\mathbf{Q_{ext}}$	$\mathbf{F\alpha_{TLS}}$	$\mathbf{1/Q_b}$
YBCO	4.78	5.7×10^4	1.17×10^{-4}	3.5×10^{-4}
Nb	5.02	4.4×10^4	1.17×10^{-4}	3.4×10^{-5}

Table 5.2: Fundamental resonance frequency f_0 and coupling quality factor Q_{ext} for the two investigated resonators. $F\alpha_{TLS}$ and $1/Q_b$ values extracted from the fit to Eq.(5.1) and Eq.(2.37) in the limit $P \ll P_c$ are also reported.

Despite the larger conductor losses compared to Nb, the realization of a YBCO transmon qubit is still possible. In fact, an unloaded quality factor $Q_0 \approx 2000$ in the single photon limit at $f_0 \approx 5$ GHz for the YBCO resonator on the LSAT/CeO_2 bilayer results in a decay rate $\kappa = f_0/Q_0 \approx 2.5$ MHz. Such a value, compared to typical coupling strength of a transmon qubit $g \approx 100$ MHz, is low enough to ensure a strong coupling between the qubit and the resonator. This is a fundamental prerequisite for the realization and the operation of a YBCO transmon qubit.

As discussed in section 3.2, the YBCO grain boundary junctions employed in the transmon device make use of (103)-oriented YBCO. In particular one of the shunt capacitor plates and half of the junction electrodes consist of (103)-oriented YBCO (see Fig.3.2). It is therefore necessary to make sure that the value of R_s, representative of the microwave properties of the (103)YBCO film, is such that it does not result in too large dissipation. A value of the surface resistance $R_s \simeq 1$ mΩ has been estimated from the unloaded quality factor $Q_0 \simeq 500$ of a $\lambda/2$ CPW resonator patterned on the (103)YBCO film, assuming an effective London penetration depth $\lambda_{eff} \simeq 1\,\mu$m. The Q_0 value has been extracted from the fitting to Eq.(5.2) of the reflection signal measured at $T = 20$ mK and at very low input power. The contribution of the (103)YBCO structures on the overall transmon quality factor can be accounted for by representing them as an equivalent resistor R_{103} in series to the junctions and the shunting capacitance. Given the geometry and the size of the (103)YBCO electrodes, the total equivalent resistance can be calculated by considering ≈ 25 squares in series. Taking the value of the (103)YBCO surface resistance at 5 GHz, a total equivalent resistance $R_{103} \simeq 25$ mΩ is obtained. The quality factor of the equivalent circuit including R_{103} is $Q_{103} = 2\pi f_0 \frac{L_J}{R_{103}} \simeq 12500$, where $L_J = \frac{\Phi_0}{2\pi I_c} \simeq 10$ nH is the minimum junction inductance (see Eq.(2.5)) at $I_c = 30$ nA and $f_0 = 5$ GHz. Indeed, the (103)YBCO electrodes do not represent the limiting dissipation source.

In conclusion, the results presented in this section assess the feasibility of a YBCO transmon qubit based on bi-epitaxial nanosized Josephson junctions fabricated on LSAT covered by a CeO_2 seed layer.

Chapter 6

Characterization of an all-YBCO transmon quantum bit

In this chapter the results from the characterization of an all-YBCO transmon qubit are discussed and analyzed. After a brief introduction about the motivation behind the presented studies, the results from transmission measurement through the resonator-qubit system showing vacuum Rabi splitting are reported. A more quantitative analysis of the device decoherence rate is obtained from spectroscopic measurements and a comparison with quality factors expected from measured I_cR_N products of the employed Josephson junctions is made. Finally, the observation of a significant improvement of the transmon coherence time, at externally applied magnetic field up to 9 Tesla, is discussed.

6.1 Motivations and design

In the previous chapter 5, the feasibility of a YBCO transmon quantum bit has been demonstrated. Quantum coherence time from an all-YBCO qubit is expected to be limited by the presence of nodal quasiparticles and midgap states, both being a direct consequence of the $d-$wave symmetry (d) of the superconducting order parameter. The presence of an imaginary subdominant $s-$wave component (is), creating a fully gapped superconducting state ($d + is$), would result in a significant improvement of the transmon coherence. In fact, with a fully gapped superconducting state, nodal qusiparticles are eliminated and MGS are shifted far from the Fermi energy and thence they do not contribute to decoherence (see section 2.5.3). Therefore, in this respect, a YBCO transmon can be used as a very sensitive spectrometer with a very high energy resolution to probe the quasiparticle spectrum by monitoring the relaxation time of the qubit. In particular, it allows for doing spectroscopy at energy scales corresponding to its characteristic frequency f_a. In the specific, a transmon frequency $f_a \simeq 5$ GHz corresponds to an energy $\simeq 20\,\mu$eV. Such value is of the same order of magnitude as the subdominat energy gap recently measured experimentally in a nanometer sized YBCO island, used for the realization of a YBCO single electron transistor[24].

The YBCO transmon qubit devices presented in this thesis work are fabricated employing bi-epitaxial garin boundary Josephson junctions (see section 3.2). Macroscopic quantum behaviour from this specific GB JJs has been experimentally observed and re-

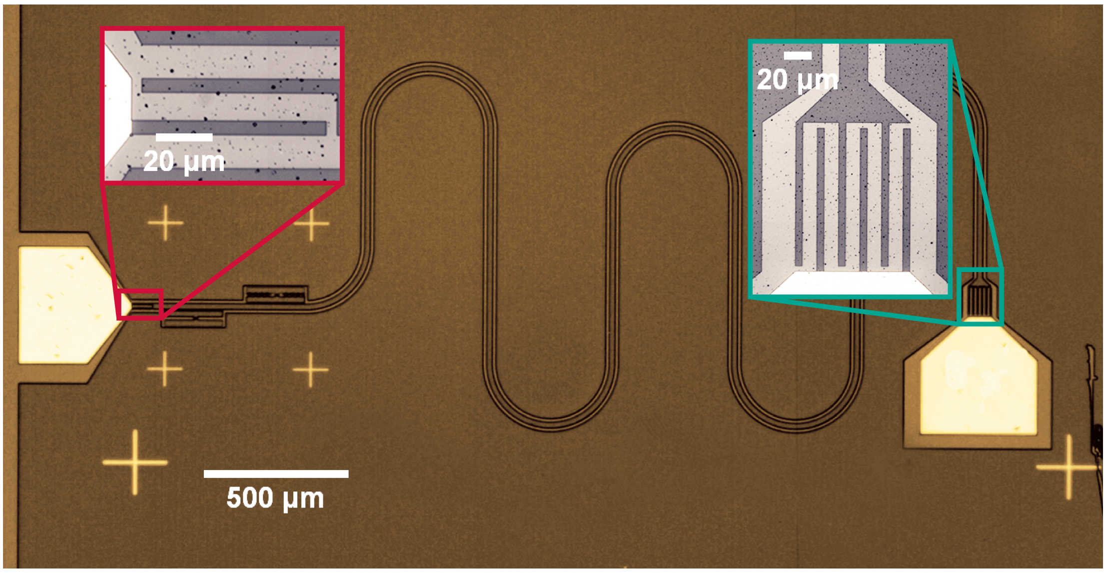

Figure 6.1: Optical image of the full device in false colors. The insets show zoom-in of both the input C_{c1} and the output C_{c2} coupling finger capacitance.

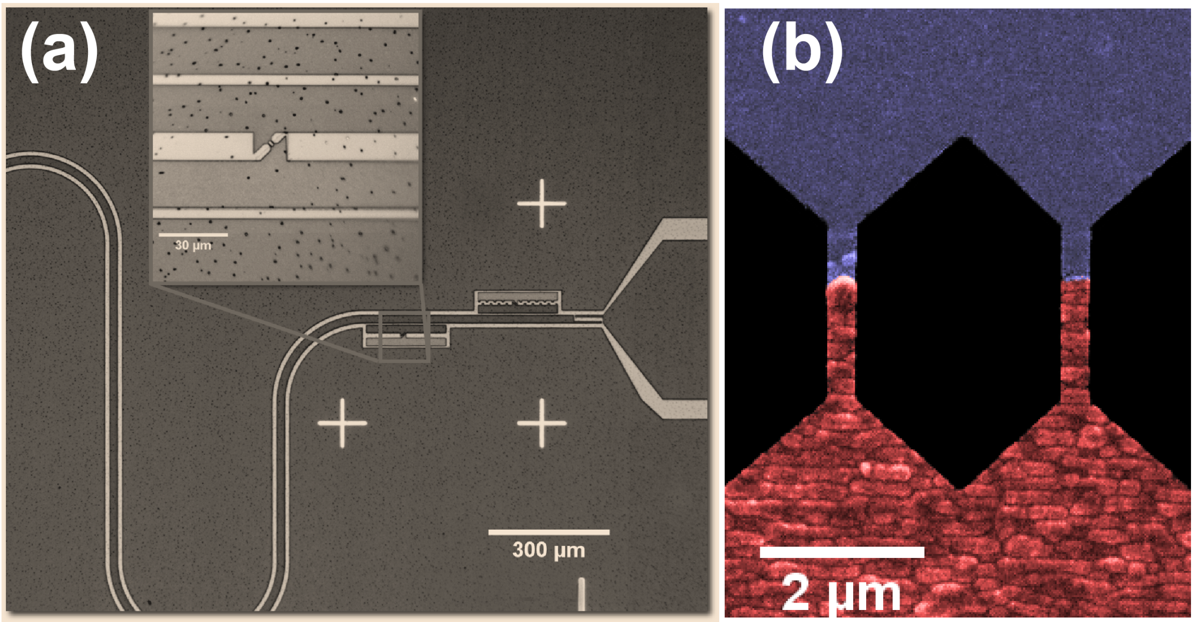

Figure 6.2: (a) Optical image showing a typical YBCO transmon-CPW resonator device. The zoom-in shows the details of the transmon layout, including the two planar capacitor plates and the two grain boundary junctions forming a SQUID loop. Here the two junctions are patterned with a nominal 45° grain boundary angle α. (b) Scanning electron microscope image of two typical YBCO grain boundary junctions (false color). The junction barrier is formed at the interface between the c-axis oriented (violet region) and the (103) oriented YBCO (red region). Here the junctions are patterned with a nominal $\alpha = 0°$.

ported in ref.[22, 23]. Three different nominal GB angles $\alpha = 0°$, 45° and 90° have been used (see figure 2.6). However, due to roughness and faceting along the GB line, the actual α angle is not well defined as it can be seen from Fig.6.2(b). Therefore, the junctions' transport properties are the result of an averaging over different angles and an accurate angular dependence can not be studied yet. For the realization of the YBCO transmon devices, two JJs, designed in a SQUID loop configuration (see Fig.6.2(b)), are employed and shunted by a large capacitance made out of two (200*20 μm^2) plates (see inset in Fig.6.2(a)). The transmon is embedded at one end (voltage antinode) of a $\lambda/2$ CPW (see Fig.6.1 and 6.2(a)). The CPW resonator is designed to have a fundamental resonance frequency $f_0 \simeq 5$ GHz (see section 3.1). More specifically, two transmons, characterized by a different SQUID loop area and different shunting capacitances, have been fabricated for a single CPW resonator. The latter is capacitively coupled to the input and the output microwave lines via finger capacitances C_{c1} and $C_{c2} > C_{c1}$, respectively (see Fig.6.1 and section 3.1 for more details). The devices are mounted in a rf-tight copper box and thermally anchored at the mixing chamber of a dilution refrigerator ($T \simeq 20$ mK). The measurement setup, described in section 3.3, has been used for the characterization of the YBCO transmon devices.

6.2 Transmission and spectroscopy results

Transmission measurements

The simplest way to detect a transmon qubit consists in measuring the transmission signal through the qubit-resonator system while tuning the qubit transition frequency f_a close to the $\lambda/2$ cavity fundamental mode f_0 by means of an externally applied magnetic flux Φ_e. The same measurement also allows for the estimation of the coupling strength g between the qubit and the resonator electromagnetic mode when the qubit and the resonator are on resonance (see section 2.5.1). When a two-level system is coupled to an electromagnetic mode, the coupled system is described by the Jaynes-Cummings (JC) Hamiltonian (see Eq. (2.55)). As discussed in section 2.5.1, different behaviours are expected depending on the detuning $\Delta_0 = |f_a - f_0|$. The detuning can be varied by sweeping the external magnetic flux. By sweeping Φ_e, in fact, the critical current I_c of the SQUID modulates periodically in multiples of the flux quantum Φ_0. Consequently, the transmon transition frequency f_a modulates with the same periodicity, resulting in a change of the Δ_0 value. In figure 6.3, the amplitude of the transmission signal through the transmon-resonator system, as a function of the external flux Φ_e in units of the flux quantum Φ_0 and the probing frequency f_{rf}, is shown for two different investigated devices. Here the amplitude is plotted in a color scale, such that red means high and blue low amplitude. At external magnetic flux corresponding to integer multiples n of the flux quantum $\Phi_e = n\Phi_0$, the transmon is at the maximum detuning from the resonator fundamental resonance ($\Delta_0 > g_{01}$), and only a single peak of the transmission signal is observed in the measurement frequency range. The peak is centred around f_0 and is characterized by a linewidth Δf_0 mainly representative of the bare resonator. Specifically, the data from device 1, displayed in Fig. 6.3(a), show a $\Delta f_0 \simeq 25$ MHz, corresponding to a $Q_L \simeq 200$, in close agreement with the estimation of the design parameters (see section 3.1). When qubit and cavity are close to resonance, as it is the case for the data from device 2 (figure 6.3(b)), the coupled qubit-cavity system states are given by a superposition of qubit and photon number states (see section 2.5.1). At zero detuning $\Delta_0 = 0$, the qubit and the resonator are on resonance.

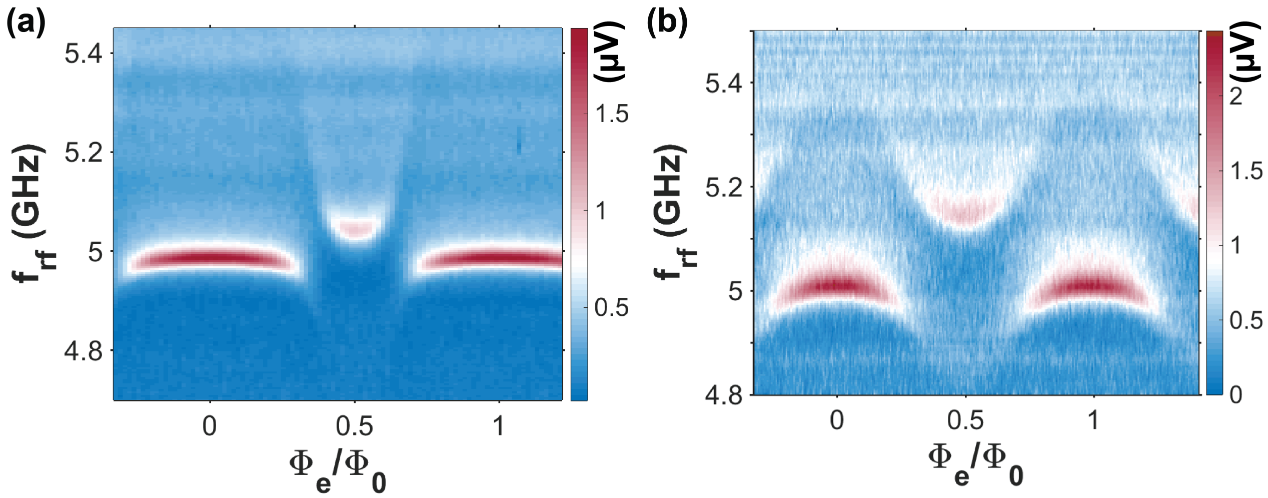

Figure 6.3: Amplitude of the transmission signal through the qubit-resonator system, for device 1 (a) and device 2 (b), as a function of the probe frequency f_{rf} and of the external magnetic flux Φ_e, expressed in units of the flux quantum Φ_e. Both devices have been realized with a nominal $\alpha = 45°$.

At resonance, the eigenstates of the total coupled system are known as *dressed states* (see section 2.5.2). The coupling lifts the degeneracy between the $|0\rangle\,|n=1\rangle$ and the $|1\rangle\,|n=0\rangle$ states and as a consequence two transmission peaks are observed. This phenomenon is known as *vacuum Rabi splitting*. The minimum separation in frequency between the two peaks is a measurement of the coupling strength g_{01}. In order to get an estimate of g_{01}, the transmission measurement for device 2 has been repeated in a narrower range of magnetic flux, with a higher frequency resolution and more averaging. The obtained data are displayed in figure 6.4(a), where the amplitude of the transmission signal is plotted as a function of the probe frequency f_{rf} and Φ_e in units of Φ_0. The red dashed line indicates the position at which a linecut is taken. The linecut is shown in figure 6.4(b), where the amplitude of the transmission signal is plotted versus the probe frequency. From figure 6.4(b) a coupling $g_{01} \simeq 140$ MHz has been estimated. A quantitative estimation of the transmon decoherence rate has been obtained from measurements of the spectroscopic linewidth Δf of the qubit $0 \to 1$ transition, with qubit and cavity off resonance, as reported in the next paragraph.

Spectroscopy measurements

The transmon qubit can be detected by dispersive read-out even when it is far detuned from the resonator $\Delta_0 \gg g_{01}$. The measurement consists in probing the resonator with a microwave signal at frequency around f_0, and at the same time a second tone is swept in a wide range of frequency f_1 (see schematic of the measurement setup in figure 3.6). At $f_1 \simeq f_a$, the first excited state of the qubit gets populated and therefore the resonator frequency is dispersively shifted by a factor $\chi \simeq -g_{01}^2 E_c/[\Delta_0(\Delta_0 - E_C)]$, as described in section 2.5.2, and a change in the amplitude and phase of the transmission signal is observed. Figure 6.5 displays the phase of the transmission signal as a function of the

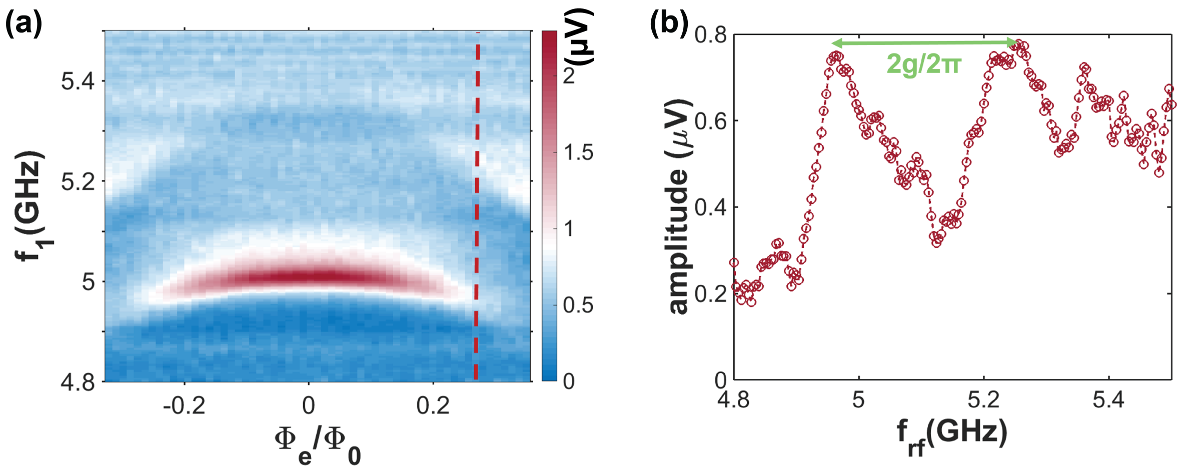

Figure 6.4: (a) Amplitude of the transmission signal versus the probe frequency and the external magnetic flux in units of the flux quantum Φ_0, for device 2. As compared to Fig.6.3, here the data are taken with a higher frequency resolution and more averaging. The dashed red line indicates the position at which the linecut, shown in (b), is taken. (b) Amplitude of the transmission signal versus the probe frequency, at a fixed Φ_e.

second tone frequency f_1 and of the externally applied magnetic flux Φ_e, in units of the flux quantum Φ_0, of a typical investigated device (device 3).

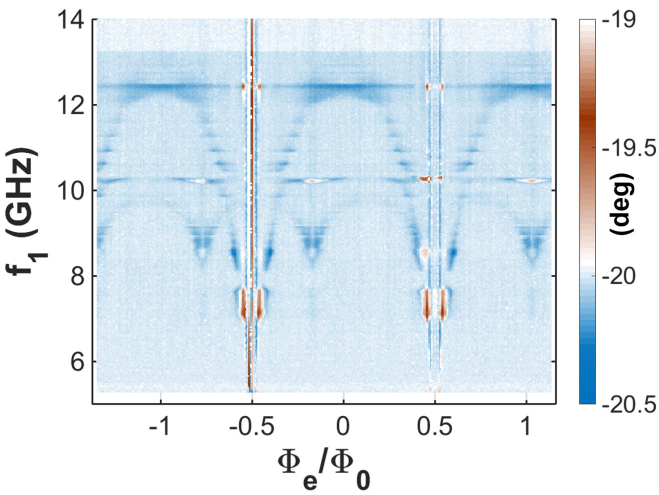

Figure 6.5: Phase of the transmission signal, measured at the resonator frequency $f_0 \simeq 5.1$ GHz, as a function of the second tone frequency f_1 and of the external magnetic flux Φ_e, for device 3. The two transmons, characterized by different transition frequency and different periodicity, are observed.

One can clearly observe a periodic SQUID modulation of the transmon frequency as a function of Φ_e, as expected from the magnetic flux dependent Josephson energy E_J. In particular, both the transmon qubits embedded in the resonator are detected up to frequencies around 13 GHz. The two transmons differ in periodicity, total critical current

I_c and junctions asymmetry.

In figure 6.6(a) the amplitude of the transmission signal, measured at the resonator frequency $f_0 \simeq 5.1$ GHz, from device 1 is plotted as a function of the second tone frequency f_1 and of the magnetic flux Φ_e. The dashed red line indicates the position at which the linecut shown in figure 6.6(b) is taken. By taking a linecut at a fixed magnetic flux, it is possible to extract the linewidth Δf as the full width at half depth/height of the signal dip/peak. Here a $\Delta f \simeq 180$ MHz is extracted. This represents a typical value for the investigated YBCO transmon qubit devices.

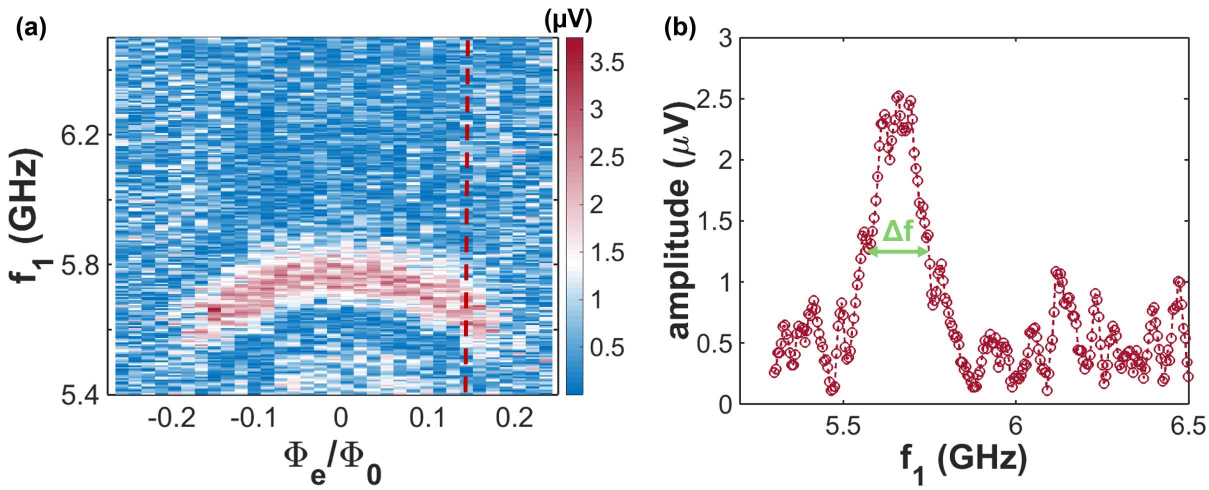

Figure 6.6: (a) Amplitude of the transmission signal versus the external magnetic flux Φ_e and the second tone frequency f_1, for device 1. The dashed red line indicates the position at which the linecut, shown in (b), is taken. (b) Transmission amplitude versus f_1. The linewidth Δf is extracted as the full width at half height of the signal peak.

Various different dissipation and dephasing sources contribute to the transmon decoherence rate and result in the observed Δf (see section 2.5.1). In the specific case of YBCO the main expected sources are: low frequency critical current fluctuations[120, 86], nodal quasiparticles, the presence of midgap states (see section 2.2), a resistive shunt in the GB barrier due either to the presence of localized quasiparticles states (intrinsically shunted junctions) or to a non-homogeneous barrier with normal transport channels characterized by very low values of the I_cR_N product. Attempts to directly measure relaxation time were limited by the ring up time of the resonator. This sets an upper limit for the transmon relaxation time $T_1 < 50$ ns. In order to discriminate among the above mentioned different decoherence sources, a study of the transmon coherence time extracted from the spectroscopic width in the presence of a high magnetic field has been done. Moreover a comparison to the DC characterization of the employed junctions is made. Both are reported in the next sections.

6.3 Coherence at high in-plane magnetic field

The dominant superconducting order parameter of YBCO has a $d-$wave symmetry (see section 1.3.1). However, a subdominat imaginary $s-$wave component (is) has been both experimentally observed[24] and theoretically predicted in ref.[51, 161] and references therein. Moreover, its weight is expected to be enhanced by applying a high magnetic field along the GB interface, such that states are shifted away from zero energy by the induced screening currents. The presence of a is component results in a fully gapped superconducting state, which can have strong consequences on the transmon decoherence rate. In fact, both nodal quasiparticles and MGS, which are a direct consequence of the $d-$wave symmetry of the order parameter and two of the main dissipation sources limiting the coherence time of a YBCO transmon[119] (see section 2.5.3), are expected to be affected. Indeed, the presence of the imaginary $s-$wave component would result in a significant improvement of the transmon coherence time. In order to detect the presence of the is component, spectroscopy measurements of a YBCO transmon device have been performed in presence of a high in-plane magnetic field $B_{\|}$. An in-plane magnetic field $B_{\|}$ minimizes vortex trapping and at the same time has a component along the GB interface due to the 45 slanted GB that have been used for the presented devices (see section 2.1.3). In figure 6.7 the data from spectroscopy measurements at two different values of the $B_{\|}$ are shown.

In figure 6.7(a) and (c) the amplitude of the transmission signal is plotted as function of the external magnetic flux Φ_e and of the second tone frequency f_1, respectively for the measurement at $B_{\|} = 300$ mT and $B_{\|} = 2$ T. The data at all the different $B_{\|}$ values show a periodic SQUID modulation. In Fig.6.7(a) and (c), the solid white line represent the transmon frequencies as calculated by keeping fixed the charging energy ($E_c \simeq 260$ MHz) and adjusting both the total SQUID critical current $I_c \simeq 25$ nA and the junctions asymmetry ($d = \frac{I_{c2}-I_{c1}}{I_{c2}+I_{c1}} \simeq 0.9$). The dashed green lines, instead, indicate the position at which the linecuts shown in figure 6.7(b) and (d), respectively for the data measured at $B_{\|} = 300$ mT and $B_{\|} = 2$ T, are taken. The linewidth are extracted from the fit to one or two Lorentzian curves, displayed by the solid green lines in the figures. Figure 6.8 shows the linecuts obtained respectively at $B_{\|} = 3$ T (a) and $B_{\|} = 9$ T (b), where the solid red lines represent the best fit to a Lorentzian line shape. The obtained Δf values are plotted versus the applied $B_{\|}$ field and shown in figure 6.9 (open violet circles).

Moreover, the values f_a, at which the reported linewidth are extracted, are plotted in the top panel of figure 6.9 as a function of $B_{\|}$. The variation of f_a as a function of the applied magnetic field is the result of random vortex trapping close to the GB junctions, affecting the critical current of the individual JJs. For magnetic field values $B_{\|} \leq 2$T the detuning Δ_0 is in the range of 2-3 times the coupling g_{01}. Therefore, the states probed at $B_{\|} \leq 2$T are still considerable mixtures of qubit and resonator states, whereas for $B_{\|} > 2$T, the detuning Δ_0 is large enough that the probed states are more of qubit nature. An estimate of the bare qubit decoherence rate γ can be obtained by using the following expression for the Δ_0-dependent decoherence rate of the qubit interacting with the cavity γ'[162]:

$$\gamma' = [1 - z^2]\gamma + z^2\kappa, \tag{6.1}$$

where κ is the CPW resonator decay rate. For large detuning $\Delta_0 \gg g_{01}$, $z \simeq (g_{01}/\Delta_0)$ represents a good approximation[162]. In the case of small detuning, instead, the exact

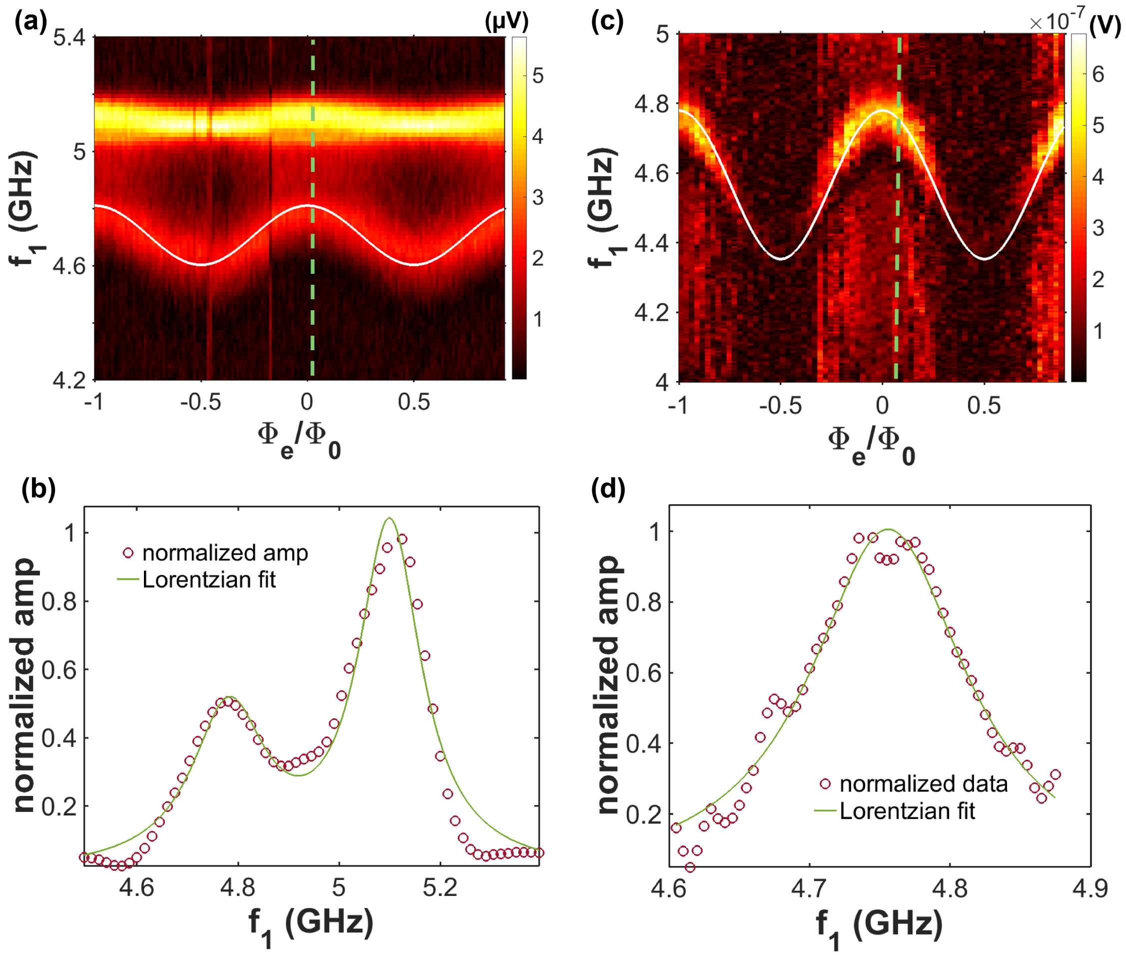

Figure 6.7: Spectroscopy measurements in presence of an in-plane magnetic field $B_\parallel$. (a) Amplitude of the transmission signal as a function of the second tone frequency f_1 and of the external magnetic flux Φ_e, measured at $B_\parallel = 300$ mT. The bright signal around 5.1 GHz corresponds to the resonator. The white solid line represents the transmon frequency as calculated by keeping fixed the charging energy E_c and adjusting the total critical current value $I_c = 25$ nA and the junctions asymmetry $d = \frac{I_{c1}-I_{c2}}{I_{c1}+I_{c2}} = 0.9$. The green dashed line indicates the position at which the linecut, shown in (b), is taken. (b) Normalized amplitude signal as a function of f_1. The transmon linewidth is extracted from to fit to two Lorentzian curves. (c) and (d) are the equivalent figures at $B_\parallel = 2$ T. The white solid line in (c) is obtained with $I_c \simeq 25$ and $d \simeq 0.8$.

expression has to be used[163]:

$$z = \left|\sqrt{n}\sin\theta_n\cos\theta_{n-1} - \sqrt{n-1}\sin\theta_{n-1}\cos\theta_n\right|, \tag{6.2}$$

where $\theta_n = \frac{1}{2}\arctan\left(\frac{2g\sqrt{n}}{\Delta_0}\right)$. The γ values calculated from Eq.(6.1) and Eq.(6.2), setting $n = 1$, $\gamma' = \Delta f$ and $\kappa = 20$ MHz, are also displayed in figure 6.9 (orange diamonds). The observed decrease of γ with increasing $B_\parallel$ indicates a significant increase of the transmon coherence time. This result is compatible with the occurence of a subdominant imaginary $s-$wave component in the superconducting order parameter. The improvement of the coherence time could be associated to a progressive enhancement of the weight of the

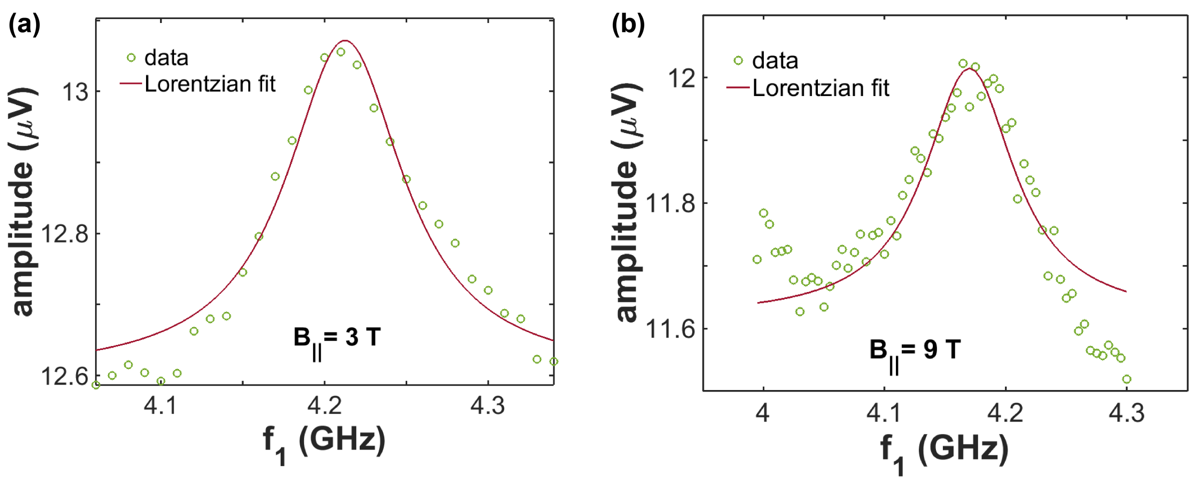

Figure 6.8: Amplitude of the transmission signal as function of f_1 from spectroscopy measurement at $B_{||} = 3$ T (a) and $B_{||} = 9$ T (b). The red solid lines are Lorentzian fit.

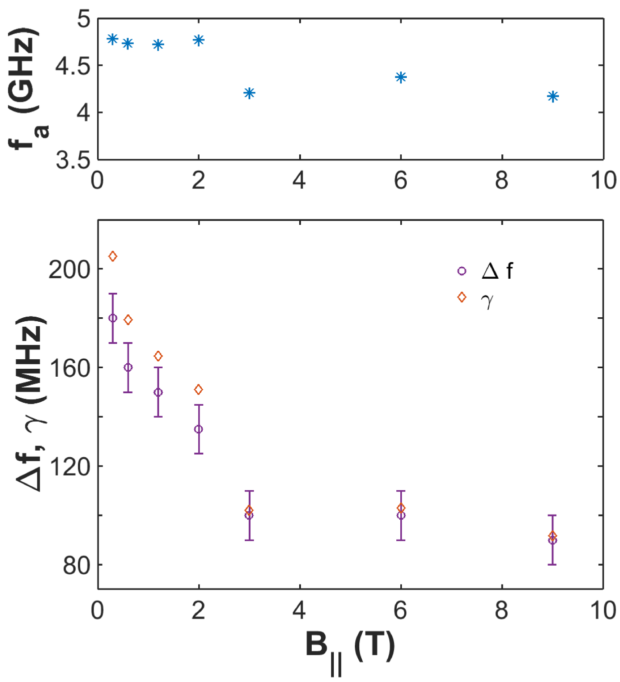

Figure 6.9: Transmon frequency f_a (top panel) and linewidth Δf (open violet circle, bottom panel) as a function of the in-plane field $B_{||}$. The transmon dacay rate γ, as calculated from Eq.(6.1) and Eq.(6.2), is also plotted versus $B_{||}$ (orange diamonds, bottom panel).

is component and opening of a fully developed gap in the quasiparticle spectrum[119]. However, γ saturates for $B_{||}$ above 3 T, suggesting the presence of an additional intrinsic source of decoherence independent of $B_{||}$. In order to provide insights regarding the nature of this other decoherence source, the DC current-voltage characteristics and the noise voltage properties of the junctions employed for the realization of the transmon devices have been investigated. Results from such studies are presented in the next section.

6.4 Transmon coherence from I-V characteristics

The two additional main candidates as possible decoherence sources are: low frequency critical current fluctuations, responsible of dephasing processes (see section 2.5.1), and the presence of a resistive shunting in the grain boundary barrier. In this respect, the study of the DC current-voltage characteristics and of the noise properties of the junctions, used for the realization of the all-YBCO transmon devices, delivers insights to discriminate among the different sources.

Modelling the transmon as an RLC parallel circuit (see inset in Fig.6.10(b)), where the dissipative sources is represented by a frequency dependent effective resistance $R_{eff}(\omega_a)$, its quality factor can be written as:

$$Q_a = \omega_a R_{eff}(\omega_a) C_\Sigma. \tag{6.3}$$

Here C_Σ is the total transmon capacitance. For ideal SIS tunnel junctions at $T \ll T_c$, the subgap resistance below 2Δ is exponentially larger than the normal resistance R_N, as a result of the exponentially reduced number of quasiparticles N_{qp} predicted by BCS theory. In this case, the subgap resistance represents a good approximation for R_{eff}. In SNS junctions, instead, the minigap plays a similar role as the superconducting gap Δ for the quasiparticles and it provides low dissipation (high R_{eff})[164, 165]. For YBCO, and in general for cuprates, the grain boundary junctions are characterized by a finite subgap resistance. Moreover, the presence of normal conductive channels in the barrier, i.e. regions of negligible local I_cR_N product, would result in a resistive shunt of the junction and therefore high dissipation. R_{eff} is then well approximated by the normal resistance R_N even at frequencies below $\frac{2\Delta_d}{h}$, in case the resistive shunt dominates the R_N value. Thence, recalling the definition of the transmon quality factor $Q_a = \frac{f_a}{\Delta f}$ and using the following expression for the total capacitance $C_\Sigma = \frac{I_c}{2\pi\Phi_0 f_a^2}$, the transmon linewidth Δf writes as follows:

$$\Delta f = \frac{f_a^2 \Phi_0}{I_c R_N}. \tag{6.4}$$

Equation (6.4) expresses Δf in terms of the I_cR_N product of the grain boundary bi-epitaxial Josephson junctions. Therefore, the measurement of the I_cR_N product provides an estimate of the transmon linewidth, assuming that R_N is dominated by a resistive shunt independent of frequency.

In figure 6.10 (a) the I-V characteristics of a typical bi-epitaxial grain boundary junction with nominal $\alpha = 45°$, measured at $T = 300$ mK after fabrication (red stars) and after the extra Ar^+ milling (violet stars) made to tune the total critical current value I_c, are displayed. In figure 6.10 (b), the differential conductance, measured after the extra etching process, is shown up to voltages above $2\Delta_d \simeq 40$ mV. The large observed value of Δ_d is most probably due to meandering of the GB junction with facets having GB angles $\alpha = 0°$ or $90°$.

A reduction of more than an order of magnitude of the critical current, with a final $I_c \simeq 350$ nA, is observed as result of the milling process. The resulting I_c is much closer to the $(20 - 50)$ nA range, needed to get a transmon frequency around $f_a \simeq 5$ GHz.

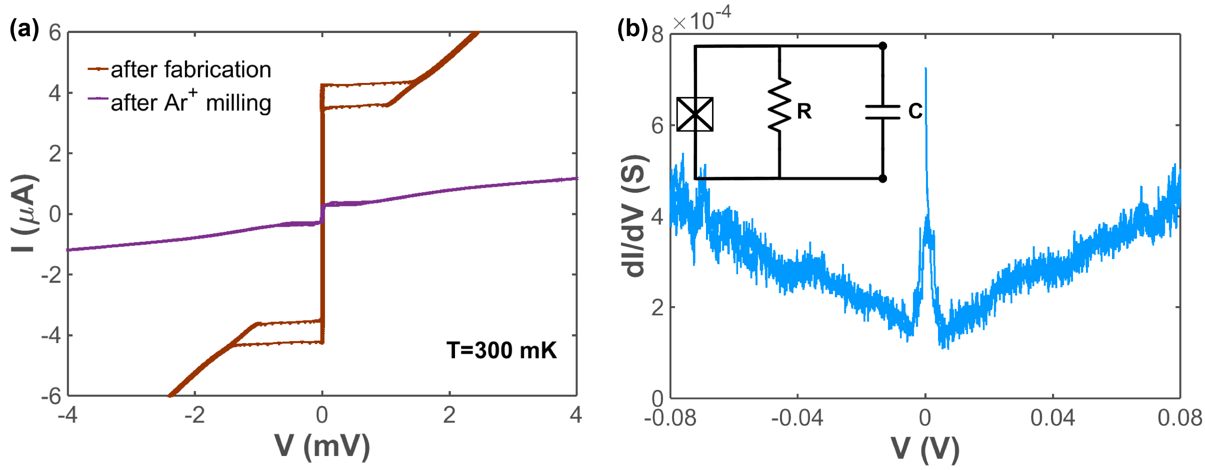

Figure 6.10: (a) Current-voltage characteristics measured at T = 300 mK, after fabrication (red stars) and after the extra etching process made to reduce the device I_c (violet stars). (b) Differential conductance measured after extra etching process, at T = 300 mK, up to voltages above $2\Delta_s$. The inset is a schematic circuit for the transmon device, where R represents the dissipative term.

However, the decrease in I_c is associated with a reduction of the I_cR_N product, from $\simeq 2$ mV down to $\simeq 1.1$ mV. The I_cR_N products, obtained from the DC I-V characteristics of junctions characterized by a nominal $\alpha = 0°$ GB angle, are plotted as a function of the critical current density J_c in figure 6.11. Both the values before (green diamonds) and after the extra etching (red open circles) are displayed.

Although we observe a decrease of I_cR_N with decreasing J_c, it does not clearly follow the $I_cR_N \propto (J_c)^{0.5}$ scaling described by the intrinsically shunted junctions (ISJ) model[166, 167], which is displayed with a blue solid line in the same figure. The observed decrease might be due to faceting at the grain boundary interface, as confirmed by SEM imaging (see Fig.6.2(b)), with lower J_c due to facets with $\alpha \simeq 45°$. The $d-$wave symmetry of the YBCO order parameter, in fact, results in a strong angular dependence of the I_cR_N product[126]. In general, an $I_cR_N \simeq (100 \div 500)\,\mu$V is measured for junctions or SQUIDs characterized by $I_c < 100$ nA. Using equation (6.4), this value of the I_cR_N product results in a $\Delta f \simeq (100 \div 500)$ MHz and so in good agreement with the values experimentally observed. This result suggests that the quasiparticles conductance below $2\Delta_d$ of the employed JJs is well approximated by the one extracted from the normal resistance R_N. In fact, the low values of the I_cR_N product as compared to the YBCO $d-$wave gap $\Delta_d \simeq 25$ meV indicate that resistive shunts are present in the GB barrier. These resistive shunts seem also to represent the dissipation source responsible for the measured YBCO transmon decoherence rate. A better understanding of the origin of this shunting resistance in the barrier is provided by voltage noise measurement across the junctions. Assuming the RSJ model for the I-V characteristic (over-damped junction, see section 2.1.2) and that the voltage fluctuations are caused both by critical current δI_c and normal resistance δR_N fluctuations, the power spectral density of the voltage across the junction at a given frequency f writes as[168]

$$S_V(f) = (V - R_dI)^2 S_I(f) + V^2 S_R(f) + k(V - R_dI)V S_{IR}(f), \tag{6.5}$$

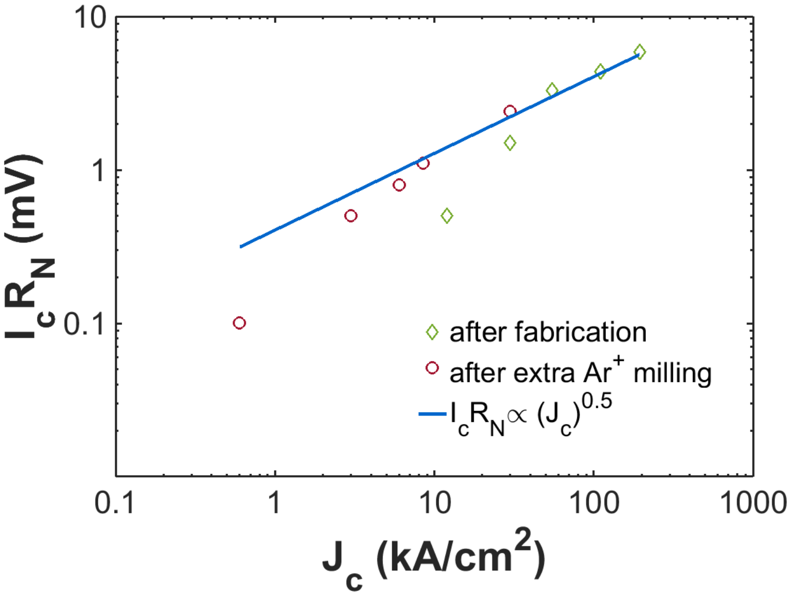

Figure 6.11: I_cR_N product as a function of the critical current density J_c for junctions characterized by $\alpha = 0°$, measured after fabrication (green diamonds) and after the extra etching process (red open circles). The blue solid line represents the scaling predicted by the ISJ model.

where $S_I = |\delta I_c/I_c|^2$ and $S_R = |\delta R_N/R_N|^2$ are respectively the relative critical current and normal resistance fluctuations, $S_{IR} = |\delta I_c/I_c||\delta R_N/R_N|$ is the cross-spectral density of the fluctuations, and $k = 2\langle\cos(\Delta\phi(t))\rangle$ is the time average of the cosine of the phase difference between δI_c and δR_N fluctuations. Uncorrelated fluctuations are characterized by $k = 0$, whereas perfectly correlated fluctuations by $k = 2$ if in phase, and by $k = -2$ if out of phase. R_d is the voltage dependent differential resistance of the junction. For a homogeneous GB barrier with a uniform current flow, the same junction area is involved in both the tunnelling of quasiparticles and Cooper pairs, such that $I_c \propto \frac{1}{R_N}$ and thence $S_I = S_R$. The ISJ model, assuming the presence of localized quasiparticles states in the homogeneous GB barrier and resulting in a leakage normal current, predicts a ratio $q = \sqrt{\frac{S_I}{S_R}} = 2$[167, 166]. Finally, a non homogeneous GB barrier consisting of N parallel transport channels, among which only one carries supercurrent, would result in a q ratio as large as $\sqrt{N}$. Moreover, the ratio $q^2 = \frac{S_I}{S_R} = \frac{A_{qp}}{A_{cp}}$ is equal to the ratio of the area for the quasiparticleas channels A_{qp} and the area for the Cooper pairs channels A_{cp}[169]. Figure 6.12(a) displays typical voltage noise spectra for three different values of I_b. The spectra are the sum of the $1/f$ background plus one or more Lorentzian spectra, depending on the number of two-level fluctuators (TLFs) present. From the measured voltage spectra at various bias currents, the amplitude of the power spectral density at 10 Hz is extracted and plotted as a function of I_b (see Fig.6.12(b)) The data in Fig.6.12(b) show an abrupt increase of S_V at bias current I_b close to the critical current $I_c \simeq 5.5\,\mu$A, as consequence of the large value of the differential resistance $R_d = \frac{dV}{dI}$. The data are dominated by the critical current fluctuations S_I at low bias currents close to I_c, whereas by the normal resistance fluctuations S_R at larger bias currents $I_b \gg I_c$. Voltage steps in

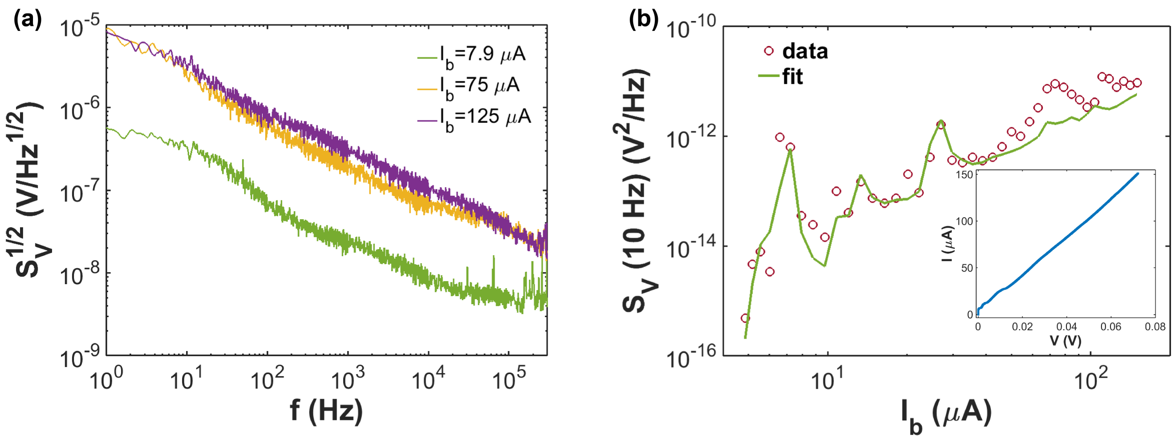

Figure 6.12: (a) Typicial voltage noise spectra for three different values of the bias current I_b. (b) Voltage spectral density S_V at $f = 10$ Hz as function of the bias current I_b, measured at $T = 4$ K for a SQUID device. Inset: I-V characteristic at $T = 4$ K.

the IV characteristic (see inset in Fig.6.12(b)) associated to resonances also cause spikes of R_d, which results in sharp peaks of the voltage noise across the GB junctions. The presence of TLFs characterized by Lorentzian power spectra (see Fig.6.12(a)), instead, produces the observed smooth humps in S_V at $I_b > 60\,\mu$A. For a quantitative analysis of the measured noise, the data shown in Fig.6.12(b) are fitted to Eq.(6.5). The green solid line represents the best fit, from which $S_I = 0.9 \times 10^{-8}$ Hz^{-1}, $S_R = 0.1 \times 10^{-8}$ Hz^{-1} and $k = -1$ have been extracted. The ratio $\frac{S_I}{S_R} \simeq 10$ indicates that $A_{qp} \simeq 10A_{cp}$ and that the GB barrier is highly non-homogeneous. Moreover, using the amplitude of the relative critical current fluctuations at 1 Hz ($\sqrt{S_I} \simeq 3 \times 10^{-4}Hz^{-1/2}$) in Eq.(2.63), a dephasing time $T_\phi \simeq 200$ ns ($\Delta f \simeq 5$ MHz) at $f_a = 5$ GHz is estimated. This estimate suggests that the transmon linewidth extracted from the spectroscopy measurement are mainly due to relaxation processes. However, critical current fluctuations are very sample dependent and can contribute significantly to the transmon decoherence.

In order to get larger I_cR_N values, the quality of the grain boundary interface has to be improved. This could be, most probably, achieved by reducing the junction width below the actual 200 nm resulting in low I_c junctions directly after patterning without the detrimental use of additional Ar$^+$ milling (see Fig.6.11). At the same time it allows for a well defined GB angle α with a reduced number of facets. Moreover a detailed analysis of the microscopic structure of the GB via transmission electron microscope imaging, could provide a better understanding of the origin of the quasiparticle channels acting as resistive shunts and help for the optimization of the YBCO growth at the boundary interface. These fabrication improvements will be the starting points for future experiments.

Chapter 7

Conclusions and Outlook

Driven by the need of new experimental insights, required for obtaining new hints on the microscopic mechanism leading to superconductivity in YBCO and in cuprates in general, the main goals of this thesis project was the development and the implementation of new tools able to perform experiments in previously inaccessible regimes. In this respect, YBCO quantum devices have been realized and investigated. In the following the main results and achievements are summarized.

In the appended paper **I**, nanowire based YBCO nanoSQUIDs, implementing the Dayem bridge configuration, are presented. These devices are characterized by transport properties very close to the pristine bulk material, and they are potential tools to study fundamental physics by looking at the fluxoid quantization via transport measurements. The nanoSQUIDs show critical current modulation as a function of the externally applied magnetic flux in the whole temperature range up to the critical temperature $T_c \simeq 83$ K of the devices. Thanks to the development of numerical methods that allow for a very accurate estimation of the nanoSQUIDs effective area, the value of the magnetic flux quantum Φ_0, which depends on the charge pairing, has been evaluated. The $4e$ charge pairing, which would result in a value of magnetic flux quantum $\Phi_0 = h/4e$, predicted as a consequence of the presence of a pair density wave of the superconducting condensate, has not been observed in the presented devices. This has been attributed to the fact that close to optimally doped YBCO thin films were used for the realization of the nanoSQUIDs. PDW has been mainly predicted for underdoped YBCO, and the employment of this kind of films is subject of present and future investigations. Another very important result is that, thanks to the nanometer size of the devices and the consequent very small inductance, an ultra low white magnetic flux value below $1\,\mu\Phi_0/\sqrt{\mathrm{Hz}}$ is observed. This makes the nanoSQUIDs very attractive for application in nanomagnetism, such as detection of magnetic nanoparticles, and as general magnetic flux detectors. In paper **II**, we report on nanowire based YBCO nanoSQUIDs directly coupled to an in-plane pickup loop. The pickup loop, mainly coupled via kinetic inductance to the nanometer sized SQUID loop, allows for a significant increase of the effective area of the device in agreement with full numerical calculations. Moreover, the larger effective area does not affect the white flux noise, resulting in a higher sensitivity to magnetic field, which could be further extended to the $\mathrm{fT}/\sqrt{\mathrm{Hz}}$ level by means of a bigger pickup loop and a larger coupling. The critical current noise spectrum is frequency dependent, and well fitted by a sum of Lorentzians. The critical current noise in nanowires might be associated to fluctuations of the electronic nematic order, an intrinsic property of the cuprates HTS. A systematic investigation of the critical current and normal resistance noise in YBCO nanowires as a function of the lateral dimensions, the temperature and the doping is currently ongoing.

With papers **III** and **IV**, the feasibility of the strong coupling regime and consequently of a YBCO transmon is proven. In particular, in paper **III** the microwave losses from the dielectric materials commonly implemented for the growth of YBCO thin films and suitable for the realization of bi-epitaxial JJs are investigated in the single photon regime. To minimize the losses from the superconductor and allow for the identification of the dielectric losses, Niobium CPW resonators are used in this work. The temperature and the power dependence are successfully compared to a theoretical model assuming the presence of two-level systems (TLSs) in the dielectric, which couple via dipole moment to the electric field in the resonator. As main outcome of the comparison of different dielectric materials, LSAT has been identified as the ideal substrate material for HTS microwave devices operated in the single photon limit. In paper **IV**, instead, the unloaded quality factor of a YBCO CPW resonator patterned on LSAT substrate covered by a CeO_2 seed layer is investigated in the single photon regime. The seed layer is necessary for the fabrication of YBCO bi-epitaxial JJs. Data from a device for which a Niobium film replaces the YBCO are also presented. The temperature dependence in the millikelvin range and the power dependence are studied, and compared to the TLS model from which dielectric (from the CeO_2 layer) and background losses (from the YBCO and Niobium films) values are extracted. These values indicate that the YBCO film contributes with larger conductor losses compared to Niobium, whereas the dielectric losses, coming mainly from the CeO_2 seed layer, are consistent. Nevertheless, a value of $Q_0 \simeq 2000$ at the single photon limit demonstrates that the strong coupling regime is accessible for YBCO devices as well.

Finally, in paper **V** the realization and the characterization of the first YBCO transmon qubits, employing bi-epitaxial grain boundary Josephson junctions, is reported. From the measurement of the transmission signal through the qubit-resonator system, vacuum Rabi splitting between the eigenstates describing the coupled system is observed and the coupling strength is estimated. The spectroscopic linewidth, representative of the qubit decoherence rate, is studied in comparison to intrinsic dissipation sources for YBCO. The transmon is successfully used as spectrometer to detect the presence of a subdominant imaginary $s-$wave component of the superconducting order parameter. A fully gapped superconducting state results in the suppression of the nodal quasiparticles and in the shifting of midgap states far from the Fermi energy. Both are among the main dissipation sources contributing to decoherence in YBCO quantum devices. Indeed, a significant improvement of the transmon coherence time is observed by applying a high in-plane magnetic field, which is expected to enhance the presence of the subdominant gap. An additional decoherence source has been identified in a resistive shunting of the junctions, associated to the presence of normal transport channels in the grain boundary barrier. In this respect, an improvement can be obtained by making higher quality grain boundary junctions, aiming at large I_cR_N products. A future direction will be to reduce the barrier size below the actual 200 nm, and to make a systematic investigation of the YBCO growth at the grain boundary interface.

Appendices

Appendix A

Interacting loop-current model

Following ref.[98], the total energy U of a network of interacting superconducting loops can be written in a matrix form as:

$$U = \frac{1}{2}\mathbf{I}^{\dagger}(\mathbf{L} - \mathbf{l})\mathbf{I}, \tag{A.1}$$

where the element I_m of the vector $\mathbf{I}$ represents the current in the loop m, $\mathbf{I}^{\dagger}$ is the transpose, $\mathbf{L}$ is a diagonal matrix of inductances and $\mathbf{l}$ is an off-diagonal matrix of the inductance elements shared by adjacent loops. In the case of the three loops network sketched in Fig.A.1, the total inductance matrix writes as:

$$\mathbf{L} - \mathbf{l} = \begin{pmatrix} L_1 & -l_{12} & -l_{13} \\ -l_{12} & L_2 & -l_{23} \\ -l_{13} & -l_{23} & L_3. \end{pmatrix}$$

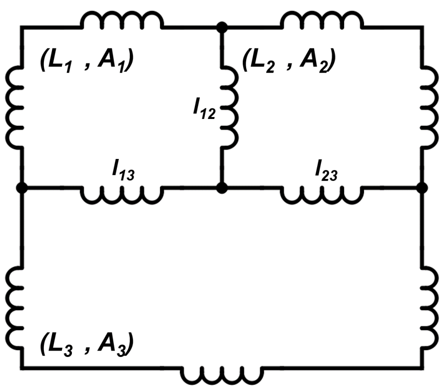

Figure A.1: Sketch of a three loops network. L_i and A_i are respectively the total inductance and the area of the i^{th} loop.

Within this formalism the fluxoid quantization condition writes as:

$$(\mathbf{L} - \mathbf{l})\mathbf{I} = \mathbf{L}\mathbf{I}^{\mathbf{0}}, \tag{A.2}$$

where

$$\mathbf{I}^0 \equiv L^{-1}(\mathbf{\Phi} - \mathbf{N\Phi_0}) \tag{A.3}$$

is the bare loop currents vector. Here $\mathbf{\Phi}$ is the vector of the applied flux in the loops, and $\mathbf{N}$ is the vector of the vorticity (number of fluxoid quanta in the loops). Using equations (A.2) and (A.3), the loop currents vector can be written as:

$$\mathbf{I} = (\mathbf{L} - \mathbf{l})^{-1}(\mathbf{\Phi} - \mathbf{N\Phi_0}), \tag{A.4}$$

hence, the total network energy U can be expressed as:

$$U = \frac{1}{2}(\mathbf{\Phi} - \mathbf{N\Phi_0})^{\dagger}(L - l)^{-1}(\mathbf{\Phi} - \mathbf{N\Phi_0}). \tag{A.5}$$

Now, for the specific network sketched in Fig. 2.16(b), the energy U, starting from eq.(A.5) and after some algebraic steps, writes as follows:

$$\begin{aligned} U = \frac{1}{2(L_{nS}L_{loop} + L_c^2)} * [&L_{nS}\left(BA_{loop} - N_{loop}\Phi_0\right)^2 + \\ &2L_c\left(BA_{loop} - N_{loop}\Phi_0\right)\left(BA_{nS} - N_{nS}\Phi_0\right) + \\ &+L_{loop}\left(BA_{nS} - N_{nS}\Phi_0\right)^2]. \end{aligned} \tag{A.6}$$

Here L_{nS} and A_{nS} are respectively the total inductance and the effective area of the nanoSQUID loop, L_{loop} and A_{loop} are respectively the total inductance and the effective area of the pickup loop, and B is the externally applied magnetic field. For a fixed value of $N_{loop} = 0$ and a variable N_{nS}, equation (A.6) represents a set of parabolas (see Fig.A.2). The magnetic field periodicity ΔB is given by the distance of two neighbouring parabola crossings, which corresponds to two consecutive changes of vorticity in the nanoSQUID loop (see Fig.A.2). Calculating the magnetic field at which two consecutive parabolas cross $B_{cr}(N_{nS})$, e.g. for $N_{nS}+1$ and N_{nS}, as a function of N_{nS} one obtains:

$$B_{cr}(N_{nS}) = \Phi_0 L_{loop}(N_{nS}+1)\frac{1}{L_{loop}A_{nS} + L_c A_{loop}}. \tag{A.7}$$

Here $\Delta U = U(0; N_{nS}+1) - U(0; N_{nS}) = 0$, with $N_{loop} = 0$ (zero vorticity in the pickup loop) has been used for the derivation of Eq.(A.7). The periodicity is then given by:

$$\begin{aligned} \Delta B = B_{cr}(N_{nS}+1) - B_{cr}(N_{nS}) &= \\ &= \frac{\Phi_0}{A_{nS} + \frac{L_c A_{loop}}{L_{loop}}}, \end{aligned} \tag{A.8}$$

and thus the following expression for the effective area of the whole network is obtained:

$$A_{eff} = A_{nS} + \frac{L_c}{L_{loop}}A_{loop}. \tag{A.9}$$

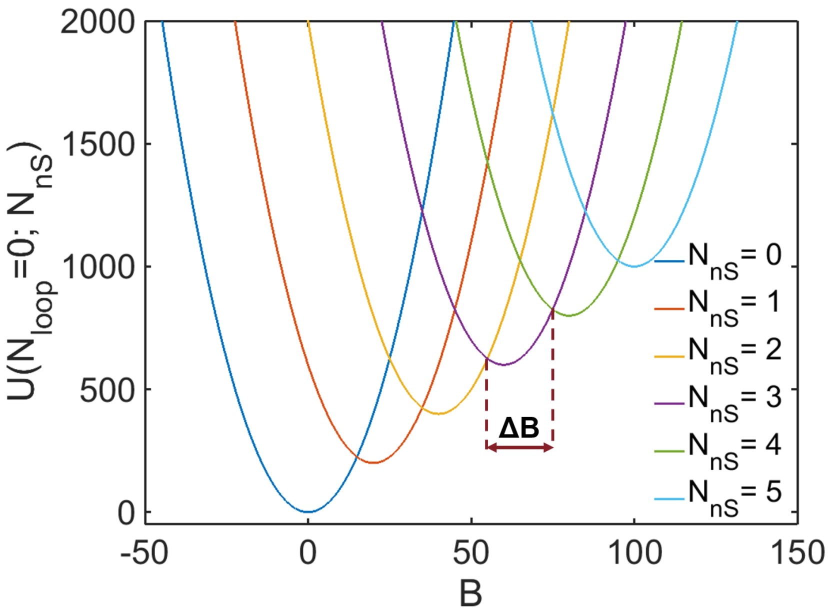

Figure A.2: Different parabolas of the total network energy U for $N_{loop} = 0$ and for six different values of the nanoSQUID vorticity number N_{nS}.

Appendix B

Fabrication recipes

In this appendix the details of the fabrication processes are reported. The actual parameters listed here are peculiar of the equipments at the Nanofabrication Laboratory at the Department of Microtechnology and Nanoscience, Chalmers university.

YBCO nanoSQUIDs

1. **Substrate cleaning**. Each substrate is first kept in acetone at 50 °C for 10 min,then in ultrasonic bath for 5 min at 50 °C, followed by a careful cleaning using a cotton tip. Finally, the substrate is rinsed in isopropanol (IPA) and dried with nitrogen.

2. **YBCO deposition**. The YBCO film is epitaxially grown by PLD, keeping the substrate temperature at 760 °C and the chamber in an O_2 atmosphere with a pressure of 0.6 mbar. The laser fluence is ≈ 2 J/cm^2. A 50 nm thick film is obtained with 900 pulses, at a repetition rate $f_R = 6$ Hz. After the deposition, the YBCO film is post annealed in an O_2 atmosphere at 900 mbar while cooling down at a 5 °C/min rate.

3. **Au capping layer**. The gold capping layer is deposited by magnetron sputtering at 5 μbar pressure and room temperature. A 50 nm thick layer is obtained with a deposition rate of roughly 1 nm/sec.

4. **C deposition**. A roughly 80 nm thick carbon film is deposited by PLD at room temperature and high vacuum ($< 10^{-6}$ mbar). The deposition rate is roughly 15 nm/min.

5. **e-beam resists**. A double layer e-beam resist is spun on the chip and baked. The bottom resist is a MMA co-polymer EL4 (4% solid in Ethyl lactate), whereas ARP 6200.13 1:2 is used as top layer resist. Both layers are spin-coated at 6000 rpm for 1 min and 30 sec and than baked for 5 min at 95 ° C on a hotplate. The final resist thickness are ≈ 60 nm for both layers.

6. **e-beam lithography**. The resist layers are exposed by an electron beam at 100 kV, according to the desired device design. Nanometer sized structures are exposed with a 2 nA beam current and a base dose of 150 μC/cm^2. The actual dose of each

structure section is varied according to the result of proximity effect corrections. The larger structures (micrometer sized electrodes and bonding pads) are, instead, exposed with a 35 nA beam current and a base dose of 250 μC/cm^2.

7. **Resist development.** The top layer resist is developed in o-Xylene for 40-45 sec, then rinsed in IPA and dried by N_2. The bottom layer, instead, is developed in MBIK:IPA 1:3 for 35-40 sec, then rinsed in IPA and dried by N_2.
8. **Resist descum**. A resist descum process is done via O_2 plasma at 50 W and 250 mTorr pressure for 10 sec.
9. **Cr deposition**. A 12-15 nm thick chromium film is deposited by e-beam evaporation at 1 Å/sec rate.
10. **Cr lift-off**. The chromium is lifted-off in a remover mR-400 at 65 °C.
11. **First C etching**. The unprotected carbon (no chromium on top) is etched away via O_2 plasma at 50 W and 100 mTorr pressure for 25 min.
12. **Au/YBCO etching**. The gold and YBCO regions not covered by the carbon mask are etched via gentle Ar^+ milling. The chosen acceleration voltage for the Ar ions is $\Delta V = 300$ V, which is right above the YBCO etching threshold. The other parameters used are the following: $I_{beam} = 5$ mA, the chip rotates at a tilting angle of 5°, $P_{base} \approx 1 \times 10^{-7}$ mbar, $P_{process} \approx 1.5 \times 10^{-4}$ mbar and the Ar flow is 4 sccm. No charge neutralizer is used in this case. Using these parameter, the etching rates for the different materials are as follows: 5 nm/min for the Au, 7 Å/min for the YBCO, and 1.5 nm/min for the MgO. The total etching time is ≈ 110 min, which results in a ≈ 150 nm step: 50 nm Au, 50 nm YBCO and 50 nm MgO.
13. **Final C etching**. The remaining carbon is etched by O_2 plasma for 25 min, at 50 W and 100 mTorr pressure.

Niobium CPW resonators

1. **Substrate preparation**. Each substrate is cleaning as described at point 1 in the previous section. The cleaning is followed by an annealing at 200 °C for1 hour.
2. **Nb deposition**. The Niobium films are deposited by ultra high vacuum magnetron sputtering, using a 200 W DC-power. The Nb target is pre-sputtered for 5 min before starting the deposition. The 200 nm thick film is deposited in 5 steps, with a 4 min cool down time interval between each step. The deposition is done at 8 μbar and using an Ar flow of 60 sccm.
3. **e-beam lithography**. A UV5 0.8 resist layer is spun at 3000 rpm and baked at 130 °C for 2 min. The resist is exposed using a 35 nA e-beam current, with a dose of 25 μC/cm^2, according to the resonator design.
4. **Resists development**. After the exposure, the chip is first baked for 90 sec on hotplate at 130 °C, then developed in MF-24A for 40 sec, and finally rinsed with water and dried by N_2.

5. **Nb etching**. The niobium is etched by RIE using NF_3 gas. A laser interferometer end-point detection is used to establish the etching time needed. 1 min and 30 sec are normally enough to etch 200 nm of Nb, plus roughly 10 nm of over-etching into the substrate.

6. **Resist removal**. The chip is first submerged in remover mR-400, and kept for many hours (overnight is preferable). A 7 min ashing in O_2 plasma is then used to better clean the chip from any resist residual.

YBCO bi-epitaxial Josephson junctions

1. **Substrate cleaning**. See point 1 in the first section.

2. **CeO_2 deposition**. A 40 nm thick CeO_2 film is deposited by magnetron sputtering in O_2 atmosphere at 800 °C and a 0.1 mbar pressure. The target is pre-sputtered for 10 min. The film is deposited at a 2 nm/min with a 30 mm distance between the target and the substrate. The deposition is followed by a post annealing in O_2 at 650 mTorr while cooling down at a 10 °C/min.

3. **Laser writer photo-lithography for CeO_2 patterning**. An S1813 photoresist layer is spun at 7000 rpm and baked at 95 °C for 5 min. The resist is exposed using a direct laser writing tool, implementing a single diode laser source with a 405 nm wavelength, according to desired seed layer design. The tool allows to define resist structures with lateral dimensions down to 0.7 μm.

4. **Resist development**. The resist is developed in MF-319 for 35 sec, then rinsed in water and dried by N_2.

5. **Seed layer etching**. The CeO_2 regions, not protected by the resist mask, is etched by Ar^+ milling. The etching parameters are: a base pressure of $\simeq 1 \times 10^{-7}$ Torr, $\Delta V = 300$ V for the Ar ions acceleration voltage, the beam current is set to $I_{beam} =$ 13 mA, the Ar flow is 3 sccm and it results in a current density of 0.08 mA/cm^2. The chip is rotated at 3 rpm and tilted at 5°. An electron emitter is used to ensure neutral ion beam space charge. The etching process is monitored by means of a secondary ion mass spectrometer (SIMS). The CeO_2 is etched with a rate of $\simeq 2$ nm/min.

6. **Resist removal**. The resist mask is removed by submerging the chip in remover mR-400, and kept for many hours (preferably overnight). After ultrasonic bath, a 5 min Ar stripping at 50 W is used to better clean the CeO_2 surface. The latter step is crucial to obtain a high quality YBCO c-axis oriented film.

7. **YBCO deposition**. The YBCO is epitaxially grown on the patterned $CeO_{2/}$LSAT substrate by PLD, using a template technique. The technique consists in depositing first a thin template layer at 760 °C, and then the actual YBCO film at 810 °C optimized for a high quality bi-epitaxial YBCO film (see section 3.2). A $\simeq 120$ nm thick film is obtained with 1900 laser pulses, at a repetition rate $f_R = 6$ Hz. The laser fluence is $\simeq 1.5$ J/cm^2. The film is deposited in a 0.6 mbar O_2 pressure. After

the deposition, the YBCO film is post annealed in an O_2 atmosphere at 800 mbar while cooling down at a 10 °C/min rate.

8. **Au deposition**. The YBCO film is covered by 100 nm of gold, deposited by magnetron sputtering as described in point 3 of the first section.

9. **Laser writer photo-lithography for Au patterning**. Gold cross marks for e-beam lithography and bonding pads are defined using the same procedure as described at point 3 of this section.

10. **Resist development**. The S1813 photoresist is developed in MF-319 for 15 sec, then rinsed in water and dried by N_2.

11. **Au etching**. The thickness of the unprotected gold regions is reduced from 100 nm down to 40 nm via Ar^+ milling, using the same etching parameters reported at point 5 of this section. The Au etching rate is roughly 6 nm/min.

12. **Resist removal**. The remaining resist mask is removed as described at point 6 of the second section.

13. **C deposition, e-beam lithography, resist development, Cr lift-off, first C etching**. See points from 4 to 11 of the first section. The only differences are: the e-beam base doses, which are 160 and 200 μC/cm^2 respectively for the low and high beam current; and the top resist layer development time, which is 10-15 sec in this case.

14. **Au/YBCO etching**. The gold and YBCO regions not covered by the carbon mask are etched via Ar^+ milling. The parameters used are the same as at point 5 of this section, with the exception of the beam current used. At this step, a current $I_{beam} = 22$ mA, resulting in a current density of 0.13 mA/cm^2, is used instead. Again, the etching process is monitored by SIMS detector. The YBCO is etched with a rate of $\simeq 3$ nm/min.

15. **Final C etching**. The remaining C mask is etched by O_2 plasma as at pint 13 of the first section.

16. **Au removal**. The final protective capping gold layer is removed by O_2 plasma for 60 min, at 100 W and 15 mTorr pressure.

YBCO CPW resonators

1. **Substrate cleaning**. See point 1 of the first section.

2. **Seed layer deposition**. The CeO_2 seed layer is deposited as described at point 2 of the third section.

3. **YBCO deposition**. See point 7 of the third section.

4. **Au deposition**. See point 8 of the third section.

5. **Photo-lithography for YBCO resonator patterning**. The S1813 photoresist has been patterned, according to the resonator, using both the laser writer as described at point 3 of the previous section and alternatively a mask aligner tool. In the latter case, the resist is exposed by a UV lamp at roughly 200 W, and the desired design is obtained using a Cr mask patterned on a transparent glass. A new Cr mask, realized by e-beam lithography, is required every time a modification of the device design is made. This makes the laser writer the preferable technique.

6. **Au/YBCO etching**. See point 14 of the previous section.

7. **Resist removal**. See point 12 of the previous section.

8. **Final Au removal**. See point 16 of the previous section.

Appendix C

Inductances and effective area simulations

Following ref.[170], the current distribution in a superconducting thin film of any shape can be calculated and used to determine the inductance of a specific device. Here it is considered a superconducting device whose typical length scales are such that:

$$t \leq \lambda_L, \tag{C.1}$$

where t is the thickness of the superconducting film, l and w represent respectively the typical length and width of the device in the plane orthogonal to t, and λ_L is the London penetration length. The starting point are the following London and Maxwell equations for the current density $\mathbf{J}$ and the magnetic field $\mathbf{B}$ induced by this current, in absence of external field:

$$\begin{aligned} \mu_0 \lambda_L^2 \nabla \times \mathbf{J} + \mathbf{B} &= 0 \\ \nabla \times \mathbf{B} &= \mu_0 \mathbf{J}. \end{aligned} \tag{C.2}$$

In the case set by equations (C.1), it is possible to neglect the component of $\boldsymbol{J}$ along the z direction, such that $\mathbf{J} = (j_x(x,y), j_y(x,y), 0)$. Then, introducing the Pearl length $\lambda_\perp = 2\lambda_L^2/t$ and using the *Biot-Savart law* for the magnetic field, the first of equations C.2 can be written as:

$$\mu_0 \lambda_\perp (\nabla \times \mathbf{J}(x,y))_z + \frac{1}{4\pi} \int_S \mathbf{J}(P) \times (\nabla \frac{1}{|\mathbf{P} - \mathbf{P}_0|}) dxdy = 0, \tag{C.3}$$

where P and P_0 are two points in the xy plane. To simplify the problem, a *stream function* $\psi(x,y)$ for the current density $\mathbf{J}$ is introduced:

$$j_x = \frac{\partial \psi}{\partial y} \quad \text{and} \quad j_y = -\frac{\partial \psi}{\partial x}. \tag{C.4}$$

As it is defined, the stream function represents the total current:

$$I(P_0, P) = \int_{\Gamma_P} J dl = \psi(P) - \psi(P_0) \tag{C.5}$$

where Γ_P is an open path integral connecting P and P_0. Indeed, ψ allows for an easy formulation of the boundary conditions, needed to solve the whole problem, i.e. no current through the surface, total circulating current around a superconducting loop.

The expression for the total energy of the system, given by the sum of the kinetic energy E_{kin} plus magnetic energy E_M, writes as:

$$E = \frac{1}{2}\int_S (\mu_0 \lambda_\perp j^2 + \mathbf{J} \cdot \mathbf{A}) dxdy. \tag{C.6}$$

Using the stream function, the kinetic and the magnetic contributions can be respectively written as:

$$\begin{aligned} E_{kin} &= \frac{\mu_0}{2}\int_S \lambda_\perp (\nabla_{xy}\psi(P))^2 dxdy \\ E_M &= \frac{\mu_0}{8\pi}\int_S\int_S \frac{\nabla_{xy}\psi(P) \cdot \nabla_{x_0 y_0}\psi(P_0)}{|P - P_0|} dx_0 dy_0 dxdy \end{aligned} \tag{C.7}$$

Since

$$\begin{aligned} E_{kin} &= \frac{1}{2} L_{kin} I^2 \\ E_M &= \frac{1}{2} L_{ex} I^2, \end{aligned} \tag{C.8}$$

by evaluating the integrals in C.7 for a given value of the total current I in the system, one can easily get an estimation for the kinetic L_{kin} and the geometric L_{ex} inductance.

In the case of a superconducting loop as the nanoSQUID devices presented in chapter 4, from the knowledge of the total current distribution in the device, it is also possible to get an estimation of the effective area A_{eff}. In fact, A_{eff} can be evaluated from the total magnetic moment m, induced by the screening current I_s circulating around the nanoSQUID loop when an external magnetic field B is applied, as follows[171]:

$$A_{eff} = \frac{m}{I}. \tag{C.9}$$

In the presence of a large pickup loop, inductively coupled to the small nanoSQUID loop, the effective area can not be calculated via eq.(C.9). However, in this case, A_{eff} can be obtained from the evaluation of the total fluxoid value Φ' through the nanoSQUID loop. For a given screening current density $\mathbf{J}_s$ circulating around the hole, the fluxoid is expressed as follows:

$$\Phi' = \oint_\Gamma \nabla\phi \cdot d\mathbf{l}_\Gamma = \oint_\Gamma \mu_0 \lambda_\perp \mathbf{J_s} \cdot d\mathbf{l}_\Gamma + \oint_\Gamma \mathbf{A} \cdot d\mathbf{l}_\Gamma, \tag{C.10}$$

where μ_0 is the vacuum permeability, and the integral is over any contour Γ enclosing the hole. The second term in eq.C.10 represents the ordinary magnetic flux through the contour Γ, where $\mathbf{A}$ is the vector potential associated to the magnetic field $\mathbf{B}$. The effective area can be then calculated from the fluxoid, assuming zero vorticity in the pickup loop and zero circulating current in the nanoSQUID loop, as follows:

$$A_{eff} = \frac{\Phi'}{B}. \tag{C.11}$$

Acknowledgements

"When you try your best, but you do not succeed". You realize that with others help, you can. For this thesis work I took advantage of many persons' help. I allow myself to divide them in three different categories: the person I chase, those I look up to and those I look forward to.

My greatest gratitude goes to my supervisor Thilo Bauch. Thanks for making me part of this project. You have taught me a lot in the last five years, and much more I still have to learn from you. You are the person I have been chasing during all this time. I kept asking myself: "are you getting as good?", and the answer was always the same: "no, not even close". This has motivated me to do better and better.

I would like to thank all the people I have looked up to during my PhD studies. First, a deep thank to my co-supervisor and examiner Floriana Lombardi. You have been essential for the achievement of all the results and in the writing process. Your passion for research has always been inspiring.

Thanks to all the guys I have been working with: Chirag, David, Domenico, Edoardo, Eric, Gunta, Luca, Reza, Riccardo, Shahid and Sophie. You all have given a significant contribution to my thesis. I am so proud of being part of such a great group.

Thanks to all the QDP members I had the pleasure to meet during the past five years. It has been stimulating and enjoyable to be surrounded by so many smart people devoted to science. A particular thank to Andreas and Philip for initiating me with the qubit measurements.

A special thanks to Astghik, Lars and Reza for being such good officemates. I have no idea how you managed to stand me all these years. You should share your secret.

Thanks to all the clean-room staff, your help with all the equipment has been essential for the successful realization of the devices. In particular, I would like to thank Henrik Fredriksen and Mats Hagberg. If I had given you ten sek each time I asked your help, you would have been richer than the king by now.

Thanks to Jukka Pekola for giving me the opportunity to work in his group and be part of a very interesting project. Collaborating with nice and smart persons like Klaara, Simone, Matthias, Timothé, Anna, Hung and all the others has been a honour and a pleasure.

Thanks to Jari Pentilla, Leif and Erkki for the different and very formative experience at Aivon. I have learned a lot from you guys. It has been very useful for my personal professional development.

Thanks to Hervé Courtois and all the Q-NET members for all the stimulating meetings.

Thanks to all the Q-NET students: Angie, Luca, Atsghik, Anna, Timothé, Mano, Maria, Prya, Robert, Maria, Jonna, Jorge, Sayanti and Pauline. It was nice to share with you our PhD experiences, and to have fun together.

Thanks to Pier Paolo. If it was not for you, most probably I would have not even moved to Sweden.

And finally the persons I always look forward to. They have unconsciously given a priceless contribution to all this five years work.

Thanks to Ughina, the best, the coolest and the most elegant roommate ever. My aware and constructive loneliness would have not been the same without you.

Thank you Angie, Rob&Ross, Flavia, Livia and Giuseppe for treating me so nicely and for all the happy time we had together. My heart is not big enough to love you as you deserve.

Thanks Ric, once again, for being such a good friend before being an essential co-worker. Like a succulent plant is green despite the desert, you are a great friend despite me.

Thanks to Antonio, Marcello, Piero, Pasquale and Enrico. You are my best and the most "accimati" friends. I am a very lucky captain. No matter what, no matter how far, I know you will always be there for me. A special thanks to you Doc for listening to all my overthinking and for sharing your couch.

Thanks Mamma, Papá, Rosario and Luisa. You are the best family one can desire.
Thanks to Federica. The gaze that shakes me, the smile that warms me up. You are what people call "Love".
You five are the persons I love most and I want to make most proud of me. Thanks for always making me feel beloved. It is such a good and vital feeling.

Marco
Göteborg, October 15th, 2016

Bibliography

[1] J.G. Bednorz and K.A. Müller. Possible high T_c superconductivity in the Ba-La-Cu-O system. In *Ten Years of Superconductivity: 1980–1990*, pages 267–271. Springer, 1986.

[2] Towards a complete theory of high T_c. *Nat. Phys.*, 2:138–143, 2006.

[3] B. Keimer, S.A. Kivelson, M.R. Norman, S. Uchida, and J. Zaanen. From quantum matter to high-temperature superconductivity in copper oxides. *Nature*, 518(7538):179–186, 2015.

[4] G. Ghiringhelli, M. Le Tacon, M. Minola, S. Blanco-Canosa, C. Mazzoli, N. B. Brookes, G. M. De Luca, A. Frano, D. G. Hawthorn, F. He, T. Loew, M. Moretti Sala, D. C. Peets, M. Salluzzo, E. Schierle, R. Sutarto, G. A. Sawatzky, E. Weschke, B. Keimer, and L. Braicovich. Long-range incommensurate charge fluctuations in (Y,Nd)$Ba_2Cu_3O_{6+x}$. *Science*, 337(6096):821–825, 2012.

[5] E.H. da Silva Neto, P. Aynajian, A. Frano, R. Comin, E. Schierle, E. Weschke, A. Gyenis, J. Wen, J. Schneeloch, Z. Xu, et al. Ubiquitous interplay between charge ordering and high-temperature superconductivity in cuprates. *Science*, 343(6169):393–396, 2014.

[6] M.H. Devoret, J.M. Martinis, and J. Clarke. Measurements of macroscopic quantum tunneling out of the zero-voltage state of a current-biased josephson junction. *Phys. Rev. Lett.*, 55:1908–1911, 1985.

[7] J.M. Martinis, M.H. Devoret, and J. Clarke. Energy-level quantization in the zero-voltage state of a current-biased josephson junction. *Phys. Rev. Lett.*, 55:1543–1546, 1985.

[8] J.M. Martinis, S. Nam, J. Aumentado, and C. Urbina. Rabi oscillations in a large josephson-junction qubit. *Phys. Rev. Lett.*, 89:117901, 2002.

[9] Y. Yu, S. Han, Xi Chu, S.-I. Chu, and Z. Wang. Coherent temporal oscillations of macroscopic quantum states in a josephson junction. *Science*, 296(5569):889–892, 2002.

[10] D. Vion, A. Aassime, A. Cottet, P. Joyez, H. Pothier, C. Urbina, D. Esteve, and M. H. Devoret. Manipulating the quantum state of an electrical circuit. *Science*, 296(5569):886–889, 2002.

[11] R. C. Jaklevic, John Lambe, A. H. Silver, and J. E. Mercereau. Quantum interference effects in josephson tunneling. *Phys. Rev. Lett.*, 12:159–160, 1964.

[12] Matti Hämäläinen, Riitta Hari, Risto J. Ilmoniemi, Jukka Knuutila, and Olli V. Lounasmaa. Magnetoencephalography-theory, instrumentation, and applications to noninvasive studies of the working human brain. *Rev. Mod. Phys.*, 65:413–497, 1993.

[13] M. Xie, J.F. Schneiderman, M.L. Chukharkin, A. Kalabukhov, S. Whitmarsh, D. Lundqvist, and D. Winkler. Benchmarking for on-scalp MEG sensors. *IEEE Trans. Appl. Supercond.*, 25(3):1–5, 2015.

[14] V. M. Zotev, A. N. Matlashov, P. L. Volegov, I. M. Savukov, M. A. Espy, J. C. Mosher, J. J. Gomez, and R. H. Kraus Jr. Microtesla MRI of the human brain combined with MEG. *J. Mag. Res.*, 194:115 – 120, 2008.

[15] A Chwala, J P Smit, R Stolz, V Zakosarenko, M Schmelz, L Fritzsch, F Bauer, M Starkloff, and H-G Meyer. Low temperature squid magnetometer systems for geophysical exploration with transient electromagnetics. *Supercond. Sci. Technol.*, 24(12):125006, 2011.

[16] Harold Weinstock, editor. *SQUID Sensors: Fundamentals, Fabrication and Application*, volume 329 of *Series E: Applied Sciences*. Kluwer Academic Publishers, 1996.

[17] R. Körber, J.H. Storm, H. Seton, J.P. Mäkelä, R. Paetau, L. Parkkonen, C. Pfeiffer, et al. SQUIDs in biomagnetism: a roadmap towards improved healthcare. *Supercond. Sci. Technol.*, 29(11):113001, 2016.

[18] M.H. Devoret and J.M. Martinis. Implementing qubits with superconducting integrated circuits. *Quantum Information Processing*, 3:163–203, 2004.

[19] M. H. Devoret and R. J. Schoelkopf. Superconducting Circuits for Quantum Information: An Outlook. *Science*, 339:1169, 2013.

[20] H. Paik, D. I. Schuster, L. S. Bishop, G. Kirchmair, G. Catelani, A. P. Sears, B. R. Johnson, M. J. Reagor, L. Frunzio, L. I. Glazman, S. M. Girvin, M. H. Devoret, and R. J. Schoelkopf. Observation of High Coherence in Josephson Junction Qubits Measured in a Three-Dimensional Circuit QED Architecture. *Phys. Rev. Lett.*, 1907:240501, 2011.

[21] M.H.S. Amin, A.Yu. Smirnov, A.M. Zagoskin, T. Lindstrom, S.A. Charlebois, T. Claeson, and A.Ya. Tzalenchuk. Silent phase qubit based on d-wave Josephson junctions. *Phys. Rev. B*, 71(6):64516–1, 2005.

[22] T. Bauch, F. Lombardi, F. Tafuri, A. Barone, G. Rotoli, P. Delsing, and T. Claeson. Macroscopic quantum tunneling in d-wave $YBa_2Cu_3O_{7-\delta}$ Josephson junctions. *Phys. Rev. Lett.*, 94(8):087003–1, 2005.

[23] T. Bauch, T. Lindström, F. Tafuri, G. Rotoli, P. Delsing, T. Claeson, and F. Lombardi. Quantum Dynamics of a d-wave Josephson Junction. *Science*, 311(5757):57–60, 2006.

[24] D. Gustafsson, D. Golubev, M. Fogelström, T. Claeson, S. Kubatkin, T. Bauch, and F. Lombardi. Fully gapped superconductivity in a nanometre-size $YBa_2Cu_3O_{7-\delta}$ island enhanced by magnetic field. *Nat. Nanotech.*, 8:25, 2013.

[25] H.K. Onnes. The superconductivity of mercury. *Comm. Phys. Lab. Univ. Leiden*, 122:124, 1911.

[26] W. Meissner and R. Ochsenfeld. Ein neuer effekt bei eintritt der supraleitfähigkeit. *Naturwissenschaften*, 21(44):787–788, 1933.

[27] F. London and H. London. The electromagnetic equations of the supraconductor. In *Proceedings of the Royal Society of London A: Mathematical, Physical and Engineering Sciences*, volume 149, pages 71–88. The Royal Society, 1935.

[28] L.D. Landau and V.L. Ginzburg. On the theory of superconductivity. *Zh. Eksp. Teor. Fiz.*, 20:1064, 1950.

[29] J. Bardeen, L. N. Cooper, and J. R. Schrieffer. Theory of superconductivity. *Phys. Rev.*, 108(5):1175, 1957.

[30] L.P. Gor'kov. Microscopic derivation of the Ginzburg-Landau equations in the theory of superconductivity. *Sov. Phys. JETP*, 9(6):1364–1367, 1959.

[31] Michael Tinkham. *Introduction to superconductivity.* Courier Corporation, 1996.

[32] A.P. Drozdov, I.A. Eremets, M.I. andTroyan, V. Ksenofontov, and S.I. Shylin. Conventional superconductivity at 203 kelvin at high pressures in the sulfur hydride system. *Nature*, 525(7599):72–76, 2015.

[33] M. K. Wu, J. R. Ashburn, C. J. Torng, P. H. Hor, R. L. Meng, L. Gao, Z. J. Huang, Y. Q. Wang, and C. W. Chu. Superconductivity at 93 K in a new mixed-phase Y-Ba-Cu-O compound system at ambient pressure. *Phys. Rev. Lett.*, 58:908–910, 1987.

[34] High-Temperature Superconductivity. Ginzburg, v.l. *Prog. Low Temp. Phys.*, 12, 1989.

[35] D.N. Basov, R. Liang, D.A. Bonn, W.N. Hardy, B. Dabrowski, D.B. Quijada, M.and Tanner, J.P. Rice, D.M. Ginsberg, and T. Timusk. In-plane anisotropy of the penetration depth in $YBa_2Cu_3O_{7-x}$ and $YBa_2Cu_3O_8$ superconductors. *Phys. Rev. Lett.*, 74(4):598, 1995.

[36] C. Villard, G. Koren, D. Cohen, E. Polturak, B. Thrane, and D. Chateignier. ab-plane anisotropy of transport properties in unidirectionally twinned $YBa_2Cu_3O_{7-\delta}$ films. *Phys. Rev. Lett.*, 77(18):3913, 1996.

[37] H.J.H. Smilde, A.A. Golubov, G. Rijnders, J.M. Dekkers, S. Harkema, D.H.A. Blank, H. Rogalla, H. Hilgenkamp, et al. Admixtures to d-wave gap symmetry in untwinned $YBa_2Cu_3O_7$ superconducting films measured by angle-resolved electron tunneling. *Phys. Rev. Lett.*, 95(25):257001, 2005.

[38] D.H. Lu, D.L. Feng, N.P. Armitage, K.M. Shen, A. Damascelli, C. Kim, F. Ronning, Z-X Shen, D.A. Bonn, R. Liang, et al. Superconducting gap and strong in-plane anisotropy in untwinned $YBa_2Cu_3O_{7-\delta}$. *Phys. Rev. Lett.*, 86(19):4370, 2001.

[39] J.R. Kirtley, C.C. Tsuei, C.J.M. Verwijs, S. Harkema, H. Hilgenkamp, et al. Angle-resolved phase-sensitive determination of the in-plane gap symmetry in $YBa_2Cu_3O_{7-\delta}$. *Nat. Phys.*, 2(3):190–194, 2006.

[40] T. Timusk and B. Statt. The pseudogap in high-temperature superconductors: an experimental survey. *Rep. Prog. Phys.*, 62(1):61, 1999.

[41] S. Chakravarty, H.-Y. Kee, and K. Völker. An explanation for a universality of transition temperatures in families of copper oxide superconductors. *Nature*, 428(6978):53–55, 2004.

[42] V.J. Emery and S.A. Kivelson. Importance of phase fluctuations in superconductors with small superfluid density. *Nature*, 374(6521):434–437, 1995.

[43] V. Hinkov et al. Spin dynamics in the pseudogap state of a high-temperature superconductor. *Nat. Phys.*, 3(3):780–785, 2007.

[44] M.J. Lawler, K. Fujita, J. Lee, A.R. Schmidt, Y. Kohsaka, Chung Koo Kim, H. Eisaki, S. Uchida, J.C. Davis, J.P. Sethna, et al. Intra-unit-cell electronic nematicity of the high-Tc copper-oxide pseudogap states. *Nature*, 466(7304):347–351, 2010.

[45] C. M. Varma, P. B. Littlewood, S. Schmitt-Rink, E. Abrahams, and A. E. Ruckenstein. Phenomenology of the normal state of Cu-O high-temperature superconductors. *Phys. Rev. Lett.*, 63:1996–1999, 1989.

[46] J. R. Waldram. *Superconductivity of metals and cuprates*. CRC Press, 1996.

[47] T. Sekitani, N. Miura, S. Ikeda, Y.H. Matsuda, and Y. Shiohara. Upper critical field for optimally-doped $YBa_2Cu_3O_{7-\delta}$. *Phys. Rev. B*, 346:319–324, 2004.

[48] C.C. Tsuei and J.R. Kirtley. Pairing symmetry in cuprate superconductors. *Rev. Mod. Phys.*, 72(4):969, 2000.

[49] C.C. Tsuei, J.R. Kirtley, G. Hammerl, J. Mannhart, H. Raffy, and Z.Z. Li. Robust $d_{x^2-y^2}$ pairing symmetry in hole-doped cuprate superconductors. *Phys. Rev. Lett.*, 93(18):187004, 2004.

[50] M. Matsumoto and H. Shiba. Coexistence of different symmetry order parameters near a surface in d-wave superconductors i. *J. Phys. Soc. Japan*, 64(9):3384–3396, 1995.

[51] M. Fogelström, D. Rainer, and J. A. Sauls. Tunneling into current-carrying surface states of high-T_c superconductors. *Phys. Rev. Lett.*, 79:281–284, 1997.

[52] B.D. Josephson. Possible new effects in superconductive tunnelling. *Phys. Lett.*, 1(7):251–253, 1962.

[53] P. W. Anderson and A. H. Dayem. Radio-frequency effects in superconducting thin film bridges. *Phys. Rev. Lett.*, 13:195–197, 1964.

[54] J.E. Zimmerman and A.H. Silver. Quantum effects in type ii superconductors. *Phys. Lett.*, 10(1):47–48, 1964.

[55] A. Barone and G. Paterno. *Physics and applications of the Josephson effect.* 1982.

[56] S. Shapiro. Josephson currents in superconducting tunneling: The effect of microwaves and other observations. *Phys. Rev. Lett.*, 11(2):80, 1963.

[57] E. McCumber. Phys. 39, 3113 (1968); W.C. Stewart. *Appl. Phys. Lett*, 12:277, 1968.

[58] H. Hilgenkamp and J. Mannhart. Grain boundaries in high-T_c superconductors. *Rev. Mod. Phys.*, 74(2):485, 2002.

[59] D. Dimos, P. Chaudhari, J. Mannhart, and F.K. LeGoues. Orientation dependence of grain-boundary critical currents in $YBa_2Cu_3O_{7-\delta}$ bicrystals. *Phys. Rev. Lett.*, 61(2):219, 1988.

[60] K.P. Daly, W.D. Dozier, J.F. Burch, S.B. Coons, R. Hu, C.E. Platt, and R.W. Simon. Substrate step-edge $YBa_2Cu_3O_7$ rf squids. *Appl. Phys. Lett.*, 58(5):543–545, 1991.

[61] F. Lombardi, Z. G. Ivanov, G. M. Fischer, E. Olsson, and T. Claeson. Transport and structural properties of the top and bottom grain boundaries in $YBa_2Cu_3O_{7-\delta}$ step-edge josephson junctions. *Appl. Phys. Lett.*, 72(2):249–251, 1998.

[62] C.P. Foley, E.E. Mitchell, S.K.H. Lam, B. Sankrithyan, Y.M. Wilson, D.L. Tilbrook, and S.J. Morris. Fabrication and characterisation of YBCO single grain boundary step edge junctions. *IEEE Trans. Appl. Supercond.*, 9(2):4281–4284, 1999.

[63] K. Char, M.S. Colclough, S.M. Garrison, N. Newman, and G. Zaharchuk. Bi-epitaxial grain boundary junctions in $YBa_2Cu_3O_7$. *Appl. Phys. Lett.*, 59(6):733–735, 1991.

[64] A. A. Golubov, M. Yu. Kupriyanov, and E. Il'ichev. The current-phase relation in josephson junctions. *Rev. Mod. Phys.*, 76:411–469, 2004.

[65] Manfred Sigrist and T. M. Rice. Unusual paramagnetic phenomena in granular high-temperature superconductors - A consequence of d- wave pairing? *Rev. Mod. Phys.*, 67:503–513, 1995.

[66] T. Löfwander, V.S. Shumeiko, and G. Wendin. Andreev bound states in high-T_c superconducting junctions. *Supercond. Sci. Technol.*, 14(5):R53, 2001.

[67] A.F. Andreev. On the theory of superconductivity. *Zh. Eksp. Teor. Fiz.*, 46:1823, 1964.

[68] Chia-Ren Hu. Midgap surface states as a novel signature for d^2_{xa}-x^2_b-wave superconductivity. *Phys. Rev. Lett.*, 72:1526–1529, 1994.

[69] M. Matsumoto and H. Shiba. Coexistence of different symmetry order parameters near a surface in d-wave superconductors ii. *J. Phys. Soc. Japan*, 64(12):4867–4881, 1995.

[70] M. Matsumoto and H. Shiba. Coexistence of different symmetry order parameters near a surface in d-wave superconductors iii. *J. Phys. Soc. Japan*, 65(7):2194–2203, 1996.

[71] Y. Tanuma, Y. Tanaka, M. Ogata, and S. Kashiwaya. Quasiparticle states near surfaces of high$-T_c$ superconductors based on the extended $t-j$ model. *Phys. Rev. B*, 60:9817–9826, 1999.

[72] W. Tsang and T. Van Duzer. Dc analysis of parallel arrays of two and three josephson junctions. *J. Appl. Phys.*, 46(10):4573–4580, 1975.

[73] K. Hasselbach, D. Mailly, and J.R. Kirtley. Micro-superconducting quantum interference device characteristics. *J. Appl. Phys.*, 91(7):4432–4437, 2002.

[74] C.D. Tesche and J. Clarke. Dc squid: Noise and optimization. *J. Low Temp. Phys.*, 29(3-4):301–331, 1977.

[75] J.M. Martinis and J. Clark. Measurements of current noise in DC SQUIDS. *IEEE Trans. on Magnetics*, 19:446–8, 1983.

[76] J. Gallop. SQUIDs: some limits to measurement. *Supercond. Sci. Technol.*, 16:1575, 2003.

[77] R Wölbing, T Schwarz, B Müller, J Nagel, M Kemmler, R Kleiner, and D Koelle. Optimizing the spin sensitivity of grain boundary junction nanoSQUIDs-towards detection of small spin systems with single-spin resolution. *Supercond. Sci. and Technol.*, 27(12):125007, 2014.

[78] S. Hunklinger and A. K. Raychaudhuri. Thermal and elastic anomalies in glasses at low temperatures. *Prog. Low Temp. Phys.*, IX, 1986.

[79] W.A. Phillips. Tunneling states in amorphous solids. *J. of Low Temp. Phys.*, 7(3):351–360, 1972.

[80] W. Phillips. Two-level states in glasses. *Rep. Prog. Phys*, 50:1657–1708, 1987.

[81] R.H. Koch, D.P. DiVincenzo, and J. Clarke. Model for $1/f$ flux noise in squids and qubits. *Phys. Rev. Lett.*, 98:267003, 2007.

[82] L. Faoro and L.B. Ioffe. Microscopic origin of low-frequency flux noise in josephson circuits. *Phys. Rev. Lett.*, 100:227005, 2008.

[83] S. Choi, Dung-Hai Lee, S.G. Louie, and J. Clarke. Localization of metal-induced gap states at the metal-insulator interface: Origin of flux noise in SQUIDs and superconducting qubits. *Phys. Rev. Lett.*, 103:197001, 2009.

[84] S. Sendelbach, D. Hover, M. Mück, and R. McDermott. Complex inductance, excess noise, and surface magnetism in dc squids. *Phys. Rev. Lett.*, 103:117001, 2009.

[85] C.M. Quintana et al. 2016.

[86] D.J. Van Harlingen, T.L. Robertson, B.L.T. Plourde, P.A. Reichardt, T.A. Crane, and J. Clarke. Decoherence in josephson-junction qubits due to critical-current fluctuations. *Phys. Rev. B*, 70:064517, 2004.

[87] C.T. Rogers and R.A. Buhrman. Composition of 1/f noise in metal-insulator-metal tunnel junctions. *Phys. Rev. Lett.*, 53:1272–1275, 1984.

[88] F.C. Wellstood, C. Urbina, and J. Clarke. Low-frequency noise in dc superconducting quantum interference devices below 1 K. *Appl. Phys. Lett.*, 50(12):772–774, 1987.

[89] F.C. Wellstood, C. Urbina, and J. Clarke. Flicker (1/f) noise in the critical current of josephson junctions at 0.09-4.2K. *Appl. Phys. Lett.*, 85(22):5296–5298, 2004.

[90] J. Eroms, L.C. van Schaarenburg, E.F.C. Driessen, J.H. Plantenberg, C.M. Huizinga, R.N. Schouten, A.H. Verbruggen, C.J.P.M. Harmans, and J.E. Mooij. Low-frequency noise in josephson junctions for superconducting qubits. *Appl. Phys. Lett.*, 89(12), 2006.

[91] E. Paladino, Y.M. Galperin, G. Falci, and B.L. Altshuler. $1/f$ noise: Implications for solid-state quantum information. *Rev. Mod. Phys.*, 86:361–418, 2014.

[92] D. Drung. High-T_c and low-T_c dc SQUID electronics. *Supercond. Sci. Technol.*, 16:1320–1336, 2003.

[93] K. K. Likharev and L. A. Yakobson. Steady state properties of superconducting bridges. *Sov. Phys. Tech. Phys.*, 20:950–954, 1976.

[94] R. Arpaia. *$YBa_2Cu_3O_{7-\delta}$ nanowires to study nanoscale ordering in High-Tc Superconductors.* PhD thesis, 2016.

[95] K.K. Likharev. Superconducting weak links. *Rev. Mod. Phys.*, 51:101–159, 1979.

[96] Kupriyanov et al. *LT14 T027*, 104, 1975.

[97] L.N. Bulaevskii, M.J. Graf, and V.G. Kogan. Vortex-assisted photon counts and their magnetic field dependence in single-photon superconducting detectors. *Phys. Rev. B*, 85:014505, 2012.

[98] C. C. Chi, P. Santhanam, and P. E. Blöchl. Interacting loop-current model of superconducting netwroks. *J. Low Temp. Phys.*, 88(1/2):163, 1992.

[99] T. Lindström, J. Healey, M. Colclough, C. Muirhead, and a. Tzalenchuk. Properties of superconducting planar resonators at millikelvin temperatures. *Phys. Rev. B*, 80:132501, 2009.

[100] P. Macha, S. H. W. van der Ploeg, G. Oelsner, E. Il'ichev, H.-G. Meyer, S. Wunsch, and M. Siegel. Losses in coplanar waveguide resonators at millikelvin temperatures. *Appl. Phys. Lett.*, 96:062503, 2010.

[101] J.M. Sage, V. Bolkhovsky, W.D. Oliver, B. Turek, and P.B. Welander. Study of loss in superconducting coplanar waveguide resonators. *J. Appl. Phys.*, 109:063915, 2011.

[102] M. Arzeo, F. Lombardi, and T. Bauch. Microwave losses in MgO, LAO, and LSAT dielectrics at low power and in the millikelvin temperature range. *Appl. Phys. Lett.*, 104:212601, 2014.

[103] B.A. Mazin. *Microwave Kinetic Inductance Detectors*. PhD thesis, 2004.

[104] U. Strom, M. von Schickfus, and S. Hunklinger. Low-Temperatures Anomalies in the Microwave Dielectric Properties of Na β-Alumina. *Phys. Rev. Lett.*, 41:910, 1978.

[105] L. Faoro and Lev B. Ioffe. Internal loss of superconducting resonators induced by interacting two-level systems. *Phys. Rev. Lett.*, 109:157005, 2012.

[106] D. Mattis and J. Bardeen. Theory of the Anomalous Skin Effect in Normal and Superconducting Metals. *Phys. Rev.*, 111:412, 1958.

[107] O. G. Vendik, I. B. Vendik, and D. I. Kaparkov. Empirical Model of the Microwave Properties of High-Temperature Superconductors. *IEEE Trans. Microw. Theory Tech.*, 46:469, 1998.

[108] W. Rauch, E. Gornik, G. Sul̈kner, A. A. Valenzuela, F. Fox, and H. Behner. Microwave properties of $YBa_2Cu_3O_{7-x}$ thin films studied with coplanar transmission line resonators. *J. Appl. Phys.*, 73(4):1866–1872, 1993.

[109] G. Ghigo, D. Botta, A. Chiodini, R. Gerbaldo, Gozzelino. L., F. Laviano, B. Minetti, E. Mezzetti, and D. Andreone. Microwave dissipation in YBCO coplanar resonators with uniform and non-uniform columnar defect distribution. *Supercond. Sci. Technol.*, 17:977, 2004.

[110] M.H. Devoret. *Quantum fluctuations in electrical circuits,*. S. Reynaud, E. Giacobino, and J. Zinn-Justin, eds, North-Holland/Elsevier, Amsterdam., 1997.

[111] V. Bouchiat, D. Vion, P. Joyez, D. Esteve, and M.H. Devoret. Quantum coherence with a single cooper pair. *Physica Scripta*, 1998:165, 1998.

[112] Y. Nakamura, Y.A. Pashkin, and J.S. Tsai. Coherent control of macroscopic quantum states in a single-cooper-pair box. *Nature*, 398:786, 1999.

[113] Caspar H. van der Wal, A.C.J. ter Haar, F.K. Wilhelm, R.N. Schouten, C.J.P.M. Harmans, T.P. Orlando, Seth Lloyd, and J.E. Mooij. Quantum superposition of macroscopic persistent-current states. *Science*, 290:773–777, 2000.

[114] J.R. Friedman, V. Patel, W. Chen, S. K. Tolpygo, and J. E. Lukens. Quantum superposition of distinct macroscopic states. *Nature*, 406:43, 2000.

[115] J. Koch, M. Yu. Terri, J. Gambetta, A. A. Houck, D. I. Schuster, J. Majer, A. Blais, M. H. Devoret, S. M. Girvin, and R. J. Schoelkopf. Charge-insensitive qubit design derived from the Cooper pair box. *Phys. Rev. A*, 76:042319, 2007.

[116] M.H. Devoret and J.M. Martinis. Course 12 superconducting qubits. *Les Houches Summer School Proceedings*, 79:443–485, 2004.

[117] David P. DiVincenzo. The physical implementation of quantum computation. *Fortschritte der Physik*, 48(9-11):771–783, 2000.

[118] E.M. Purcell. Resonance absorption by nuclear magnetic moments in a solid. *Phys. Rev.*, 69:37, 1946.

[119] M.H.S. Amin and A.Yu. Smirnov. Quasiparticle decoherence in d-wave superconducting qubits. *Phys. Rev. Lett.*, 92:017001, 2004.

[120] T. Bauch, D. Gustafsson, K. Cedergren, S. Nawaz, M. Mumtaz Virk, H. Pettersson, E. Olsson, and F. Lombardi. High critical temperature superconductor Josephson junctions for quantum circuit applications. *Phys. Scr.*, T137:014006, 2009.

[121] C.N. Chang, W.C. Chang, and C.H. Chen. Full-wave analysis of multilayer coplanar lines. *IEEE Trans. Microwave Theory and Techniques*, 39(4):747–750, 1991.

[122] R. Schinzinger and P.A.A. Laura. *Conformal Mapping: Methods and Applications*. Elselvier, 1991.

[123] S. Gevorgian, L.J.P. Linner, and E.L. Kollberg. CAD models for shielded multilayered CPW. *IEEE Trans. Microw. Theory Techn.*, 43(4):772–779, 1995.

[124] A. G. Zaitsev, R. Schneider, G. Linker, F. Ratzel, R. Smithey, P. Schweiss, J. Geerk, R. Schwab, and R. Heidinger. Microwave measurements of the absolute London penetration depth in double-sided $YBa_2Cu_3O_{7-x}$ thin films on sapphire. *Rev. Sci. Instr.*, 73(2):335–344, 2002.

[125] M.S. Khalil, M.J.A. Stoutimore, F.C. Wellstood, and K.D. Osborn. An analysis method for asymmetric resonator transmission applied to superconducting devices. *J. Appl. Phys.*, 111:054510, 2012.

[126] D. Stornaiuolo, G. Papari, N. Cennamo, F. Carillo, L. Longobardi, D. Massarotti, A. Barone, and F. Tafuri. High quality factor HTS Josephson junctions on low loss substrates. *Supercond. Sci. Technol.*, 24:045008, 2011.

[127] D. Stornaiuolo, G. Rotoli, D. Massarotti, F. Carillo, L. Longobardi, F. Beltram, and F. Tafuri. Resolving the effects of frequency-dependent damping and quantum phase diffusion in $YBa_2Cu_3O_{7-x}$ Josephson junctions. *Phys. Rev. B*, 87:134517, 2013.

[128] C H Wu, Y T Chou, W C Kuo, J H Chen, L M Wang, J C Chen, K L Chen, U C Sou, H C Yang, and J T Jeng. Fabrication and characterization of high-T_C $YBa_2Cu_3O_{7-x}$ nanosquids made by focused ion beam milling. *Nanotechnology*, 19(31):315304, 2008.

[129] N Curtz, E Koller, H Zbinden, M Decroux, L Antognazza, Ø Fischer, and N Gisin. Patterning of ultrathin YBCO nanowires using a new focused-ion-beam process. *Supercond. Sci. Technol.*, 23(4):045015, 2010.

[130] A. A. O. Elkaseh, W. J. Perold, and V. V. Srinivasu. Josephson nanoconstrictions made by AFM plowing of $YBa_2Cu_3O_{7-x}$ films. *J. Appl. Phys.*, 108(5):053914, 2010.

[131] A. I. Mansour, K. H. Chow, and J. Jung. Persistent critical current of $YBa_2Cu_3O_{7-\delta}$ nanowires. *J. Appl. Phys.*, 110(6):063909, 2011.

[132] K. Kajino, T. Kimura, Y. Horii, M. Watanabe, M. Inoue, and A. Fujimaki. Preparation of narrowed $YBa_2Cu_3O_{7-\delta}$ nanobridges down to 30 nm with reduced degradation. *IEEE Trans. Appl. Supercond.*, 19(3):178–182, 2009.

[133] G. Papari, F. Carillo, D. Born, L. Bartoloni, E. Gambale, D. Stornaiuolo, P. Pingue, F. Beltram, and F. Tafuri. YBCO nanobridges: Simplified fabrication process by using a Ti hard mask. *IEEE Trans. Appl. Supercond.*, 19(3):183–186, 2009.

[134] R. Arpaia, S. Nawaz, F. Lombardi, and T. Bauch. Improved nanopatterning for YBCO nanowires approaching the depairing current. *IEEE Trans. Appl. Supercond.*, 23:1101505, 2013.

[135] S. Nawaz, R. Arpaia, T. Bauch, and F. Lombardi. Approaching the theoretical depairing current in $YBa_2Cu_3O_{7-x}$ nanowires. *Physica C*, 495:33–38, 2013.

[136] S. Nawaz, R. Arpaia, F. Lombardi, and T. Bauch. Microwave response of superconducting $YBa_2Cu_3O_{7-\delta}$ nanowire bridges sustaining the critical depairing current: Evidence of Josephson-like behavior. *Phys. Rev. Lett.*, 110(16):167004, 2013.

[137] K. Cedergren. *Grain boundary Josephson π-junctions –Correlation between microstructure and transport properties for novel devices.* PhD thesis, 2010.

[138] M. Arzeo, F. Lombardi, and T. Bauch. Microwave losses in YBCO coplanar waveguide resonators at low power and millikelvin range. *IEEE Trans. Appl. Supercond.*, 25(3):1–4, 2015.

[139] Io-Chun Hoi, C.M. Wilson, G. Johansson, T. Palomaki, B. Peropadre, and P. Delsing. Demonstration of a single-photon router in the microwave regime. *Phys. Rev. Lett.*, 107:073601, 2011.

[140] P. Krantz, A. Bengtsson, M. Simoen, S. Gustavsson, V. Shumeiko, W.D. Oliver, C.M. Wilson, P. Delsing, and J. Bylander. Single-shot read-out of a superconducting qubit using a josephson parametric oscillator. *Nat. Comm.*, 7:11417, 2016.

[141] R. Arpaia, S. Charpentier, R. Toskovic, T. Bauch, and F. Lombardi. $YBa_2Cu_3O_{7-\delta}$ nanorings to probe fluxoid quantization in high critical temperature superconductors. *Physica C*, 506:184–187, 2014.

[142] R.L. Kautz, S.P. Benz, and C.D. Reintsema. Large amplitude Shapiro steps and self field effects in high-Tc Josephson weak links. *Appl. Phys. Lett.*, 65:1445–1447, 1994.

[143] R. Kleiner, A. S. Katz, A. G. Sun, R. Summer, D. A. Gajewski, S. H. Han, S. I. Woods, E. Dantsker, B. Chen, K. Char, M. B. Maple, R. C. Dynes, and John Clarke. Pair tunneling from c-axis $YBa_2Cu_3O_{7-x}$ to Pb: Evidence for s-wave component from microwave induced steps. *Phys. Rev. Lett.*, 76:2161–2164, 1996.

[144] M.H. Hamidian, S.D. Edkins, Sang Hyun Joo, A. Kostin, H. Eisaki, S. Uchida, M.J. Lawler, E-A Kim, A.P. Mackenzie, K. Fujita, et al. Detection of a cooper-pair density wave in $Bi_2Sr_2CaCu_2O_{8+x}$. *Nature*, 532(7599):343–347, 2016.

[145] E. Berg, E. Fradkin, and S.A. Kivelson. Charge-4e superconductivity from pair-density wave order in certain high-temperature superconductors. *Nat. Phys.*, 5:830–833, 2009.

[146] C. Granata, A. Vettoliere, R. Russo, M. Fretto, N. De Leo, and V. Lacquaniti. Three-dimensional spin nanosensor based on reliable tunnel josephson nano-junctions for nanomagnetism investigations. *Appl. Phys. Lett.*, 103(10), 2013.

[147] R. Arpaia, M. Arzeo, S. Nawaz, S. Charpentier, F. Lombardi, and T. Bauch. Ultra low noise $YBa_2Cu_3O_{7-\delta}$ nano superconducting quantum interference devices implementing nanowires. *Appl. Phys. Lett.*, 104(7):072603, 2014.

[148] T. Schwarz, R. Wölbing, C. F. Reiche, B. Müller, M. J. Martínez-Pérez, T. Mühl, B. Büchner, R. Kleiner, and D. Koelle. Low-Noise $YBa_2Cu_3O_7$ Nano-SQUIDs for performing magnetization-reversal measurements on magnetic nanoparticles. *Phys. Rev. Applied*, 3:044011, 2015.

[149] M. Arzeo, R. Arpaia, R. Baghdadi, F. Lombardi, and T. Bauch. Toward ultra high magnetic field sensitivity $YBa_2Cu_3O_{7-\delta}$ nanowire based superconducting quantum interference devices. *J. Appl. Phys.*, 119(17):174501, 2016.

[150] R. Arpaia, D. Golubev, R. Baghdadi, M. Arzeo, G. Kunakova, S. Charpentier, S. Nawaz, F. Lombardi, and T. Bauch. Resistive state triggered by vortex entry in $YBa_2Cu_3O_{7-\delta}$ nanostructures. *Physica C*, 506(15):165–168, 2014.

[151] J. Schneider, M. Muck, and R. Wordenweber. dc squids based upon $YBa_2Cu_3O_7$ nanobridges. *Appl. Phys. Lett.*, 65(19):2475–2477, 1994.

[152] M. V. Pedyash, D. H. A. Blank, and H. Rogalla. Superconducting quantum interference devices based on YBaCuO nanobridges. *Appl. Phys. Lett.*, 68(8):1156–1158, 1996.

[153] P.A. Rosenthal, M.R. Beasley, K. Char, M. . Colclough, and G. Zaharchuk. Flux focusing effects in planar thin-film grain boundary Josephson junctions. *Appl. Phys. Lett.*, 59(26):3482–3484, 1991.

[154] T. Van Duzer and C.W. Turner. *Principles of Superconductive Devices and Circuits*. Prentice Hall, 1999.

[155] Y. L. Loh, E. W. Carlson, and K. A. Dahmen. Noise predictions for STM in systems with local electron nematic order. *Phys. Rev. B*, 81:224207, 2010.

[156] E. W. Carlson and K. A. Dahmen. Using disorder to detect locally ordered electron nematics via hysteresis. *Nat. Commun.*, 2:379, 2011.

[157] S. Scouten, Yizi Xu, B. H. Moeckly, and R. A. Buhrman. Low-frequency noise in the normal state of thin-film high-temperature superconductors. *Phys. Rev. B*, 50:16121–16124, 1994.

[158] L. N. Bulaevskii, M. J. Graf, C. D. Batista, and V. G. Kogan. Vortex-induced dissipation in narrow current-biased thin-film superconducting strips. *Phys. Rev. B*, 83:144526, 2011.

[159] R. Arpaia, M. Arzeo, R. Baghdadi, E. Trabaldo, F. Lombardi, and T. Bauch. Improved noise performance of ultrathin YBCO Dayem bridge nanoSQUIDs. *Supercond. Sci. Technol.*, to be published.

[160] J. Gao, J. Zmuidzinas, B. A. Mazin, P. K. Day, and H. G. Leduc. Experimental study of the kinetic inductance fraction of superconducting coplanar waveguide. *Nucl. Instrum. Methods Phys. Res. A*, 559:585, 2006.

[161] A.M. Black-Schaffer, D.S. Golubev, T. Bauch, F. Lombardi, and M. Fogelström. Model evidence of a superconducting state with a full energy gap in small cuprate islands. *Phys. Rev. Lett.*, 110:197001, 2013.

[162] A.A. Houck, D.I. Schuster, J.M. Gambetta, J.A. Schreier, B.R. Johnson, J.M. Chow, L. Frunzio, J. Majer, M.H. Devoret, S.M. Girvin, and R.J. Schoelkopf. Generating single microwave photons in a circuit. *Nature*, 449:328–331, 2007.

[163] D.I. Schuster. *Circuit Quantum Electrodynamics*. PhD thesis, 2007.

[164] H. le Sueur, P. Joyez, H. Pothier, C. Urbina, and D. Esteve. Phase controlled superconducting proximity effect probed by tunneling spectroscopy. *Phys. Rev. Lett.*, 100:197002, 2008.

[165] T. W. Larsen, K. D. Petersson, F. Kuemmeth, T. S. Jespersen, P. Krogstrup, J. Nygård, and C. M. Marcus. Semiconductor-nanowire-based superconducting qubit. *Phys. Rev. Lett.*, 115:127001, 2015.

[166] R. Gross, P. Chaudhari, M. Kawasaki, and A. Gupta. Scaling behavior in electrical transport across grain boundaries in $YBa_2Cu_3O_{7-\delta}$ superconductors. *Phys. Rev. B*, 42:10735–10737, 1990.

[167] A. Marx and R. Gross. Scaling behavior of 1/f noise in high-temperature superconductor josephson junctions. *Appl. Phys. Lett.*, 70(1):120–122, 1997.

[168] A.H. Miklich, J. Clarke, M.S. Colclough, and K. Char. Flicker (1/f) noise in biepitaxial grain boundary junctions of $YBa_2Cu_3O_{7-x}$. *Appl. Phys. Lett.*, 60(15):1899–1901, 1992.

[169] D. Gustafsson, F. Lombardi, and T. Bauch. Noise properties of nanoscale $YBa_2Cu_3O_{7-\delta}$ josephson junctions. *Phys. Rev. B*, 84(18):184526, 2011.

[170] M. M. Khapaev. Extraction of inductances of plane thin film superconducting circuits. *Supercond. Sci. Technol.*, 10:389–394, 1997.

[171] J.R. Clem and E.H. Brandt. Response of thin-film SQUIDs to applied fields and vortex fields: Linear SQUIDs. *Phys. Rev. B*, 72:174511, 2005.